School of Civil and Mechanical Engineering
Department of Mechanical Engineering

Characteristics of Erosion and Sedimentation in Curved Fluid Passages

Claudio Faria Duarte

This thesis is presented for the Degree of
Doctor of Philosophy - Mechanical Engineering
of
Curtin University

February 2020

Declaration

To the best of my knowledge and belief this thesis contains no material previously published by any other person except where due acknowledgement has been made. This thesis contains no material which has been accepted for the award of any other degree or diploma in any university.

Signature: .....

Date: .....

"Ability is nothing without opportunity"
- Napoleon Bonaparte

Acknowledgements

To Professor Tilak Chandratilleke. I would like to thank him for his support during my PhD and for sharing his wealth of knowledge in both theoretical and experimental work. Moreover, I enjoyed the benefit of advice pertaining both to my research and personal life.

To Dr Nima Nadim. I would like to thank him for the substantial amount of time he has spent in guiding me throughout my PhD, and the extra mile he has taken to make himself available. His depth of knowledge and passion for numerical analysis, and research more broadly, has been an inspiration to me.

To my darling wife. She has been my greatest support and motivation. She is my rock. My mentor. My reminder of what is important in life.

To my toddler son, Hugo. For his many amusing interruptions and for teaching me what it means to be truly curious.

To my brothers in A Squadron, 10th Light Horse. For imparting the virtues of focus, discipline and dedication. *Percute et Percute Velociter.*

Abstract

Fluid flow characteristics through curved passages are vastly different to those within straight channels. In curved passages, centrifugal effects from passage curvature induce secondary vortices that generate lateral fluid circulation within the main (axial) flow, thus resulting in unique spiralling flow behaviour in curved passages.

The secondary flow mechanisms represent a mechanistically challenging area of scientific investigation, both in industrial and natural environments. In applications such as slurry (granular) flow in mining, suspended solid particles flowing through pipe bends are continuously driven towards outer pipe wall by the action of secondary flow vortex motion, causing exaggerated pipe wall abrasion at pipe bends and in some situations, pipe blockage due to particle segregation. In nature as a river flows over a bend, river sand bed undergoes erosion at the outer periphery, where sand particles are dislodged by the shear forces induced by secondary flow and subsequently deposited at the inner river boundary or downstream in the process of sedimentation. Under controlled laboratory conditions, the research work described in this thesis investigates the erosion and sedimentation processes associated with a curved flow passage comprising a granular particle bed.

Whilst secondary flow behaviour in curved passages with solid walls is well documented, the fluid dynamical effects of secondary vortices on granular beds and potential changes to bed profile remain relatively unexplored largely due to interacting complexities of flow parameters. A clearer understanding of sedimentation and erosion mechanisms is not fully warranted by the reported studies that are essentially confined to open channels, where the secondary flow effects are marginal compared to closed flow passages.

This study experimentally and numerically examines the granular (sand) bed behaviour in a curved rectangular closed passage carrying a steady stream of water as the working fluid. A semicircular (180°) transparent test section is designed and developed with necessary flow circuit, measuring instrumentation and recording devices. A spot laser array combined with a photographic recording arrangement is deployed to obtain precise transient data on fluid-bed interface (profile) variation with time (temporal interrogation) and along the flow direction through the curved passage (spatial interrogation). Extensive combination of tests is performed to cover a range of water flow rates and bed sand grain sizes. Test results are used for extracting both qualitative observations and quantitative interpretations of parametric influences on channel sand bed profile behaviour, and to recognise erosion and sedimentation processes along with their unique characteristics.

Both qualitative and quantitative findings conclusively indicate that secondary flow imparts a dominant and significant influence on the sand bed behaviour for all tested flow rates. The test results identify three distinct periods of interactions between the fluid flow and the sand bed namely, the initiation stage, transient stage and the quasi-stable stage.

For the comparison between experimental and numerical findings, a numerical simulation is developed using Euler-Euler Granular Phase (EEGP) model that predicts the flow field and fluid-granular interactions. This approach assumes the granular phase as a continuum medium with characteristics similar to a fluid phase, using the analogy between gas dynamics and granular particles interactions. Mechanistic and empirical closures are deployed to synthesis a mathematical model of particle dynamics which is solved within the framework of Navier-Stokes equation.

Contents

List of Figures

List of Publications and Presentations

Publications

1. Duarte, C. F., Nadim, N., & Chandratilleke, T. T. (2019). Experimental study of granular bed erosion and sedimentation subjugated to the secondary flow structures in curved ducts. Advances in Mechanical Engineering, 11(11), 1687814019885255.[1]

Presentations:

1. 12th European Fluid Mechanics Conference, Vienna Austria, Sep 2018
2. 20th Australasian Fluid Mechanics Conference, Perth Australia, Dec 2016

Nomenclature

a	Height of duct cross-section (m)
Ar	Aspect ratio = a/b
b	Width of duct cross-section (m)
C_l	Lift coefficient
d_p	Particle diameter (μm)
e_{ss}	Coefficient of restitution for particle collision
g	Gravitational acceleration (m/s^2)
H^*	Dimensionless helicity
K	Dean number
k_{fs}	Fluid-Solid exchange coefficient
P	Static pressure (Pa)
R	Radius of curved passage = $\frac{R_o - R_i}{2}$ (m)
Re	Reynolds number = $\frac{U_{in} D_h}{\upsilon}$
U_{c}	Calibration uncertainty
U_{G}	Gauge block uncertainty
U_{T}	Total uncertainty
U_{in}	Velocity at duct inlet (m/s)
$u_{s,i}$	fluctuating solid velocity
x, y, z	Coordinates (m)

$\vec{F}_{lift}$ Lift force (N)

$\vec{v}_f$ Velocity of fluid phase (m/s)

$\vec{v}_s$ Velocity of solid phase (m/s)

Re_ω Vorticity Reynolds number

Re_p Particle Reynolds number

Greek Symbols

α Volume fraction

α_f Volume fraction of fluid phase

α_q Volume fraction of qth phase

α_s Volume fraction of solid phase

$\emptyset$ Internal friction angle $(^\circ)$

Γ Curvature ratio $= \frac{D}{R}$

γ_f Fluid phase diffusion coefficient

λ_s Bulk viscosity

μ Dynamic viscosity (Ns/m^2)

ρ_f Fluid phase density (kg/m^3)

τ Viscous stress tensor

Θ_s Granular temperature

υ Kinematic Viscosity (m^2/s)

Chapter 1

Introduction

1.1 Background

In a curved flow passage, the mechanistic principle of centrifugal action inducing radially driven fluid motion, and the presence of secondary vortex structures is a well-known. These vortex structures, inclusive of Dean vortices give rise to additional fluid mixing, flow turbulence and pressure drop across curved flow passages. Inspired by the challenging fluid mechanics, the characteristics of flow in curved passages have received significant attention in the analyses and applications involving multi-phase momentum, heat and mass exchanges.

In a curved passage with a bed of granular material, when the fluid flow is sufficiently strong, wall shear imparted by secondary flow structure tends to dislodge granular particles and shift them radially over the passage cross-section (i.e. laterally) as well as axially in the flow direction. These two erosion mechanisms are mutually interactive and determine the subsequent sedimentation of the dislodged material whilst influenced by the secondary flow. Consequently, curved passages exhibit essentially different granular bed erosion and sedimentation profiles in the flow passage compared to those in straight ducts, where the axial flow imparts particle movement.

Erosion and sedimentation processes subjected to secondary flow effects are common occurrences in nature. For example, in river flow over bends, sand is carved out from the bed by the water at the outer flow boundary while the eroded sand is deposited at the inner flow contour. Thus the river flow at bends indicates higher water depth at outer boundary where ground erosion and changes to landscape are more prevalent. Behaviour of tornados follows a similar flow principle that imparts a higher devastating impact on the outer core of the whirling fluid column. In industrial applications such as slurry (granular) flow in mining, pipe abrasion affecting protective lining is much exaggerated at pipe bends due to the lateral particle movement from the secondary flow. These swirling vortices also have the tendency segregate heavy particles at inner pipe bend thus potentially creating flow blockages. Similar flow behaviour and

adverse impact are observed with immiscible multi-phase fluid mixtures flowing thorough pipe bends, where phase separation is an inevitable phenomenon.

Recognising scientific challenges and industrial significance, the fundamental and applied problem of granular bed behaviour submerged in a flowing fluid has been scientifically studied through the onset of erosion, the pattern of bed reshaping and timescale of transitions, without the influence of secondary flow. Similarly, an extensive knowledge base is reported on the secondary flow behaviour in curved ducts with many analytical, experimental and numerical modelling studies, and a wide range of applicable methodologies in the field. However, studies on granular bed erosion in the presence of secondary flow remain virtually unexplored owing to the mechanistic complexities embedded in this flow situation.

Accordingly, the literature reporting erosion-sedimentation process in curved ducts is practically non-existent. The current study addresses this shortfall through an experimental and numerical investigation of erosion and sedimentation processes in a curved passage with granular material forming the bed of the flow passage.

Numerical investigation utilises a relatively contemporary approach, by way of an Euler-Euler Granular Phase (EEGP) model, which has been implemented for various applications including in curved ducts. Based on many sub-closures (solid pressure, granular temperature and drag force), EEGP is still considered to be an evolving model which needs to be calibrated, examined and validated for each applied configuration. Resent investigations utilised an EEGP model to investigate the influence of secondary flow on erosion-sedimentation of a granular bed in a curved duct with a rectangular cross-section. This provided a deterministic foundation for examining the dynamic interaction between the granular bed and the secondary flow structure, and for predicting and analysing the variation of the bed profile under various flow conditions. Such interactions have a two-way influence, namely the bed shape variation over the channel cross-section, in the axial direction, as well as the imparted secondary flow effects. This work accurately accounted for the lateral and axial erosion/sedimentation occurring in curved passage granular bed. Nonetheless, proper model validation was not possible due to the non-availability of reliable and applicable experimental data. The study presented in this thesis fulfils this using a practical, robust and cost effective non-intrusive method for measurement.

1.2 Scope of Work

The study presented in this thesis sets out to experimentally and numerically track the fluid-bed interface over time (temporal investigation) and across the curved section (spatial investigation) for interpreting the interaction of spiral flow structure and granular phase. The current understanding of the secondary flow structure explains the intensity of lateral vortices, their combined effect with axial flow and the time scale of variation. The test section used is a transparent curved rectangular duct forming a 180-degree bend, which is filled with sand to form a flat granular bed along its length. Changes in the granular bed profile due to fluid-granular interactions are captured using an array of perpendicularly mounted lasers utilised to illuminate discrete points across the bed interface. A number of tests are carried out to investigate and report the influence of flow rate as the primary parameter of interest while various particle size ranges are compared to obtain possible size influence.

1.3 Research Objectives

This research study examines the characteristics of a secondary flow interaction with a flat granular bed placed inside of a curved fluid passage. Experimental and numerical techniques are employed to investigate interactions between the liquid and granular phases. A qualitative and quantitative characterisation is provided, with spatial and temporal comparison made for varied granular phase particle size ranges over a range of flow rates. In view of these, the objectives of this work are as follows:

- Provide a qualitative description of interactions between the granular phase and curvature induced helical flow structures;
- Characterisation and description of granular bed structures;
- Identify regions of interest for quantitative investigation;
- Provide quantitative results of spatial and temporal interactions between the granular phase and curvature induced helical flow structures;
- Utilise a Euler-Euler Granular Phase model to characterise helical flow structure interaction with the granular phase; and
- Assess compatibility between experimental and numerical approaches.

Chapter 2

Literature Survey

2.1 Granular Material

Granular material is a conglomeration of discrete grains larger than 100 μm[2], with unique physical characteristics producing surprising and complex behaviour that still confounds researchers to the present day[2, 3]. A brief description of the properties and behaviour of granular material is provided. Additionally, parameters of significance and there broader context is delivered and discussed.

Classification of granular material is divided into three regimes or phases, seen in Figure 2.1: (i) the solid or dense-quasi static regime where deformations occur over an extended timescale is dominated by frictional contact between grains; (ii) an intermediate liquid regime driven by both collision and friction between grains, and (iii) the gaseous regime characterised by rapid and dilute flow, caused by binary collisions among grains. Though three distinct regimes are characterised, the transition between regimes is an ongoing research challenge and underpins the complex nature of granular materials[2, 4, 5].

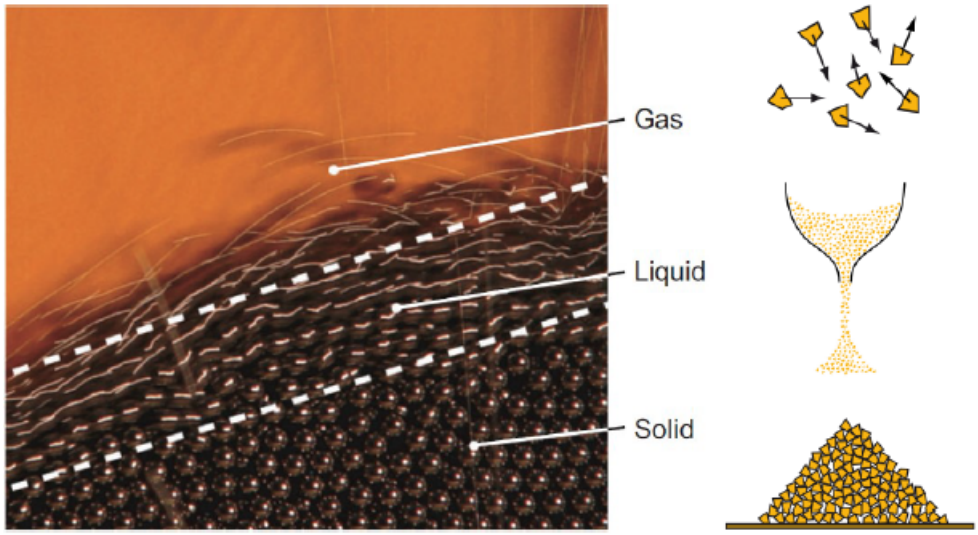

Figure 2.1: *Flow regimes of granular materials[6]*

The granular solid phase (dense quasi-static regime) is the most understood of the three regimes present in granular material. The solid phase is defined by internal friction generated by inter-granular contact forces, seen by the angle of repose of resting granular piles. The liquid phase often described as the friction-collisional regime is the most poorly understood of the three phases present in a granular material[7]. Models describing dense granular flow are typically derived from either the dense-quasi static regime (granular solid phase), based on a generalisation of Coulomb's law[8], or the collision dominated gaseous regime, derived from Kinetic Theory for Granular Flow (KTGF) models. A unified framework is still lacking, with models typically limited to describing dense granular flows under steady flow states in simple shear, which fail to capture the complex behaviour which is common in most granular flows[2, 9].

The gas phase described as dilute granular flow is modelled using the KTGF model[10, 11]. The KTGF model is an extension of the kinetic theory of gases and is a measure of the kinetic energy of random velocity fluctuations of particles in the granular phase. A principal difference between the kinetic theory of gases and the KTGF model is that interactions are fundamentally non-conservative, with collisions between grains treated as inelastic. To account for this difference, the principle of granular temperature was introduced, defined as the sum of the variance of instantaneous velocity components of grains; and form a central component in the modelling of dilute granular flows[11]. Granular flows comprising both gas and liquid phases exhibit rapid energy dissipation. Concerning the work presented the most influential granular regimes are the liquid and gaseous phases.

Interaction between granular material and external forces result in formation of patterns, or in the case if interaction due to fluid shear, ripples and dunes. A pioneering contribution to the understanding of dune formation was that of Bagnolds[12]. Using sand as the granular material, identification of two primary mechanisms of transportation were made; namely saltation and creep. Using Bagnold's description, a brief overview of the fundamental mechanisms is provided.

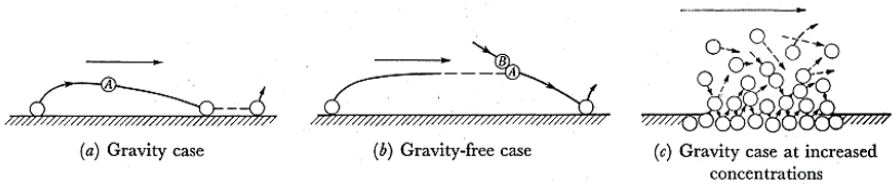

Figure 2.2: *Types of particle-particle collisions due to saltation[13]*

Saltation named after the jumping motion of random individual grains along the granular bed surface[14], is characterised into three cases, shown in Figure 2.2. The gravity case is described as resulting from random ejections of grains from the bed surface, and subsequent resettling on the bed due to gravity dominating forces acting on the grain. The gravity-free case resulting from higher shear rates where the ejected grain encounters faster grains entrained by the carrier fluid, deflected onto the bed and saltating once more. The final gravity case at increased concentration, initiates when the concentration of grains above the bed is such, that momentum from the fluid is transferred to the grains above the bed; therefore intergranular collision becomes the dominate mechanism of grain ejection.

Interaction between a shearing fluid and granular materials are influenced not only by the granular material properties but by the effect of momentum transfer from the fluid to the granular material and the transfer of momentum between grains. The result of this complex coupled relationship is seen in the formation of structures such as dunes.

2.2 Threshold of Grain Movement of Granular Material

Investigation into the threshold of grain movement is a long-standing area of research which has continued for more than 80 years[15]. Much time and effort have been invested in identifying flow and grain properties which affect the initiation of grain movement, known as incipient grain movement, the definition of which differs for several significant works[16]. Though there is agreement as to what properties are of importance with respect to grain movement, many of the proposed methods for prediction of the onset of grain movement have produced results which have a high degree of scatter. This increase in scatter can be seen by the many iterations and modifications to Shields seminal work, and the continued use of this work despite this.

Work by Shields was arguably the most significant contribution to this field, providing a non-dimensional number for the prediction of incipient grain movement, known as Shields parameter. His experimental work made use of a square open channel in which he placed grains of different densities, sizes, roughness, and shape. Using the velocity distribution at the channel centre, he set about computing a relationship between the drag force and buoyancy force acting on a grain this became known as Shields parameter. Using collated experimental data, and statistical analysis an empirical relationship between Shields parameter and the grain Reynolds number was produced, known as the Shields Diagram; as seen in Figure 2.3.

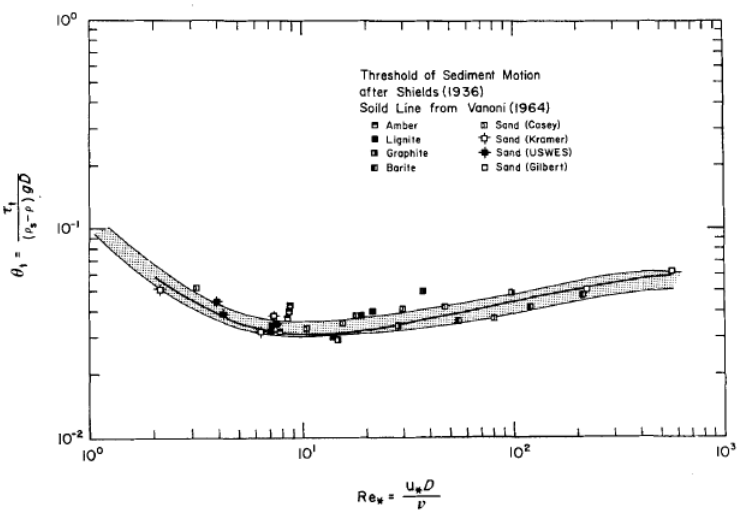

Figure 2.3: *An early version of Shields Diagram, Shields parameter is shown on the y-axis, with the grain Reynolds number on the x-axis[16].*

A limitation of the original work by Shields and subsequent authors was the lack of experimentally obtained data for incipient grain movement of grains smaller than 200 μm in diameter. The lack of published work in this area was first identified by White, noting that the 200 μm grain diameter was significant, as it represented not only the demarcation difference between hydraulically rough and smooth beds, but was more representative of geologically important minerals. A flume with a granular bed made up of the particles of interest was tested under turbulent flow conditions for all experiments using water. White went on to show that the although he confirmed Shields's original general argument, the extrapolation made by Shields for low grain Reynolds numbers was not in agreement with his experimental findings.

White made use of multiple regression models to investigate whether or not any correlation between Shields parameter and sediment properties, such as sphericity, sorting, and angle of repose existed, concluding that these parameters were independent of Shields parameter. Furthermore, no correlation was found between Shields parameter and flow depth and surface slope[17]. White's work played an essential role in improving and correcting values at lower grain Reynolds numbers in Shields Diagram, as shown in Figure 2.4. The data provided by White has remained a consistent feature of the numerous modified versions of Shields diagram.

With increased research into incipient grain movement came an increase in scatter to Shields original diagram. Miller et al. undertook a re-examination of the various studies and data produced during this period. Noting that many empirical graphical relationships have been proposed, and equations derived to define the threshold conditions, none had been shown to be a general relationship for all combinations of grain sizes, densities, and flow conditions[16].

Miller et al. set criteria for the selection of data to be used; experiments were to be performed using flumes with parallel walls under steady flow conditions over a pre-flattened bed. The particles to be utilised needed to be non-cohesive, rounded or spherical and could be either artificial or natural and be of uniform size. Additionally, the definition for incipient grain motion needed to be consistent for all datasets. Making use of the data that met these criteria, Miller et al. proposed an empirical curve that was similar to Shields. Concluding that at low grain Reynolds numbers the grain diameter was still a factor in the threshold relationship of incipient grain motion.

It was concluded by Miller et al., that Shields diagrams are most generally applied to closely graded materials of spherical or near-spherical grain shapes subjected to a liquid flow[16]. Millet et al. noted, empirical diagrams that were reviewed or modified were limited by the effect of grain size distribution, as the data that was available made use of beds with a size distribution that was not of a sufficiently wide size distribution to accurately represent those of natural systems.

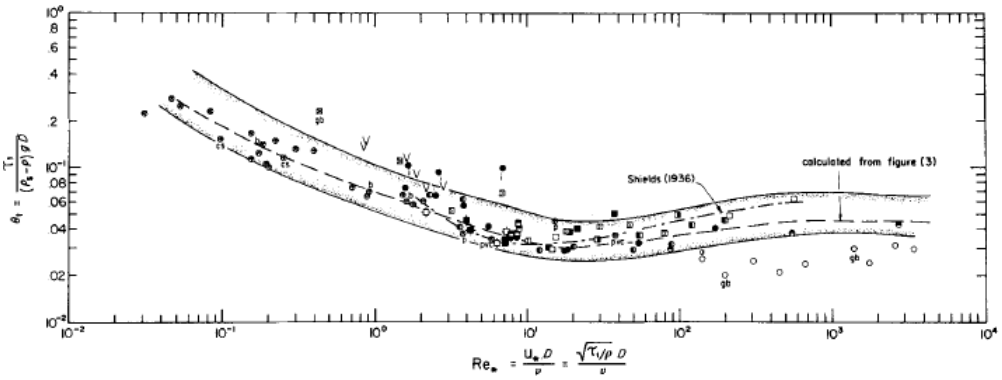

Figure 2.4: *Modified Shields Diagram, showing the increased scatter produced by the addition of experimental data[16].*

An area that had not been covered in previous works was the importance of grain protrusion. This was addressed by Fenton et al. who reasoned that granular beds even if levelled as flat as practicable would have many protruding grains above the nominally flat surface, noting that for small grain diameters the protruding grains will be exposed by almost an entire grain diameter above the surface[18]. Fenton et al. noted that as there was no practical way of achieving a perfectly flat granular bed either in a lab or in natural conditions like those on a river bed. Fenton et al. concluded that grain protrusion was an essential parameter for both transitional and turbulent flow conditions, and that it must be assumed that when working with grains smaller than 500 μm that total protrusion occurs.

Granular beds are comprised of various grain diameters of different sizes; typically these granular beds experience a phenomenon called bed armouring. Bed armouring is the removal of a surface layer of smaller grains to leave behind a layer of larger less buoyant grains. During experimental work by Hong et al. which investigated the erosion threshold of various grain sizes, and roughness values under laminar flow conditions. Hong et al. sought to reduce the potential effects of bed armouring making use of monodispersed grain sizes. Regardless of these precautions, armouring of the bed was observed. This was reported to be consistent with Charru et al. observations, who noted that freshly prepared

beds would consolidate over a prolonged period of shearing, and therefore exhibit bed armouring[19]. Hong et al. found bed armouring responsible for the systematic variation of critical Shields number to particle Reynolds number, showing that this varied for particles of the same size, and was dependant on the whether the bed were freshly prepared or not. The source of armouring was attributed to grain rearrangement as opposed to being a result of size sorting typical of beds with broad particle size ranges. Additionally, Hong et al. concluded that grains at the bed surface are only partially exposed to flow, aligning with observations made by Fenton et al.

A more recently, work by Houssais et al. investigated the slow granular dynamics within the fluid sheared granular bed, known as granular creep. Houssais et al. proposed that a critical Shields number still exists, but rather than representing the threshold for incipient grain motion, it represents a bifurcation in the transport of grains between creep and bed load, shown in Figure 2.5 by a red dot.

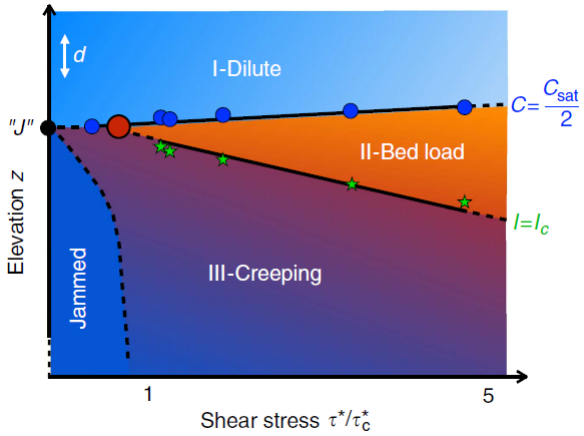

Figure 2.5: *Phase diagram of fluid-sheared granular transport, noting the bifurcation of the bed-load phase and the creeping phase[20].*

The existence of creep within the granular bed is significant, existing models do not account for the dissipative effects on fluid momentum due to fluid penetration of the bed[20]. Houssais et al. concluded that surface grain motion was not only due to the effects of fluid shear forces acting on the particles but also from the effects of granular creep below the surface.

In summary, Shields identified the principle parameters for incipient grain movement and defined a non-dimensional parameter known as Shields parameter; which consists of the ratio of horizontal shear force over the grain buoyancy force. Shields parameter is still widely used for predicting the onset of erosion in river beds; this is not surprising as the experimental conditions by which Shields obtained his data was a close approximation of river bed systems. Furthermore, parameters such as grain shape, sorting, angle of repose and grain protrusion, have been shown to be of importance. By controlling these parameters, the accuracy and predictability of determining the onset of erosion are increased. A limitation of such controlled experiments is that industrial and natural processes do not have such tight constraints; understanding the variability that these parameters introduce is important. Additionally, preparation of granular material was also shown to affect the onset of erosion, and that freshly prepared beds tended to be more susceptible to bed armouring. An important and more recent observation is that it is not merely shear forces acting on the granular bed surface, but also the forces of granular creep below the bed that are a contributing factor.

Based on the reviewed literature, selection of granular bed parameters will be of utmost importance. A granular bed, comprising of quartz sand, which will be sieved to provide grain size ranges which are as small as possible. Additionally, granular bed preparation and bed surface levelling will need to be consistent to reduce the effects of armouring and bed perturbation; this will improve repeatability of experimental results.

2.3 The role of turbulence on fluid-granular interaction

The effects of turbulence on granular beds is of great importance. The stochastic nature of granular materials is compounded with the stochastic nature of turbulent flow structures. These flow make the prediction of incipient grain movement using methods such as Shield's parameter inaccurate. It was brought to light by both theoretical and experimental means, that when turbulent conditions existed that methods developed under steady uniform flow conditions were not appropriate for the determination of sediment transport fields over them[21–24]. The role turbulence plays on fluid-granular interactions is discussed, an initial understanding of the nature of turbulent boundary layers and the production of turbulence is first provided. Turbulent boundary layer interactions with bedforms such as dunes are then described, and the mechanism by which they are initially formed, and propagated are explained. Additionally, the influence of turbulence and its effects on individual grain dislodgment is discussed.

To understand the impact that turbulence has on the fluid-granular interface, insight into the nature and effects of turbulent boundary layers is required. Significant work in this area was undertaken by Kline et al. who provided the identification of bursting phenomenon, a process described as the violent ejection of low-speed fluid into the faster moving flow[25]. The presence of bursting, seen as violent ejections, was also observed by Corino et al[26].

Kline et al. provided both qualitative and quantitative data using hydrogen bubbles to visualise the structure of turbulent boundary layers. In contrast, Corino et al. using colloidal particles and high-speed photography for flow visualisation, was able to observe both the flow field and the viscous sublayer. The use of flow visualisation enabled the capturing of interactions between the various regions, namely the shear layer and the ejection layer. In the viscous sublayer, Corino et al. noted that the flow is not laminar but is rather disturbed by elements of fluid from the adjacent region[26].

Furthermore, Corino et al. observed the presence of bursting events, and their interactions with adjacent the shear layer and ejection layer, resulted in disturbances which extend through the viscous sublayer extended to the pipe wall. Corino et al. concluded that an important characteristic of the flow located closest to the wall was the existence of busting seen as ejections of fluid elements into the mean flow and describing them as both spatially, and temporally random.

The previous works discussed above used flat, smooth beds or smooth pipe walls to characterise the nature of turbulent boundary layer interaction. In the case of a granular bed with various grain sizes the effects that grain roughness has on the nature of the turbulent boundary layer is important to understand. The effect of bed roughness on the turbulent boundary-layer investigated by Grass[27] undertook experiments using an open channel in which a bed of various roughnesses were placed; A flat, smooth bed, a bed filled with 2 mm diameter sand, and a bed with 9 mm diameter pebbles. Grass confirmed the findings made by Kline et al. for the smooth bed case, identifying both busting and sweeps. Furthermore, it was concluded that the phenomenon of sweep and subsequent busting events took place irrespective of surface roughness[27]. Grass noted that low momentum fluid is ejected from the viscous sublayer as well as from between the grains or pebbles making up the bed[27].

The discovery and characterisation of boundary layer interactions opened the way for investigation into the interaction of grains and boundary layer turbulence. Due to the observed ejection of low momentum fluid into the bulk flow and the bursting phenomenon by Kline et al. and Cotino et al.

Noting the lack of experimental work regarding interactions between turbulent boundary layers and grains Rashidi et al. undertook experiments using a horizontal straight channel. A Parametric study in which the effects of particle size, density, loading and the flow Reynolds number were investigated. Regarding the mechanism of particle transport Rashidi et al. observed that grains accumulated along low-speed streaks (Figure 2.6a), the accumulated grains are then agitated and lifted by induced vortex-loops and are subsequently ejected into the bulk flow by the vortex-loop breakdown known as bursting[28]. Rashidi et al. concluded that when larger grains (1100 μm) were introduced an increase in ejection was observed, and with smaller grains (120 μm) the number of ejections decreased. Furthermore, experimental data showed that the ejection angle of a particle was dependant on the particle size. With smaller grains being ejected at higher angles into the bulk flow when compared to larger grains, seen in Figure 2.6b.

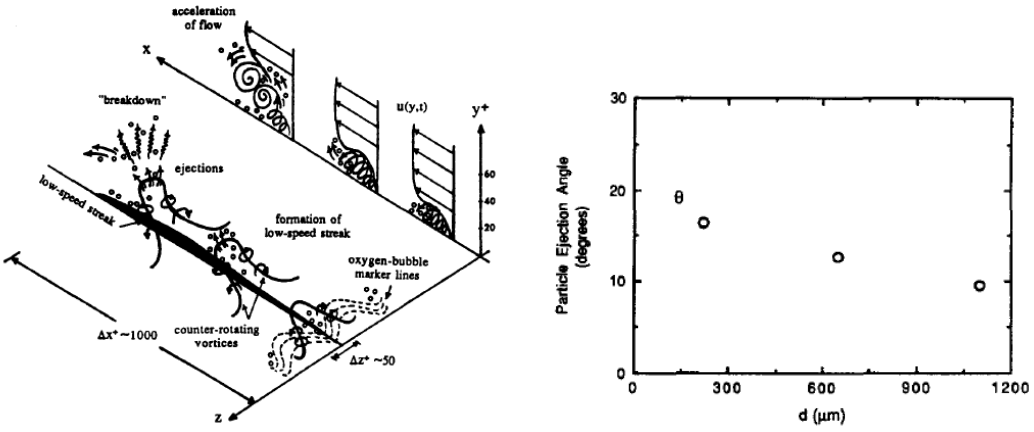

(a) (b)

Figure 2.6: *(a) Mechanism of particle transport near the wall, (b) Effect of particle size on the average particle ejection angle. Adapted from Rashidi et al.[28]*

The product of bed perturbations induced by sweeps and bursts are bedforms such as ripples and dunes. The accumulation of grains where low-speed steaks are present has been studied extensively, a comprehensive review was undertaken by Best[29, 30]. These accumulations allow the sedimentation of grains to collect and form dunes.

Experiments using a flat bed arrangement showed that initial interaction came as isolated intermittent bursts at various locations on the bed. The frequency of bursting occurred consistently irrespective of the location along the flat bed. In the case of a dune covered bed, Sutherland observed that motion occurred linearly in the troughs and stagnation regions of the dune, seen in Figure 2.7 as position 4 and 5 respectively. In the stagnation region, interactions were observed to be more violent and extensive than those in the trough of the dune, suggesting that grain motion may be a result of the presence of jet-like burst of fluid impinging onto the granular bed[31]. Adding, that in the stagnation region grains not only moved in the downstream direction, but latterly and even upstream of the mean flow. In the trough region of the dune, Sutherland noted that the grains were in a constant state of agitation, showing no preferred in direction and described their movement as oscillatory in nature.

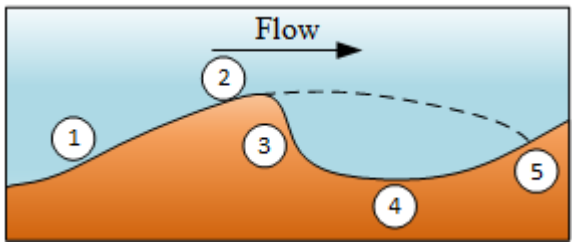

Figure 2.7: *definition sketch of a dune profile. (1) upstream slope, (2) crest, (3) lee slope, (4) through, (5) stagnation region. Adapted from Sutherland[31]*

Sutherland's conclusions concerning the granular bed during high rates of sediment transport are of interest. It was identified that turbulent eddies impinged onto the surface of the granular bed. Additionally, he attributed the swirling motion within these eddies, and the resulting drag force exerted on the grains to responsible for their acceleration. The entrainment of grains from a granular bed due to sweep impacts and the accumulation of grains along areas of low-speed flow are seen as longitudinal ridges. William and Kemp observed that the longitudinal ridges were formed as a result of the decay of sweep impacts.

It was proposed that when a bed defect reached a critical height, flow separation would occur, the reattachment point would then begin erosion at a new location upstream of the bed defect[32] (shown in Figure 2.8).

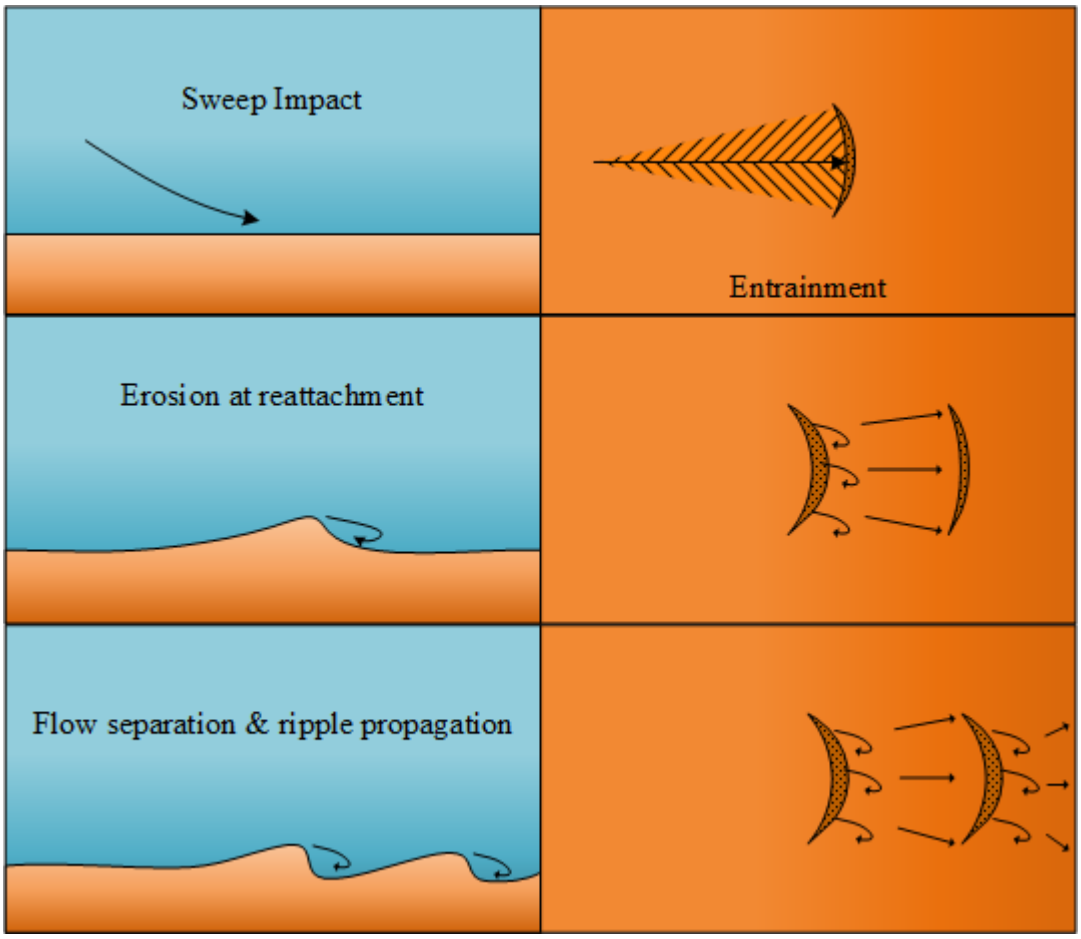

Figure 2.8: *Model for the development of bed defects from individual sweep impacts and the growth of current ripples in sand grade sediment. Adapted from Best[29]*

As shown by William and Kemp, the initial formation of a bed-defect and the resulting flow separation, and subsequent reattachment of flow onto the bed, plays an important role in the formation of various bedforms. Work by Nelson et al. presented a significant step forward in the quantitative identification of the significance of flow separation on the development of these bedforms. For unsteady non-uniform flow, Nelson et al. concluded that magnitude and the frequency of turbulence near the bed resulted in considerable changes in bedload transportation, while variations in bed shear stress were seen to remain mostly unchanged. Concluding that shear stress is not a suitable parameter to determine subtle morphological interactions between erodible beds to varying flow conditions[23].

Experimental work by Diplas et al. looked at the role of impulse on the initiation of particle movement. A metal sphere ranging between 4 – 8 mm were placed atop of Teflon spheres of the same size range, impulses generated by turbulent flow on the sphere was recorded using an electromagnetic which measured its displacement relative to its original position. Diplas et al. determined that in turbulent flow conditions, it is not only the applied force on the particle but the duration of the force that determines the initiation of particle movement, underpinning the importance of impulse in particle movement under turbulent flow conditions[33]. An expansion of the work down by Diplas et al., was undertaken by Celik et al. This work identified that impulses caused by turbulence need to have both sufficient force and time to dislodge a particle. Furthermore, it was shown that the magnitude of drag force acting on the particle plays a part in grain motion, but that there was a strong dependency in the magnitude and duration of the applied force on the particle due to impulses. Suggesting that in turbulent flow conditions the turbulence fluctuations, described as impulses, are the main mechanism by which grains dislodged from a bed[34].

In summary, the effects of turbulent flow condition that are present in this study have been reviewed. The importance of sweeps and bursts, for the transfer of energy, momentum and vorticity from inner to the outer regions of the turbulent boundary layer[25], and their spatially, and temporally random nature[26] is emphasised for the role it plays both in the production of turbulent structures, but also of the production of bed perturbations.

The production of bed perturbations is a result of the ejection of low momentum fluid from between grains making up the bed, and the agitation and entrainment of grains into the mean flow by vortex-loop breakdown seen as bursting[28]. Larger structures such as ridges and dunes develop as a result of random perturbation, their growth sustained by the ejection and accumulation of grains due to these turbulent flow structures.

Interactions between the mean flow and granular bed in the work presented undergo several phases; a characteristic of these interactions is the formation of dunes. Turbulent flow over a dune covered bed and the resulting flow separation, coupled with violent jet-like bursts of fluid impinging onto the granular bed at the reattachment point[31] is responsible for the process of dune propagation[32], the process shown on Figure 2.8. The flow reattachment point is unsteady and non-uniform, this results in considerable changes in bedload

transportation due to the magnitude and frequency of turbulence near the bed[23], in contrast, bed shear stress remains mostly unchanged. Shields parameter which is described by the ratio of shear force over the buoyancy applied on a grain does not account for the force fluctuations and therefore is not sufficient to describe the phenomenon at incipient condition[34]. Grain movement and dislodgment, under turbulent flow conditions, is determined by the applied force, and duration of the force[33], seen as impulses which are a result of turbulent fluctuations[34].

2.4 Secondary flow instability

Pioneering experimental work into the effects and description of secondary flow was the seminal work of Eustice[35] when investigation into flow resistance for straight and curved pipes, shown in Figure 2.9a. The identification of a transient threshold velocity, commonly known as the critical velocity, was made. This critical velocity was shown to occur at higher flow rates in curved pipes when compared to that of straight pipes. Through experimentation, the velocity in curved pipes was shown to be proportional to the fluid velocity raised to the power "n"[35]. Attempts to determine the cause of discrepancies between the laws that govern flow in a straight pipe and those of curved pipes, initiated the use U-shaped curved passage (Figure 2.9b) used in combination with streamlines to visualise and describe the secondary flow behaviour. Eustice observed that when a streamline approached the outer-wall of a curved pipe, the streamline broke up into two separate bands, rotating in opposite directions towards the inner-wall about the centre line of the curved pipe[36].

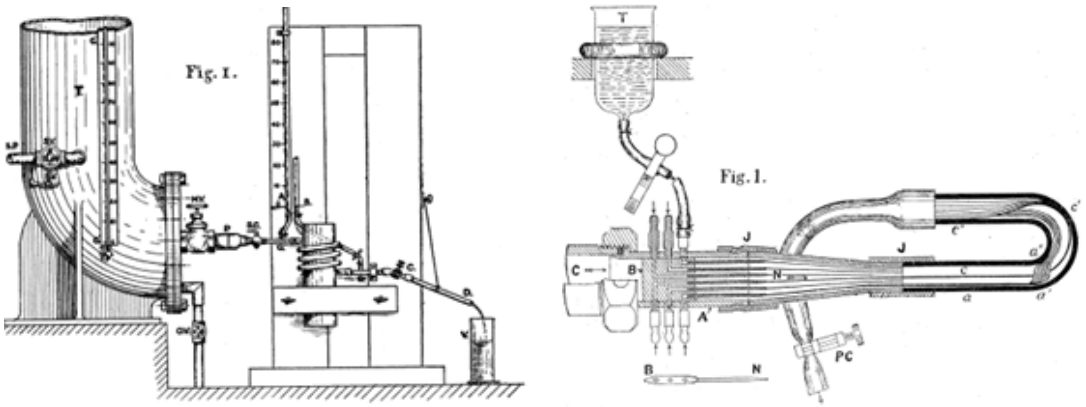

(a) (b)

Figure 2.9: *Experimental arrangements used for the investigation of secondary flow by Eustice[35][36].*

Following on the discovery of Eustice, an attempt to analytically model Eustice's experimental findings were made by Dean[37]. Dean modelled the flow of incompressible fluid through coiled circular pipes and reported good qualitative agreement to experimental results produced by Eustice, who used a small curvature ratio. The curvature ratio is the ratio between the pipe diameter and the radius of curvature of the pipe bend ($\Gamma = \frac{D}{R}$). Additionally, the non-linear relationship between pressure drop and Reynolds number in

curved pipes identified by Eustice was confirmed by Dean. Dean produced an analytically stream-function represented as ΓRe^2. The modelled developed, allowed for the illustration of the spiral nature of streamlines in curved passages under laminar flow conditions, seen in Figure 2.10.

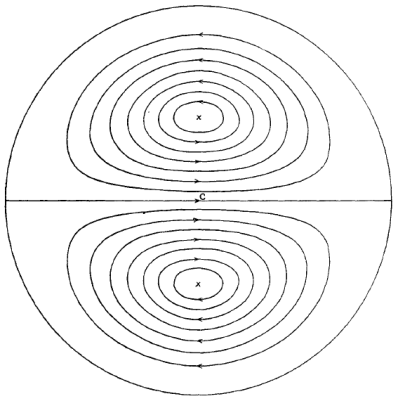

Figure 2.10: *Dean's stream function modelling secondary flow cells in a bent pipe[37]*

Further development by Dean of his original model[37] produced an analytical correlation which describes the effects of pressure drop on mean flow velocity in curved passages for varying curvature ratios, now known as the Dean number (K):

$$K = \sqrt{\Gamma}\ Re \tag{2.1}$$

Dean explained that there exists a fundamental difference between flow instability observed in curved passages and the turbulence described in straight passages, with flow instability occurring in curved passages at conditions below that of threshold conditions in straight passages.

Furthermore, that the parabolic velocity profile that exists within straight channels does not hold for curved channels. Dean's proposed criterion was later investigated by White[38] through an extension of the work done by Eustice. White experimentally investigated the relationship between the criterion proposed by Dean and pressure drop over a wide of Reynolds numbers (0.06 to 40000). White confirmed that the increased internal resistance to flow observed in curved pipes is a result of the internal circulation in the cross-sectional plane superimposed on to that of the axial flow.

The effects of secondary flow instability as investigated by the previous authors were limited to curved passages with circular cross-sections. A notable experimental investigation using curved square ducts within the laminar flow regime was undertaken by Baylis[39], who focused on flow resistance and boundary layer behaviour, and Humphrey[40], which used a curved duct with a 90° bend and a curvature ratio of 2.3. Humphreys work identified the occurrence of secondary flow instability for Dean numbers ($K > 125$), originating within the initial 25° position along the duct and appearing at the outer-wall[40].

Humphrey's extended this work using the same experimental setup to investigate the effects of the curved duct under turbulent flow conditions[41]. Similar to that of laminar flow condition, the turbulent flow case produced strong cross-stream motion which developed into a pair of counter-rotating vortices[41]. It was noted that the position of maximum velocity moved away from the outer-wall towards the inner-wall after the 71° position along the curved square duct.

A radial extension from a 90° bend to that of a 180° bend was used by Hille et al[42] to experimentally investigate the development of secondary flow under laminar flow conditions in a square duct. Hille et al showed that the streamwise flow component was connected to strong momentum transfer along the outer-wall between radial positions of 0 – 60°[42]. Moreover, the formation of an additional pair of vortices was identified from 108 – 171° along the curved duct; showing increased secondary flow instability within this region.

A numerical and experimental investigation using a 180° curved square duct operating in the turbulent flow regime was undertaken by Lacovides et al.[43]. A substantial change in the streamwise velocity was identified past the 90° radial position, which was attributed to the convective effects of secondary flow instability transporting low momentum fluid from the outer-wall towards the inner-wall of the curved duct[43], confirming observations made by Cheng et al[44]. Additionally, Lacovides et al. noted that that flow at the 135° was similar to that observed at 90°, suggesting that changes in the secondary flow pattern and subsequent formation of localised troughs in the velocity stream are the first stages in the breakdown of secondary flow into multiple smaller-scale vortices. This breakdown was captured numerically at the radial position of 135° were five such vortices were seen to form[43].

2.4.1 Effects of Aspect and Curvature Ratio

Numerical analysis was done by Cheng et al.[44, 45] using Aspect ratios of 0.5, 1, 2 and 5 with Dean numbers (K) ranging from 5 – 715 underpinned the effects of Aspect Ratio on secondary flow instability. Cheng at et concluded that the duct aspect ratio as a critical geometric parameter when determining the formation of addition counter-rotating vortex pairs, shown in Figure 2.11 with the additional vortex pair shown located at the outer-wall.

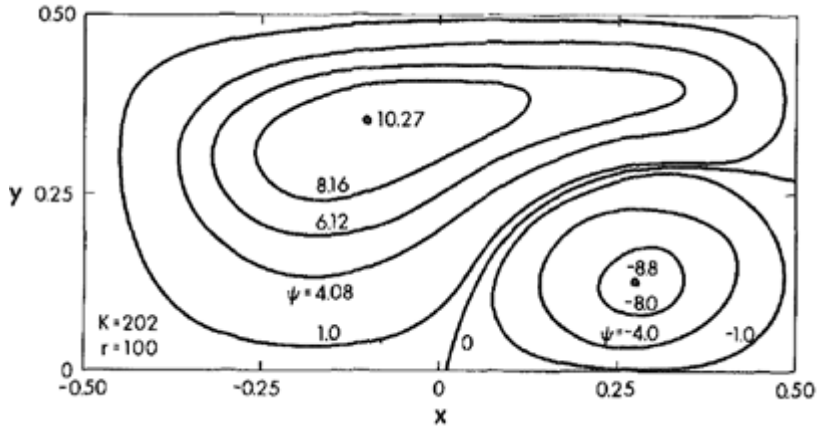

Figure 2.11: *Stream functions showing the formation of an addition vortex pair located at the outer-wall for a square duct[45]*

An experimental examination of flow characteristics was undertaken by Sugiyama et al. using flow visualisation techniques[46]. Using aspect ratios ranging from 0.5 – 2.5 and curvature ratios ranging from 5 – 8, Sugiyama et al. captured the development of additional vortices due to secondary flow instability, shown in Figure 2.12. Additionally, for an aspect ratio of 2 Sugiyama et al. highlighted the dependence of secondary flow instability on curvature ratio, showing that increased curvature ratio corresponded to a decreased critical Dean number at a given aspect ratio. Furthermore, Sugiyama et al. suggested that the critical Dean number is highest for Aspect ratios in the range of 2 – 2.5[46].

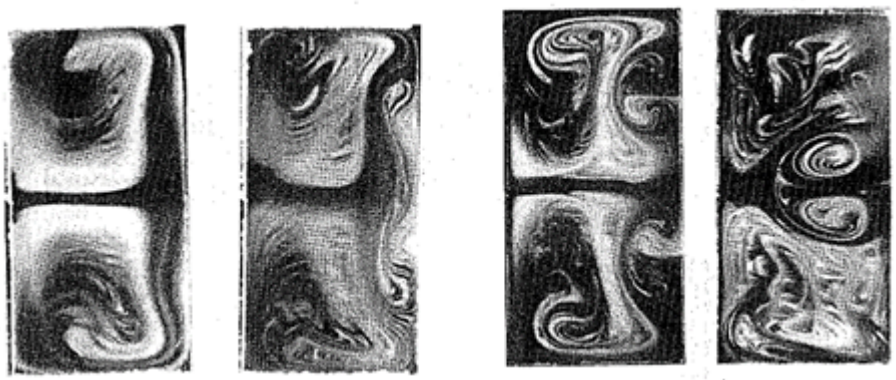

Figure 2.12: *Flow visualisation of the formation of Dean vortices[46].*

Characterisation of flow in curved ducts for both heated and isothermal cases using numerical simulation was investigated by Chandratilleke and Nursubyakto[47]; the results of interest are those computed for the isothermal curved ducts. Results obtained for Aspect ratios of 1 – 8 over Dean number of 20 – 500, underpinned relationship between Aspect ratio and the number of Dean vortices formed; with an increase in the Aspect ratio seeing an increase in vortex formation, this relationship is seen in Figure 2.13 showing aspect ratios of 2 and 4 respectively.

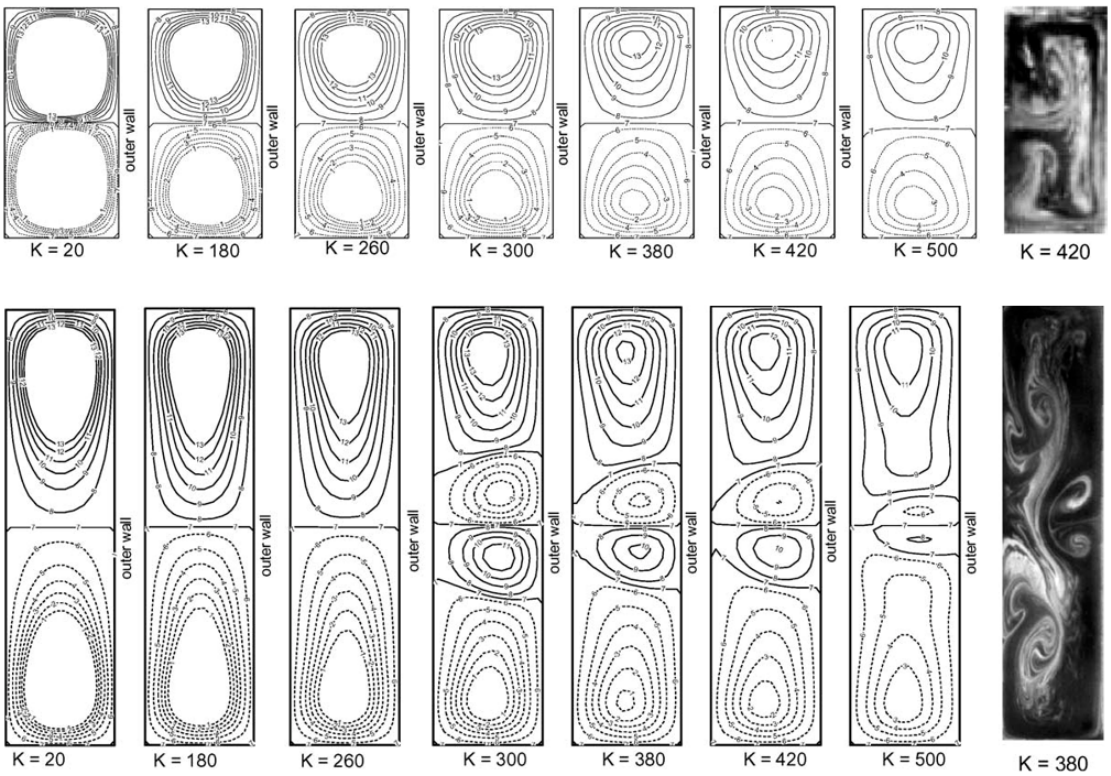

Figure 2.13: *Comparison of computed flow through a curved duct of Aspect ratio 2 and 4[47].*

The majority of numerical studies investigating secondary flow instability in curved ducts were limited to 2-dimensional analysis. Using the non-dimensionalised helicity function (H^*), Chandratilleke et al.[48] provided an improved simulation model based on 3-dimensional vortex structures. A parametric analysis investigating the effects of flow rate, aspect ratio (Ar = 1-6) and curvature ratio (γ= 4 and 5) with successful 3-dimensional representation of counter-rotating vortex structures was produced (Figure 2.14a and 2.14b). Additionally, model validation against results obtained by Cheng et al.[45] was determined to be in excellent agreement, reinforcing the importance of geometric parameters such as aspect ratio and curvature ratio on secondary flow instability.

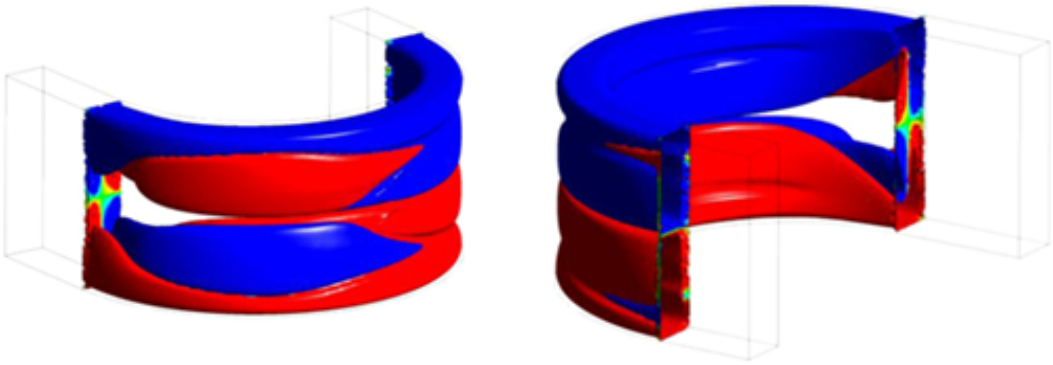

(a) (b)

Figure 2.14: *3-Dimensional visualisation of vortex cores in a curved duct[48].*

Thus far the literature presented has been limited to that of single-phase flow, a notable exception is the preliminary investigation into multi-phase flow undertaken by Chandratilleke and Nadim[49]. Fluid-granular interaction was numerically modelled using a Eulerian model and k-ε turbulence closure. The importance of shear forces as a critical parameter for determining the shape and position of vortices in a curved duct were identified[49]. As seen in Figure 2.15, the transitional nature of fluid-granular interactions was captured, showing mutually influenced relationship between secondary flow instability and the granular bed profile.

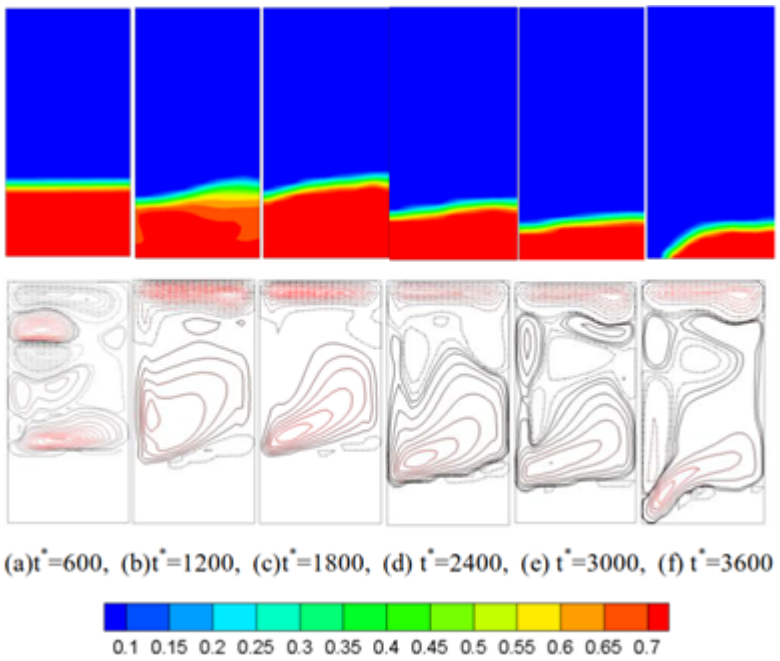

Figure 2.15: *Deformation of the granular phase bed and the helicity function of the liquid phase[49].*

2.5 Summary of Literature Survey

According to reviewed literature, an extensive knowledge base is reported on secondary flow behaviour in curved ducts with many analytical, experimental and numerical modelling studies, and a wide range of applicable methodologies. However, studies on granular bed erosion in the presence of secondary flow remain unexplored owing to the mechanistic complexities embedded in this flow situation highlighted in the literature survey. Accordingly, literature reporting on the erosion-sedimentation process in curved ducts is practically non-existent. With the majority of published literature attempting to address the long-standing problem regarding the threshold of grain movement, typically using straight open channel arrangement. When secondary flow behaviour was investigated, the flow passage is of a curved open channel arrangement. A closed ducted configuration with fluid passage geometry selected to enhance secondary flow instability has yet to be addressed. The current study addresses this shortfall through an experimental and numerical investigation of erosion and sedimentation processes in a curved passage with the passage aspect and curvature ratio selected to enhance interaction between granular material forming the bed of the flow passage and the induced secondary flow.

Chapter 3

Experimental Method and Considerations

This chapter describes the experimental apparatus utilised to examine the characterise erosion and sedimentation due to secondary flow induced fluid-granular interactions. Detailed description is provided of the experimental procedures employed to determine parameters for experimental investigation, precautions taken and the measurement accuracy of both granular bed height and flow rate are shown.

3.1 Apparatus

The apparatus used for experimentation is shown in Figure 3.1 and consists of a transparent curved fluid duct, referred to as the curved test section (1). The curved test section has a curvature ratio of 5, and a rectangular cross-section with an aspect ratio of 1.5 when a granular bed is placed inside. The curved test section geometry induces interaction between a granular bed (quartz sand) and secondary flow structures formed due to curvature effects. A straight flow entry duct (2) with a swirl impediment Chamber (9) are utilised to remove the effects of swirl prior to entry into the curved duct. A water circulation loop comprising a 3-phase centrifugal pump (4) controlled by a variable speed drive (VSD) provides fine flow rate control. Measurement of flow rate is recorded via either the rotameter (5) or the magnetic flowmeter (6) depending on the flow regime being investigated. To provide clean sediment free fluid, a settling tank (10) is employed, with inlet side coming from straight flow outlet duct (3). Addition flow rate adjustment if required is achieved using a flow control valve (7) with a flow directional valve (8) (11) allowing selection between the two flow meters.

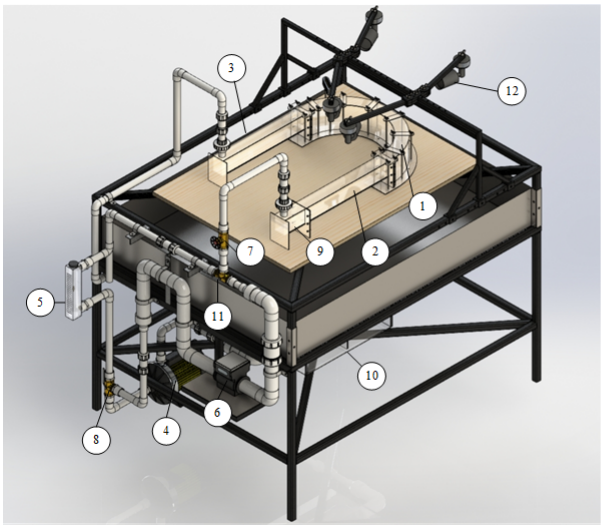

Legend

1	Curved test section
2	Straight entry duct
3	Straight outlet duct
4	Centrifugal pump
5	Rotameter
6	Magnetic flowmeter
7	Control valve
8	Directional valve
9	Swirl impediment Chamber
10	Settling tank
11	L-Port
12	Video cameras × 4

Figure 3.1: *The experimental Set-up with the Flow Loop.*

A traversing arrangement of four laser beams is used for illuminating and profiling the granular bed surface. Four position-adjustable video cameras (720p resolution) (12) are mounted around the curved test section to continuously monitor the sand bed surface behaviour and to capture the bed profile demarcated by the laser spots at selected locations. These camera views allow recording and cross-validation of bed profile data at pre-selected angles and positions along the curved duct under different conditions of water flow. The entire test set up is well sealed with suitable adhesive and O-rings to prevent any leakages. However, provisions are made in the design for easy disassembly of the test section to arrange the granular bed after each test and for cleaning the curved test section, when necessary.

A process flow diagram describing the operation of the water circulation loop is shown in Figure 3.2. Operation of the apparatus in both the laminar and turbulent flow regimes is achieved by switching between the two fluid circuits. The laminar fluid circuit (Red) using the Rotameter for flow rate measurement and the turbulent fluid circuit (Blue) using the Magnetic flowmeter.

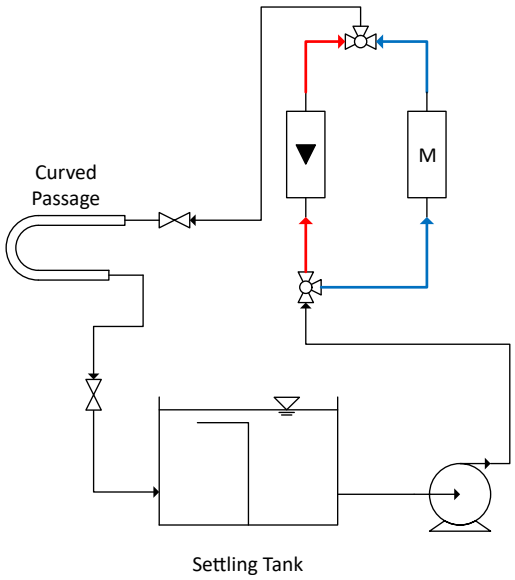

Figure 3.2: *Apparatus process flow diagram.*

3.2 Apparatus design

Key apparatus parameters and requirements for the successful investigation of interaction between the granular bed and secondary flow structures is discussed in this section. The selection of the curved test section geometric parameters such as Aspect ratio and Curvature ratio is discussed. Methods for ensuring the effects of swirl are minimised, and the maintenance of particle free supply to the curved test section is outlined. Additionally, the selection of flow rate control device, flow supply and flow rate measurement is described.

3.2.1 Curved Test Section

The Curved Test Section (1) is designed and developed to deliver a practically steady flow regime of secondary flow behaviour in a range that has been well investigated for single-phase fluid flow. Therefore, duct aspect ratio, duct curvature ratio is carefully chosen to satisfy the specific flow requirements based on the published data; discussed in Section 2.4.

The resulting Aspect ratio is 1.5 when the granular bed is placed into the curved test section. Changes to the granular bed depth during experimentation, result in Aspect ratio changes, with the granular bed removed, the maximum Aspect Ratio of the curved test section is 2.5.

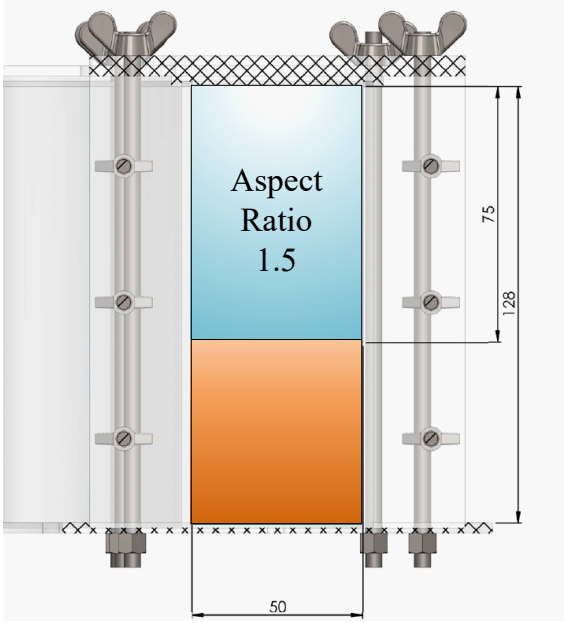

Figure 3.3: *Cross-section showing the Aspect ratio of the filled Curved Test Section.*

Figure 3.4 illustrates the detail arrangement of the curved test section which is 225 mm in radius with a cross-section of 125 mm × 50 mm. A uniform and flat granular sand bed of height 50 mm forms the bottom of the curved test section over which the working fluid, water flows. The water is directed to the curved passage through the 500 mm long straight rectangular entry duct (2) having matching cross-sectional dimensions to the curved test section. The bottom of this entry duct is level with the top surface of the sand bed in the curved duct, ensuring smooth flow entry. The straight outlet duct (3) is also similarly arranged to receive the water flow smoothly from the test section.

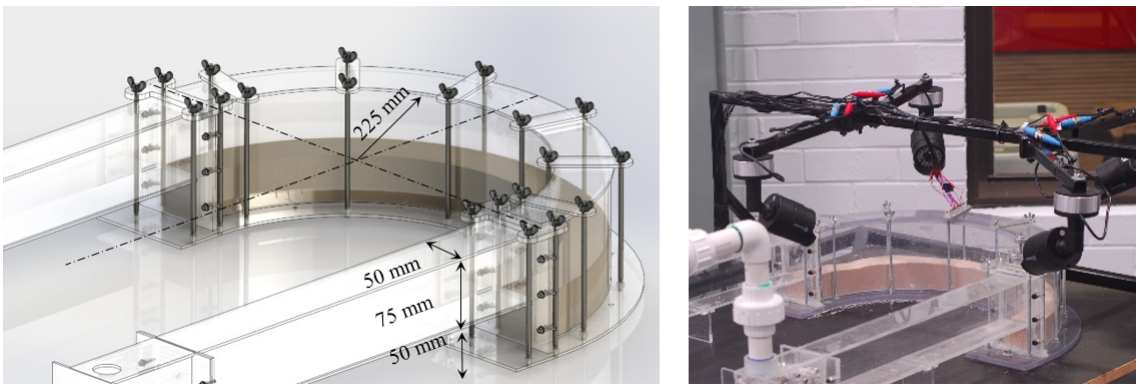

Figure 3.4: *Curved test section with granular bed.*

3.2.2 Swirl Impediment Chamber and Entry Duct

Elimination of swirl from the curved test section is necessary to exclude any external sources of secondary flow which may affect fluid-granular interaction in the curved test section; additional secondary flow instability due to swirl further compounds the complex nature of these interactions. Swirl elimination is achieved by using a Swirl Impediment Chamber (9) which is incorporated into the entry duct and filled with plastic beads, as illustrated in Figure 3.5.

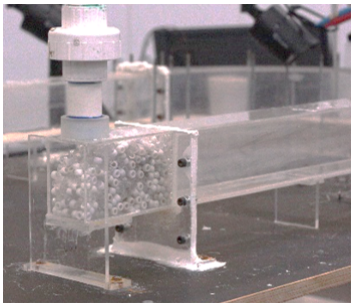

Figure 3.5: *Swirl Impediment Chamber and plastic beads.*

Consideration is given to achieving fully developed flow, selection of the inlet duct length is based on practical psychical limits. The combination of the swirl impediment devise and the sudden change in flow direction seen at the entrance to the curved test section, create conditions such that fully developed flow at the entrance to the curved test section has a negligible effect past 10° along the curved duct.

3.2.3 Particle-free inlet fluid supply

A particle free supply of fluid to the curved test section is vital. Supply fluid carrying particles could induce premature erosion due to the entrained particles impacting the granular bed. Additionally, at lower flowrates these particles may be deposited along the straight inlet duct accumulating at the inlet to the curved test section creating an uneven bed profile, the results of which are discussed in Section 4.1.6.

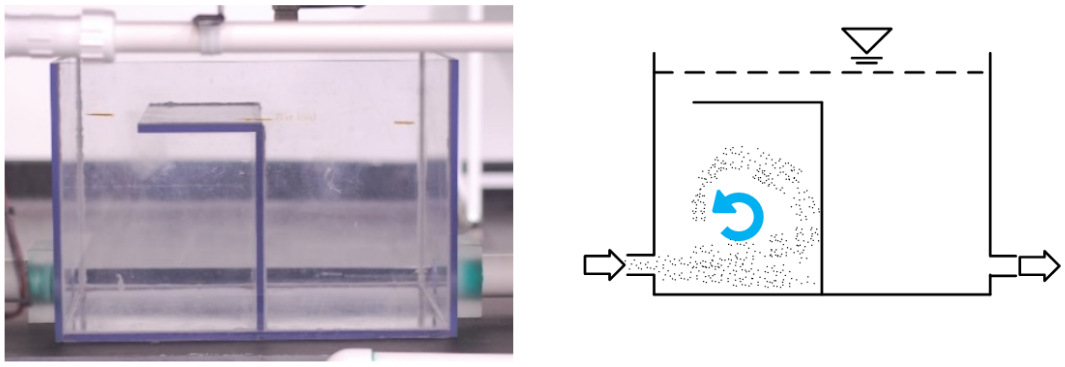

(a) (b)

Figure 3.6: *(a) Settling tank , (b) and Separating arrangement in settling tank.*

A Settling Tank (10) is used, to achieve the required particle-free inlet fluid supply. As illustrated schematically in Figure 3.6b, entrained particles are separated and contained, prior to flowing back to the pump, using an inverted L-shaped baffle. This arrangement allows for effective settling of particles as small as 100 μm. As an additional precaution in preventing suspended particle circulation, a mesh filter is also fitted to the inlet pipe of the Swirl Impediment Chamber. Additionally, both the inlet and outlet pipe (internal diameter of 48 mm) connecting to the Settling Tank are sized to reduce the flow velocity, and promote particle settling. The settling tank water surface is exposed to the atmospheric pressure to maintain constant suction head to the pump.

3.2.4 Flow rate measurement

A wide range of flow rates are required to investigate the effects of secondary flow on a granular bed of different size ranges. Therefore the apparatus requires flow rate measurements in both the laminar and turbulent flow regimes. Additionally, selected flow meters must operate accurately and reliably under conditions which may contain small percentages of sediment in the fluid flow.

These requirements are met using of two flow meters, a Rotameter [Omega FL-2081] deployed for the lower range of 4-36 L/min corresponding to laminar flow, while the magnetic flowmeter [Omega FMG-800/2] is employed at a higher range of flow rate at 25-1130 L/min. The two flow meters provide a flow rate measurement accuracy of ± 2 % and ± 1 % for the Rotameter and Magnetic flow meter respectively. Selection of a magnetic flowmeter allows for reliable

flow rate measurement, even under conditions were the measured fluid contains high concentrations of solid particles.

3.2.5 Flow supply and control

A 3-Phase centrifugal pump [Lowara CEA210/2V] is used to maintain water flow through the fluid circuit, the flow rate being controlled directly adjusting the electrical supply frequency of the centrifugal pump using a variable speed drive (VSD). This arrangement allows flow rate selection to be achieved without the use of valves providing greater flow rate resolution. Additionally, use of a VSD for direct flow rate control prevents the formation of trapped air slugs and bubbles inside of the curved test section, the presence of which is detrimental to the non-intrusive measurement technique.

The VSD [IMO iDrive2 XKL 1.5kW] controls the supply frequency to the centrifugal pump; this frequency is set using a digital control panel. The VSD has a frequency resolution of 0.01 Hz, providing a high degree of control and enables the selection and adjustment of flow rate to be carried out accurately. Furthermore, interaction between secondary flow and the granular bed result in a changing bed profile, resulting in a change in friction losses inside the curved test passage; the result of which is a fluctuating flow rate. Use of a VSD allows for the flow rate to be adjusted precisely to maintain the desired flow rate within acceptable bounds.

An addition advantage is that a VSD enables a soft start to the experiment; this is achieved by the VSD slowly increasing the frequency supplied to the centrifugal pump until the pre-selected frequency is reached. This function is vital to the experimental process as sudden velocity fluctuations can result in the granular bed being disturbed prematurely before commencing the experiment.

3.3 Experimental procedure

The experimental procedure is outlined and explained in this section. Aspects such as sand sieving for each granular test bed, camera positioning and calibration, flow rate selection and control, and granular bed preparation prior to experimental runs are explained and outlined. The experimental procedure is outlined in Figure 3.7, showing the stepwise process followed for all experiments presented in this work. Key decision points of the experimental procedure are indicated and the path taken at these critical junctures shown.

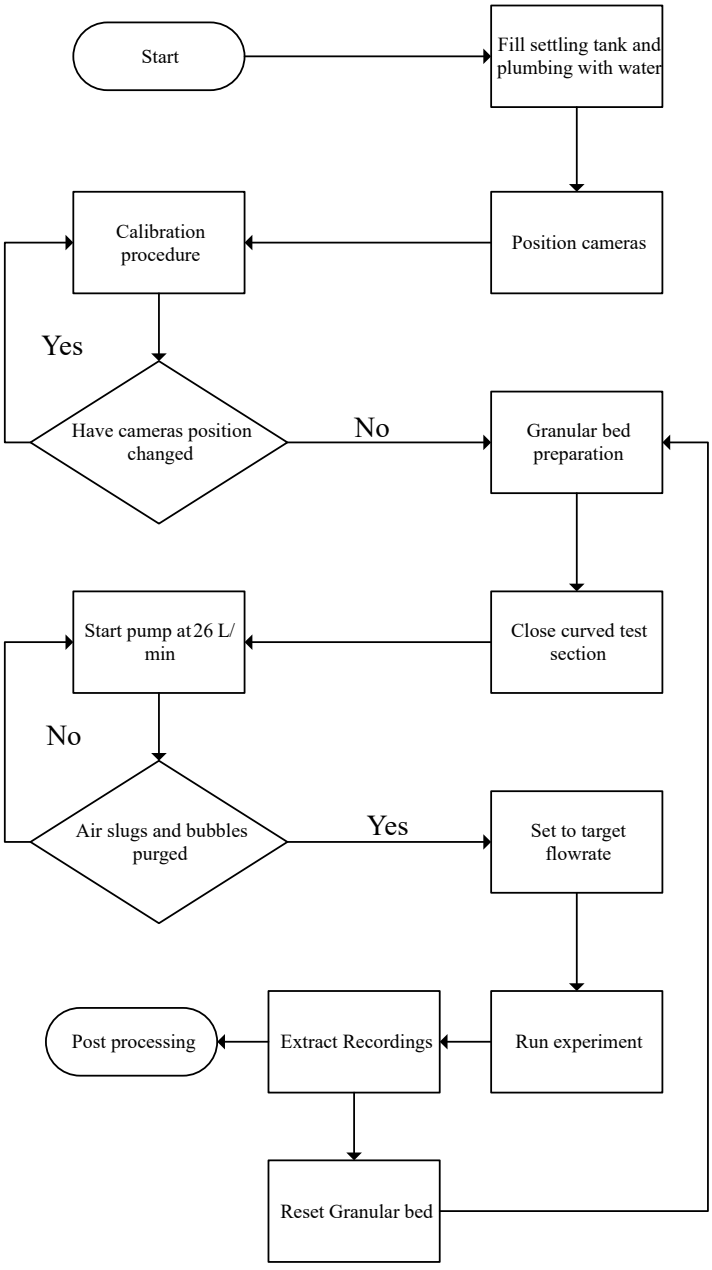

Figure 3.7: *Process diagram of experimental procedure.*

3.3.1 Sand sieving

The granular material consists of quartz sand, refer to Table 3.2 for material properties. Granular beds of three size ranges, 150 – 300 μm, 300 – 425 μm and 425 – 1180 μm are utilised for experimentation. Before sieving, quartz sand was collected and dried in an oven at a temperature of 105 °C for 12 hours. This process removes moisture from the sand, as moist sand will result in the presence of finer unwanted grains in the final granular bed due to their adhesion to the sieve mesh and larger grains. Fine sand and silt grains (<150 μm) are removed as material comprising of grains less than 100 μm can no longer be considered granular in behaviour[2]. This is due to the dominance of Van de Waals and capillary forces relative to externally applied forces and therefore falls outside of the scope of this work. Sieving consisted of using a mechanical sieve, until enough sieved sand was obtained to allow for experiments to be run, including any losses during bed resetting.

Sieve analysis for the un-sieved sand provided by the supplier is provided in Table 3.1 showing the grain size distribution, with physical properties provided in Table 3.2.

Table 3.1: *Bulk un-sieved sand grain size distribution, with yield for each sieving run*

Sieve Analysis		
Sieve Opening Size (mm)	% Passing (% Yield)	Supplier Specification Limits
4.75	-	100
2.36	-	95 - 100
1.18	100 (0)	90 - 100
600	86 (14)	72 - 100
425	55 (45)	-
300	25 (75)	17 - 37
150	1.7 (98.3)	0 - 7
75	0.1 (99.9)	0 - 5
Pan	0	-
Clay and Fine Silt	3	≤ 4

Table 3.2: *Physical properties of quartz sand*

Physical Properties	
Grain Specific Gravity	2.59
Dry Specific Gravity (Max)	1.86
Dry Specific Gravity (Min)	1.56
Clay and Fine Silt	3%
Gross Moisture Content	3.20%
Fineness Modulus	1.9

3.3.2 Calibration and Camera Positioning

Prior to the commencement of experiments the position of the various cameras was set and checked to ensure that the investigation area was fully visible and free of obstruction. Correct camera alignment was achieved by positioning the cameras first in the horizontal plane using the camera arms illustrated in Figure 3.4, once in position fine adjustments to the cameras horizontal position can be made by rotating the cameras themselves; vertical adjustment is then made using each individual camera mount. Once cameras positions are finalised, they are locked into place, ensuring that their position relative to the area of interest is constant throughout the experiment.

After cameras positioning had been completed and the respective cameras locked into place. The calibration process is then started by filling the curved test section with water; this is done to account for refraction due to the presence water, seen as image distortion. The gauge block (Figure 3.9a) is then placed into the curved section at the area of interest, and the curved test section closed, the laser rack is then positioned ensuring that the lasers are optimally focussed providing as small a projected laser point onto the gauge block. Once a calibration image has been taken from the respective camera, the gauge block is moved to the next area of interest. Calibration images are then extracted and used in the determination of calibration equations for each laser point, discussed in Section 3.5.1.

3.3.3 Granular bed preparation

Granular bed preparation is a vital element in the experimental procedure with inconsistent bed preparation leading to a lack of repeatability of in experimental results. A consistent bed preparation process is employed in order to mitigate the stochastic nature inherent to granular materials.

The bed preparation process considers keys properties affecting the granular bed which must be understood and addressed. The first is the removal of trapped air from the granular bed which creates localised areas of lower volume fraction, increasing the granular bed's sensitivity to premature erosion events. Additionally, trapped air coalesces to form bubbles within the granular bed itself, which during experimentation, burst forming cavities which later collapse, creating artificial surface perturbations educing premature erosion. The removal of trapped air is achieved by filling the curved test section with water prior to laying the granular bed. The granular bed is then poured slowly along the curved test section until enough has been added to allow for a bed of 50 mm in depth along the test section to be laid out. The loose granular bed is then agitated; this is done by stirring the submerged bed to allow residual trapped air to escape. The granular bed is then is levelled out evenly and the fluid drained from the curved test section leaving a thin surface layer of fluid above the granular bed.

The purpose of bed levelling and the minimisation of bed perturbation is to provide a bed surface which is level with minimum surface perturbations. A level surface is essential as perturbations along the fluid-granular interface result in flow separation and consequently, erosion at the source of the perturbation leading to unpredictability with respect to experimental results. Additionally, smaller surface perturbations which are a result of granular bed preparation and the bed grain size are managed within practical limits as a perfectly smooth and flat bed is impractical. The bed levelling process commenced once the air removal procedure had been completed. This process utilised a Styrofoam block cut to the fit within the curved test section; the granular bed was then raked until the desired bed height of 50 mm was achieved along the entire test section. Following this, a light tapping motion was used to remove and perturbation created due to the bed racking process. The curved test section was then slowly filled from the outlet side (see Figure 3.4), ensuring that the granular bed was not disturbed by the fluid onrush.

The final consideration is the effect of bed ageing; this phenomenon is a result of the granular material settling over time. The effects of a constant force applied on the bed due to hydrostatic pressure have been shown in literature to affect the stability of a submerged granular material. The result of which is a greater force being required to penetrate a bed that has been aged, ageing had been shown to occur within the first 24 hours for submerged beds[50]; conversely, a bed that is loosely pact is far more likely to erode prematurely. Both these factors are important as excessive bed ageing would delay the onset of erosion and therefore effect results at lower flow rates. For loosely packed bed this would be seen as premature erosion at lower flow rates and excessive erosion at higher flow rates. To avoid any excessive bed ageing, but also to ensure the granular bed is not loosely packed, the prepared curved test section, was filled with fluid, closed and left to rest for 1 hour, this improved repeatability of experimental results.

3.3.4 Flow rate Selection and Control

Flow rate through the curved duct was controlled directly via the pump; this is in turn controlled via the VSD's output frequency. It is therefore critical that for each desired flow rate a corresponding VSD output frequency is determined. Due to the dynamic nature of fluid-granular interactions and constant bed reshaping, the system does not have a constant pressure drop across the curved test section. As experiments cover multiple flow rates and granular bed grain sizes, the only reliable method to determine this relationship was a trial-and-error approach.

Identification of the initial flow rate for grain displacement was achieved by gradually increasing the flow rate until such conditions are reached. Additionally, this allowed for the determination of minimum initial flow rate that maintained steady state conditions in the curved test section from which flow rate could be increased, using the VSD's soft start capabilities allowing for an undisturbed granular bed before experimentation.

Higher flow rates are determined by using a trial bed; a bed prepared as per the bed preparation procedures, but not used for obtaining experimental results. The frequency is increased until the desired flow rate is achieved and recorded for later use. This process was repeated multiple times as overshoot was a common issue, particularly for higher flow rates.

Prior to beginning an experiment, the flow rate was brought to a flow rate of 27 L/min safely under the flow rate at which the granular bed was disturbed for all

grain sizes examined. The low flow rate used also served an additional function as this steady state period allowed for the purging of any air bubbles or slugs within the curved test section. The desired frequency of the VSD is then selected, and the flow rate is increased over a short period to the desired rate. Fine adjustment to the VSD output frequency is made during the experiment to maintain the desired flow rate, with flow rates being recorded progressively throughout the experiment, uncertainty related to fluctuating flow rate is discussed in detail in Section 3.7.4.

3.4 Measurement Technique

A method to determine the main feature of interest in the current experiment, namely the shape of granular bed interacting with fluid, must be non-intrusive. The measurement technique must allow for fluid-granular interactions to be qualitatively and quantitatively evaluated, without disruption to either the flow field or granular bed, providing both temporal and spatial data. The technique employed is selected to meet the experimental requirements and restrictions of the current case. These requirements are:

- Allow non-intrusive quantitative examination of a granular bed inside a closed curved test section,
- Provide continuous measurements without flow interruption;
- Provide high temporal and spatial resolution; and
- Allow for accurate and reliable measurements.

3.4.1 Selection Process

The requirement for a non-intrusive measurement technique capable of capturing the granular bed profile, suggests the employment of either optical and acoustic techniques. The selection process for the measurement technique employed is discussed.

The use of ultrasonic transducers for both velocity field observations, and granular bed profile is technically possible this technique is excluded based on the prohibitive cost of this equipment. In addition, ultrasonic methods are adversely affected by the scattering that occurs due to sediment transport during extreme erosion events. This scattering introduces noise and severely impacts the accuracy of data obtained using this method.

In contrast, optical methods are more cost-effective owing to the constitute components (lasers and cameras) being readily available in the commercial market. Use of commercially available bed scanning techniques which allow for the maximum bed profile resolution of any technique, introduces additional challenges; this technique is designed for profile measurements of solid objects and is typically calibrated to the operating medium. For measurements to be taken in a submerged environment, the device would need to be designed specifically for this. The presence of multiple media, namely the curved test section lid, the fluid in the curved test section and the granular bed make significant errors inevitable. Additionally, the high degree of scatter seen as noise due to the uneven and porous nature of the granular bed further compounds the use of a commercial bed scanner.

The method employed uses four discrete laser point mounted perpendicular to the region of interest. The advantages of such an arrangement are that discrete points lend themselves well to image processing techniques such as image segmentation and object tracking, allowing for the use of automated extraction of temporal and spatial data. Image processing techniques are discussed in further detail in Section 3.6. Moreover, unlike the commercial bed scanner or acoustic methods, this technique is not contingent on the return of a signal to a receiver.

3.4.2 Bed Profile Measurement

Bed profile measurement consists of utilising four equally spaced Green Class-II lasers mounted perpendicular to the granular bed and positioned over the cross-section of interest. The use of four lasers was determined by the dimensional constraints imposed by the curved channel. Smaller laser diodes allowed for greater spatial resolution but proved unreliable due to their small size and tendency to overheat. Additionally, these smaller laser diodes produced red light; this is not well suited to this experiment as the red light is diffused within the flow passage, producing a weak signal and an increase in measurement error. The Green Class-II lasers have a duty cycle that allows for extended and uninterrupted measurement, this compromise of temporal resolution over spatial resolution is justified as the curved passage has an internal width of 50 mm. Four discrete points provide sufficient bed profile detail and compare favourably to qualitative observations. The laser mount can be positioned along the curved test section from 15° to 165° in 15° increments (Figure 3.8). Additionally, the projected laser points can be focussed individually using adjustable focus lenses that are supplied with each laser. Adjustable focus allows for optimal illumination intensity and minimises the radius of projected points which accordingly reduces the uncertainty of cross-correlation.

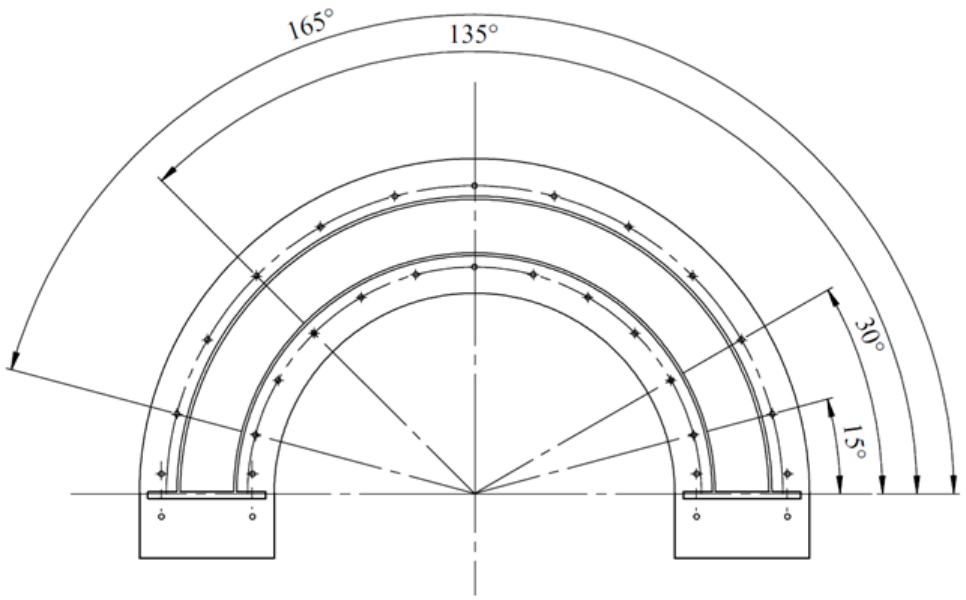

Figure 3.8: *Top view of the curved Test Section, showing radial positioning resolution of 15°*

Due to the dynamic nature of bed variation, the use of a single camera increases the likelihood that segments of the investigation area become obscured during an experiment. To overcome this potential issue, four cameras are installed on an adjustable mounting mechanism allowing two inner-wall and two outer-wall views while the combination of laser mount and camera platform could be rotated along the curved test section to investigate the cross-section of interest. The video cameras record at a resolution of 720p, translating to an image of 1280×720 px in size. The time stamped recordings from each camera are stored on a video encoder, this time stamp is used to synchronise the recorded results from each of the four cameras.

The camera mounting frame allows for each camera to be positioned individually and locked into position. In addition, the various joints along the camera arms have rubber washers placed between then to prevent any transmission of vibration to the cameras. Additionally, the centrifugal pump is placed on the rubberised laboratory floor and is not mounted onto the apparatus frame to further reduce the possibility of and vibrations.

The combined use of illuminated discrete laser points and video recording utilising multiple cameras provides the necessary flexibility and allows for verification of image processing (i.e. cross-correlation) from various references of view. As qualitative trends are observed and interactions predicted, the employment of a single camera is possible. The reallocation of spare cameras allows for the additional cameras to be positioned to provide information on multiple sections of the curved test section, allowing for additional flexibility.

3.5 Calibration Procedure

The calibration procedure forms a vital part of the non-intrusive measurement technique employed. Challenges due to the distortion induced by the test section curvature are solved using a cost-effective, reliable and accurate technique. This is achieved using a gauge block seen in Figure 3.9a, the gauge block is cut to have an inner radius and outer radius to allow for a perfect fit within the curved test section. A reference grid of 2.5 mm × 2.5 mm is attached to the gauge block. The key stages of bed scanning, which is shown in Figure 3.9a, is explained and clarified.

3.5.1 Calibration of space using a gauge-block

A single camera is fixed and focused onto a cross-section of interest; this cross-sectional plane requires correlation to physical dimensions. Correlation is achieved by the use of a gauge block as a dimension reference frame. The gauge block (Figure 3.9a) is a plane with a known pattern of dimensions, the dimensions of interest being those in the vertical axis. These are used to correlate pixels co-ordinates to a known physical height (i.e. attribute of physical space in millimetres). The use of separate laser beams projected perpendicular to the gauge block, and later during experimentation onto the granular bed, ensures that there are no other projection components in the radial and axial direction. Any displacement of the laser point is therefore in the vertical direction. Additionally, this calibration is conducted under experimental conditions; with a closed, water-filled curved test section. Therefore, accounting for distortion resulting from the inner and outer-wall curvature, camera lens curvature and the fluid-filled curved test section.

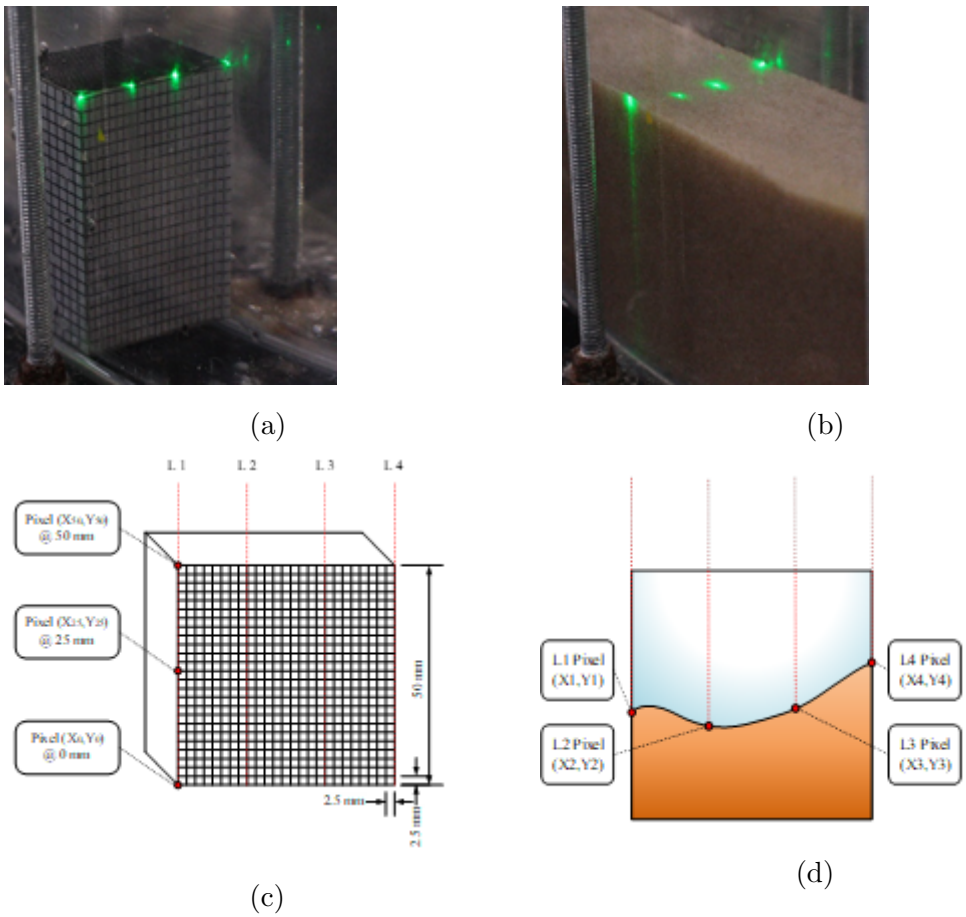

Figure 3.9: *(a) Calibration Space , (b) Illumination and capturing , (c) Image processing , and (d) Reconstruction of bed shape*

Separate calibration images are captured from each camera to account for the differences in position and the lenses themselves. These calibration images are processed, and the pixel coordinates are extracted for each know grid point on the gauge block along the path of each laser point. The known physical dimension (mm) is plotted against the corresponding extracted vertical pixel co-ordinate, shown in Figure 3.9c. The calibration equation is obtained by applying a linear fit to the extracted calibration data. The calibration equations are used to convert the extracted dimensions obtained from the recorded images to physically correlated vertical dimensions estimated using the calibration procedure.

The calibration plots for each laser point located across the curved test section (L1 = 47.5 mm, L2 32.5 mm, L3 17.5 mm, L4 2.5 mm) are shown in Figure 3.9c. The red dashed line being the linear calibration equation fitted to the calibration data. The calibration equations shown in figure 3.10d represent Calibration set 3 for camera 4.

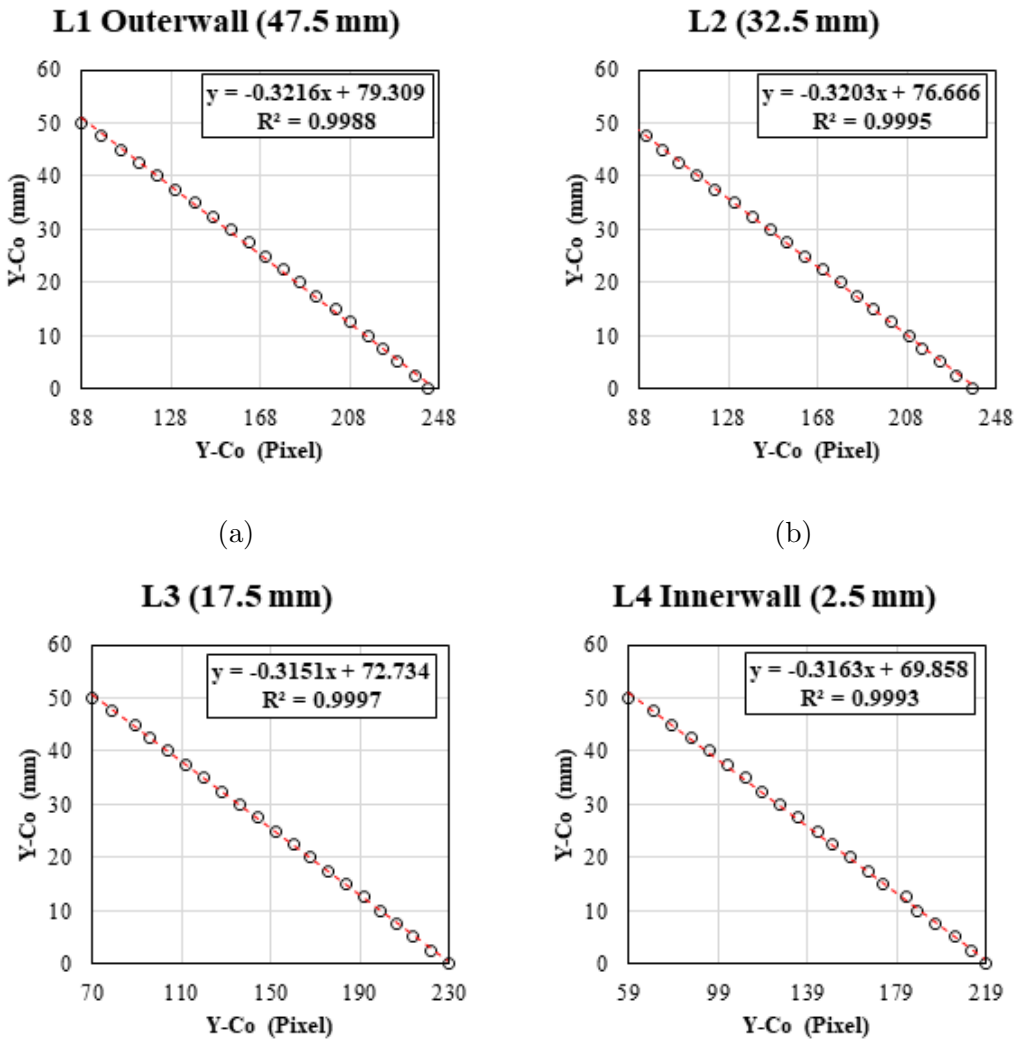

Figure 3.10: *Calibration equations for camera 4*

Calibration error is determined by the difference between the know physical reference point (gauge block) and the solution provided by the calibration equations. The calibration errors for all calibrations used for the results presented and their associated experiments are shown in Table A.4 and A.5

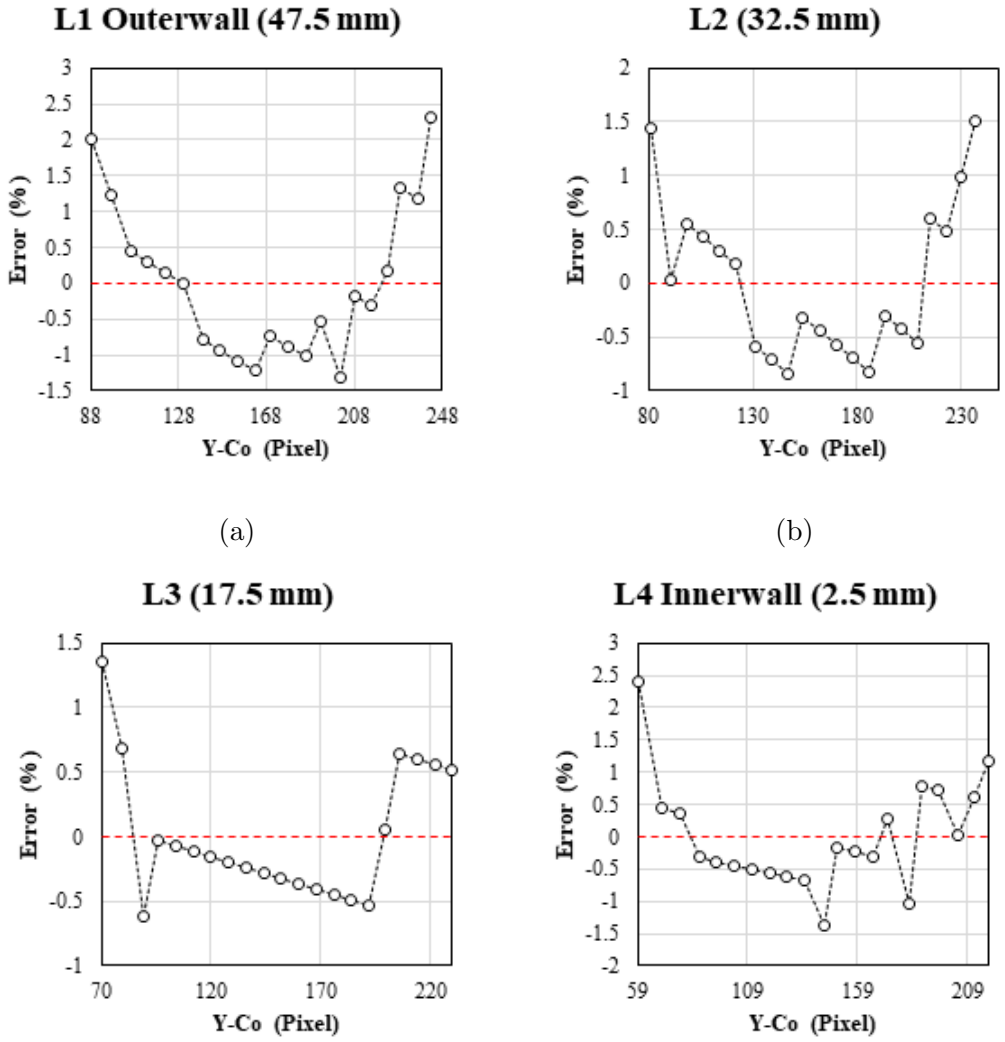

Figure 3.11: *Relative error associated with calibration along the vertical plane for each laser*

3.6 Image processing

Image processing forms an integral part in the extraction of experimental data. Video recording is segmented to the required temporal resolution which produces images for each time step during the experiment. The extracted images are cropped using MATLAB's inbuilt function to produce a consistent image showing only the area of investigation; note that the cropping area is determined during the calibration process. The cropping area position is vital as the calibration reference frame and the experimental area of integration must be the same. Pre-processing of images greatly expedites image processing and dramatically improves the accuracy of results owing to the removal of external light sources such reflections.

Two different techniques are evaluated for data extraction, a fully automated technique and a semi-automated technique. The fully automated technique makes use of colour filtering, this was achieved using the luminesce value of the image to isolate the points where the highest luminance occurred; seen as the brightest points on the image. Converting the image to a binary image, with the isolated laser points set to a value of 1 and all other parts of the image to 0. Image colour filtering allows for the extraction of the centroidal coordinated of each isolated laser point, with the Y-coordinates as in the case of the calibration gauge, to be substituted into the respective calibration equation for the respective point. The automated nature of this process brings inherent time efficiency but introduces additional uncertainty in the extracted results owing to periodic adverse measurement condition during experimentation.

The semi-automated process consisted of automatic image post-processing. The main difference is that it does not make use of colour filtering and conversion to a binary image. Data extraction is achieved by manually selecting the centre the identified laser points. The selection of the next image to be processed and the storage of the extracted data is automated, with only the identification of the centre of these points being manual. This process is more reliable owing to the dynamic nature of the granular bed, as data can be investigated even under adverse conditions. Laser points which are unidentifiable using colour filtering in the fully automated process can be extracted using the semi-automated process, providing improved temporal and spatial resolution. Furthermore, measurement accuracy is increased when using the semi-automated process.

3.7 Measurement Accuracy

The purpose of this section is to provide a detailed description of measurement accuracy for the results presented. Calculation and quantification of accuracy for both the measured granular bed height and the recorded flow rates are presented. Determination of measurement accuracy associated with the non-intrusive measurement techniques is discussed. Sources of uncertainty are determined, and the contribution to the total measurement uncertainty is outlined. Three sources of uncertainty are evaluated, Gauge Block Uncertainty (U_G), Calibration Uncertainty (U_c) and Laser Point Uncertainty (U_{LP}) and the final total uncertainty (U_T) determined.

3.7.1 Gauge Block Uncertainties

Uncertainties arising from the use of the gauge block are a direct result of the reference grid. The grid, a 2.5 mm $\times$ 2.5 mm square mesh contains lines of 0.35 mm thickness; the line thickness directly contributes to uncertainty as any measurement taken within the line have an uncertainty equal to the line thickness. The uncertainty associated with the Gauge Block (U_G) is of a magnitude of $\pm(0.2)$ mm or $\pm(0.4)$ % uncertainty, holding to the convention of taking uncertainty to the first significant digit.

3.7.1.1 Calibration Uncertainty

Calibration Uncertainty results directly from curve fitting of the calibration equation, a determination of uncertainty associated with calibration are of importance owing to the conversion of experimental results from the digital space (pixels) to the physical space (mm) using these equations. In order to report this uncertainty accurately, an appropriate method for uncertainty calculation must be used.

The original source of error is determined using the difference between the known gauge block dimensions and those calculated using the calibration equation, as shown in Figure 3.10a, 3.10b, 3.10c, and 3.10d in Section 3.5.1. The data used for determining the calibration uncertainty consist of 21 points this corresponds to 2.5mm increments from 50mm to 0 mm along the face of the gauge block. Calibration uncertainty is evaluated using the Student's t method, providing a

confidence interval of 95%. Student's t method is employed due to the small sample size of calibration points along the laser path. Using Equation (3.1) with calibration uncertainty (U_c), Student's number (t), standard deviation (σ) and sample size (n).

The value of t was determined by referring to the Student's t table, based on the data size of n = 21, v = n-1, therefore using the value for v = 20, t = 2.083 is then used. Standard deviation is then subsequently calculated for each calibration equation and the calibration uncertainty determined using Equation (3.1).

$$U_c = \frac{t\sigma}{\sqrt{n}} \tag{3.1}$$

3.7.2 Laser Point Accuracy

Laser Point Uncertainty is determined using the size of the laser points projected onto the granular bed. The source of uncertainty arises from the size of the projected laser point, which is directly affected by factors such as, the angle of the granular bed profile, light scatter during rapid erosion events, and the diffusive nature of the granular bed.

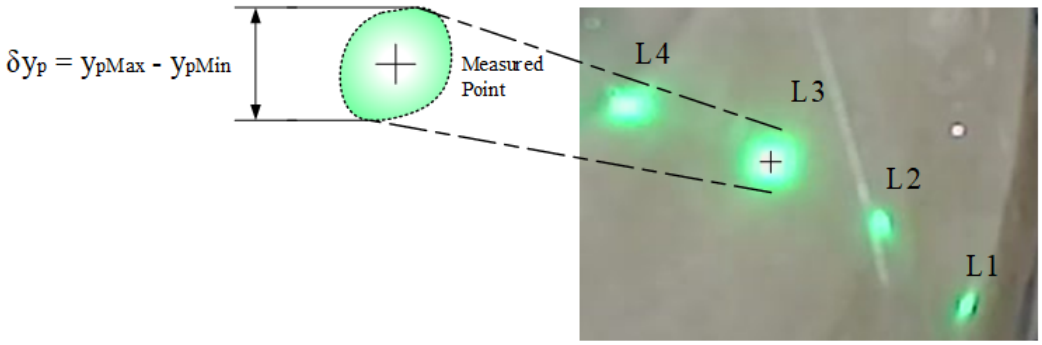

Figure 3.12: *Illustration of laser point uncertainty*

Laser Point Uncertainty is determined by taking the difference in the maximum and minimum vertical extent of the laser point (δ_{yp} = y_{pMax} - y_{pMin}), this is used in preference over the laser point diameter as the majority of projected circumferential edges of the projected laser point are not equidistant from there centre. Furthermore, the discrepancy between the centre of illumination (marked as a cross in Figure 3.12) and the centroid of the projected laser point

in most cases do not correspond; this can be seen above for laser point (L4). Making use of the maximum vertical extent of the projected laser point provides a consistent determination of Laser Point Uncertainty. Figure 3.12 shows various laser points taken from experimental data and the extraction of the projected Y-co uncertainty range. This process is repeated for every laser point at all time steps.

The relative uncertainty for each laser point, the final Laser Point Uncertainty (U_{LP}) is taken as two standard deviations ($2\sigma_{LP}$) about the mean, shown as the red dashed lines in Figures 3.13, 3.14, 3.15 and 3.16 corresponding to a 95% confidence interval, with the standard deviation determined using Equation (3.2) and relative uncertainty using Equation (3.3).

$$\sigma_{LP} = \sqrt{\frac{(\delta y_1 - \mu)^2 + (\delta y_2 - \mu)^2 \ldots + (\delta y_n - \mu)^2}{n-1}} \tag{3.2}$$

With variables Laser Point Uncertainty (U_{LP}), laser point standard deviation (σ_{LP}), the relative difference (δy_n) and the mean of the relative laser point difference (μ).

$$U_{LP} = \mu \ \pm 2\sigma_{LP} \tag{3.3}$$

Figures 3.13 and 3.14, with Figures 3.15 and 3.16, uncertainty increases towards the inner-wall (L3 and L4). This increase in uncertainty is due to the dynamic nature of interaction at these locations, undergoing periods of concentrated erosion and sedimentation events, resulting increased light scatter and a greater variation in the projected laser point dimensions.

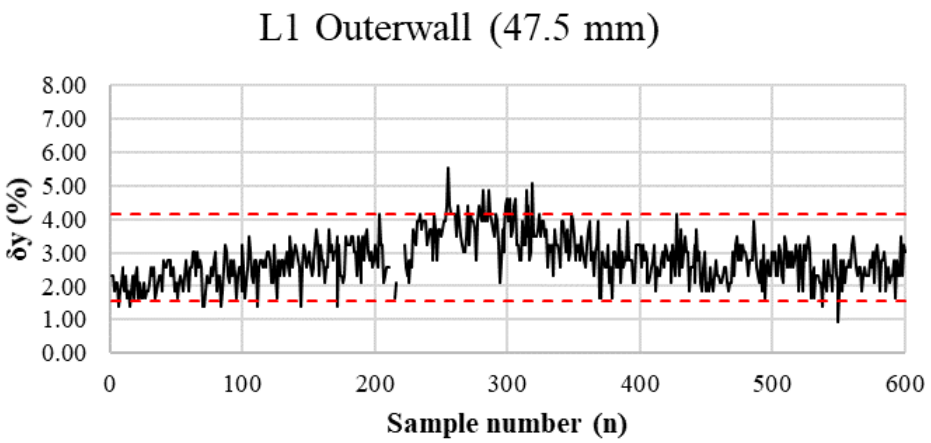

Figure 3.13: *Laser point uncertainty for Laser 1 (Point 1 outer-wall), EXP-135-300-57-02.*

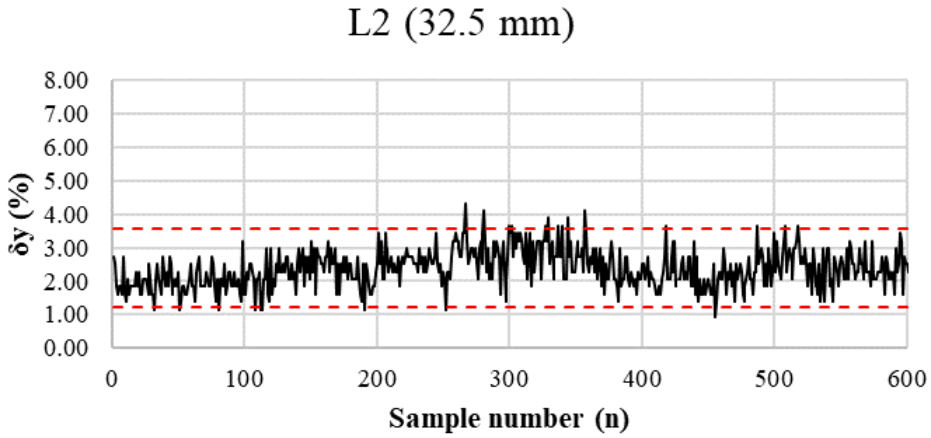

Figure 3.14: *Laser point uncertainty for Laser 2 (Point 2), EXP-135-300-57-02.*

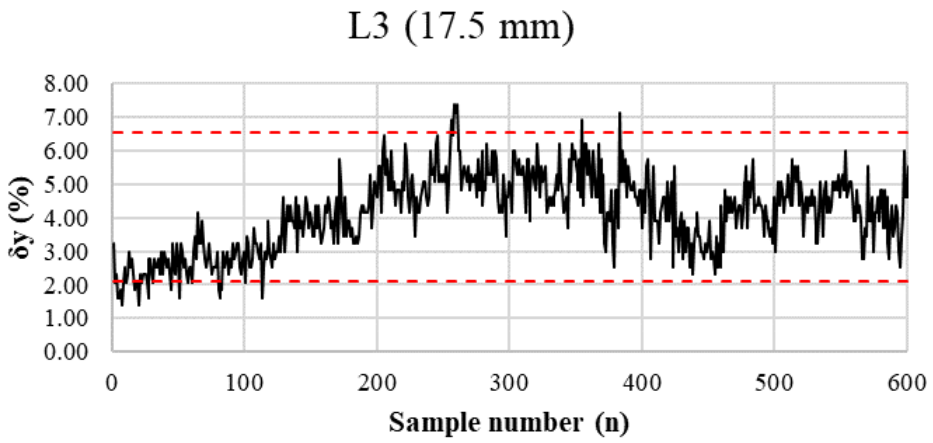

Figure 3.15: *Laser point uncertainty for Laser 3 (Point 3), EXP-135-300-57-02.*

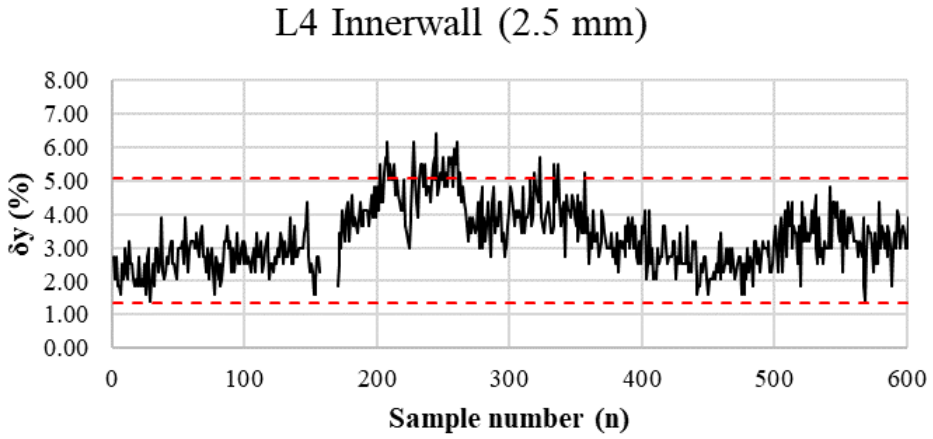

Figure 3.16: *Laser point uncertainty for Laser 4 (Point 4 inner-wall), EXP-135-300-57-02.*

3.7.3 Experimental Accuracy

Total experimental accuracy is determined by Equation 3.4 this accounts for the propagation of uncertainty throughout the measuring process for each experiment. Table A.1, A.2 and A.3 in Appendix A, show Experimental Uncertainty for experiments results taken at the 135° position along the curved test section.

$$U_T = \sqrt{U_C^2 + U_{LP}^2 + U_G^2} \tag{3.4}$$

3.7.4 Flow Measurement Uncertainty

Flow uncertainty is comprised of two sources, instrument measurement accuracy provided by the manufacturer and uncertainties resulting as a consequence of fluctuating pressure drop across the curved test passage. This pressure drop is due to the changes in the granular bed profile and the resulting changes in Aspect Ratio and surface friction. Subtle adjustments in pump speed are made to account for pressure drop and maintain the flow at the desired rate; uncertainty relating from these adjustments to flow rate are evaluated.

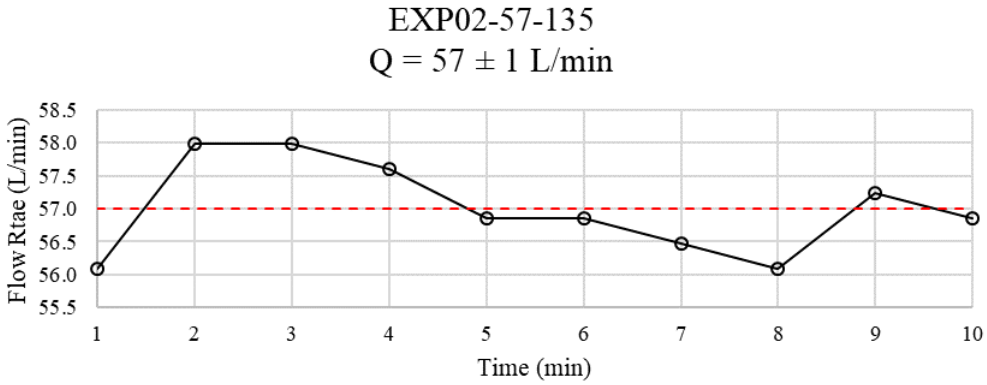

Figure 3.17: *Collected flow rate measurement during experimentation.*

Flow rate uncertainty as a result of pump speed adjustment is determined by taking a reading every minute during the experiment. Uncertainty due to flow rate fluctuation (U_F) and the required flow rate adjustments are determined by taking two standard deviations of the recorded flow rates for the for each experiment providing a confidence interval of 95% for reported flow rates.

Using Equation (3.5) the propagation of uncertainty is determined by taking flow rate fluctuation uncertainty (U_F) with equipment uncertainty ($U_E = \pm 1\%$ of recorded flow rate).

$$U_Q = \sqrt{U_E^2 + U_F^2} \tag{3.5}$$

3.8 Summary of Experimental Method and Considerations

Conditions for inducing fluid-granular interaction are possible due to the carefully selected geometric parameters of Aspect ratio (1.5) and Curvature Ratio (5) for the curved test section. Clean sediment free inlet fluid supply is ensured, with a high degree of flow rate selection and control resolution made possible by way of a VSD. A simple and reliable non-intrusive measuring technique using four discrete laser points in combination with a calibration gauge block and four cameras mounted around the interaction region of interest, with measurement accuracy reported and discussed. The methods discussed in this chapter allow for both a qualitative and quantitative investigation of the interactions between the granular bed and secondary flow structures.

Chapter 4

Qualitative Observations

The monitoring and processing elements explained in the Methods Chapter are deployed for qualitative observation and quantitative measurements. A combined approach is used to account for the complex and coupled nature of fluid-granular interactions and the stochastic nature of the granular phase. A qualitative description of the Fluid-granular interaction in the curved fluid passage is provided to contribute to an informed investigation plan for further measurements and quantitative analysis.

Qualitative and quantitative identification of discrete stages of interaction are described and illustrated. These stages of interaction are the intial stage, characterized by the formation of bedform features, the transient stage with dynamic and cyclical changes in granular bed height, and finally the quasi-stable stage with a stable granular bed profile. Furthermore, observations of key identifying bedform features, such as inner-wall dunes, and upstream ridge formation, both named after their location of inception, are illustrated and discussed. Effects of perturbation on experimental results is also briefly discussed and illustrated to provide examples of experimental sensitivity.

Based on observations informed by qualitative analysis, quantitative measurement of bed height is applied across the curved fluid passage at fixed radial locations as Fluid-granular interactions progress. A spatial investigation at four radial locations across the curved fluid passage provides details of fluid-granular interactions in the streamwise direction. Additionally, temporal analysis using a fixed single frame (radial position of 135°) measurement provides a Eulerian description of the phenomenon, this is used for temporal scaling of the process according to key parameters such as flow rate and granular phase characteristics.

Nevertheless, the full observation of the process over time and throughout the test section reveals those measurements cannot solely be referred for comprehensive projection of vortices and bed evolution during the term of the experiment. Therefore, the process is qualitatively explained based on general observation of process taking place across the channel as time progresses.

4.1 Qualitative description of the process

A qualitative description of the Fluid-granular interaction in the curved fluid passage is provided to define and highlight parameters of interest. The identification of discrete stages (initiation stage, transient stage and quasi-stable stage) of interaction are described and illustrated, with identifying bedform features illustrated and explained. The effects of surface perturbation and the effects of Fluid-granular interactions are briefly discussed.

4.1.1 Inner-wall dunes formation - initiation stage

The initial product of interactions between the fluid and the granular phases was seen as the formation of bed structures here referred to as inner-wall dunes, relating them to their location of inception; the initiation of which occurred over the radial span from 80° to 180°. inner-wall dunes formed due to the displacement of surface grains from the outer-wall. The outer-wall being where the Secondary flow initially has higher intensity (i.e. with a flat bed) and carried out toward the inner-wall, the removal of surface grains from the outer-wall was dispersed over a relatively broad surface area so as to leave no measurable initial change at the outer-wall. The accumulation of displaced granules nonetheless resulted in the formation of small bed defects from which inner-wall dune formed. The presence of helix-like flow structures associated with the curved duct contributed to the inner-wall nature of these dunes. The higher secondary flow intensity at the outer-wall prevented the accumulation of granules and stable outer-wall granular bed. Contrasting this, interaction at the inner-wall where flow deceleration due to interaction with the inner-wall occurred, and the resulting division of fluid momentum into axial and vertical components, would be insufficient to lift and carry away the granules with the bulk flow and therefore a gradual build-up and migration of the formed dunes occur.

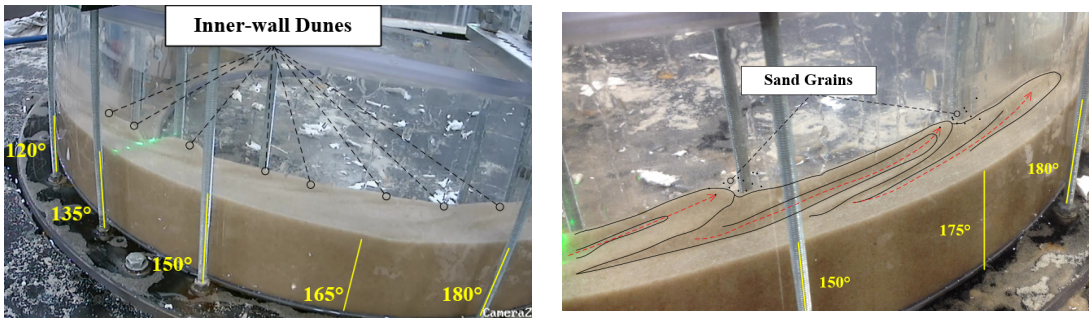

(a) (b)

Figure 4.1: *(a) Initial stages of Fluid-granular interaction seen as inner-wall dunes, (b) Propagation of inner-wall Dunes due to scour.*

As the dune height from the original granular bed surface increased, the flow structure of fluid, shape and local intensity secondary/Dean eddies would, in turn, be influenced. The product of these interactions seen as regions of scour along the granular bed extending in the direction of flow inclined towards the inner-wall (Figure 4.1a). The propagation of inner-wall dunes shown in Figure 4.1b illustrates the first inner-wall dune seeding another younger dune downstream of the parent dunes location. The accumulation of grains displaced due to scouring, shown by the path of the dashed red arrows, increased the size of the seeding dune. As the seeding dune reach occupied a sufficient width of the curved duct, scour occurred around the seeding dunes parameter (Figure 1.b).

Granular material was displaced the scour path and accumulated to form a new inner-wall dune. Continued scour along the path of the newly formed inner-wall dune gradually enlarged it, and assisted in the formation of another downstream inner-wall dune repeating the process anew. Additionally, the scour path pushed the crest of the inner-wall dunes along the duct wall, resulting in dunes migrating streamwise. The effects of increased flowrate (57 - 63 L/min) were seen by the simultaneous initiation of multiple inner-wall dunes and their rapid propagation along the inner-wall, in contrast at lower flowrates (47 - 53 L/min) an initial inner-wall dune formed from which subsequent dunes were seeded.

During the formation of inner-wall dunes flow reattachment due flow separation caused by the seeding dune was not observed. As discussed the prime observable agent of inner-wall dune propagation was seen as scour paths along the granular surface. The presence of localised scour suggests the dominance of secondary flow instability due to interaction with the curved duct outer-wall, in contrast to flow separation as seen in dune formation in axial flows.

4.1.2 Evolution of dunes - transient stage

Following the initiation stage of formation, dunes gradually expanded width wise across the curved duct and concurrently were pushed along in the streamwise direction. This widening provided a more extensive base of flow for scour resulting in the region of scour moving closer to the outer-wall. The movement of scour to the outer-wall marked a transition from the initial inner-wall sedimentation dominant stage to new interactive behaviour of combined erosion/sedimentation across the entire width of the duct. The transient nature of interactions was a result of the migration of outer-wall erosion in the streamwise direction. During this stage the most prominent interaction between the fluid and granular phase occurred, showing strong oscillatory behaviour (i.e. the bed height is intermittently varying across the channel).

Momentum transfer between the fluid and granular phase during outer-wall erosion was sufficient to entrain the granular material removed from the outer-wall and be transported by the fluid phase without being redeposited back onto the bed as seen in Figure 4.2.

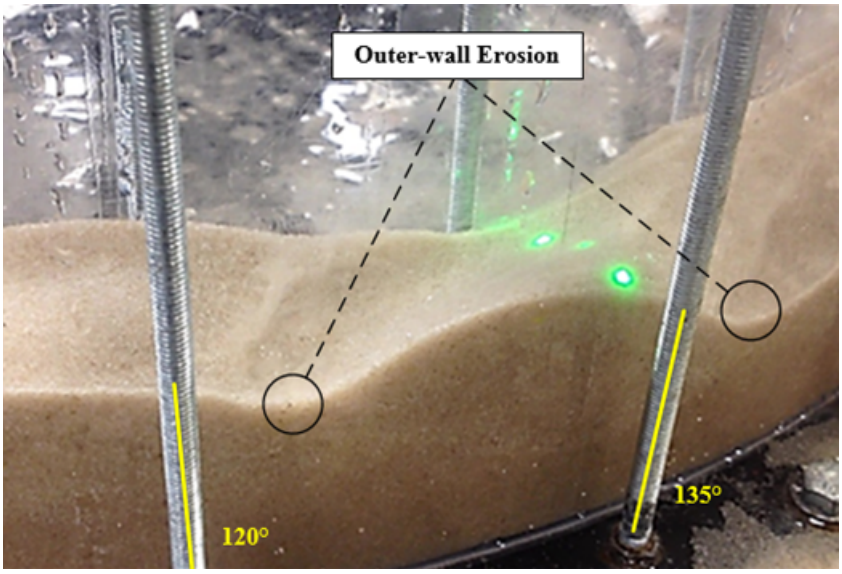

Figure 4.2: *outer-wall erosion and granular bed particle entrainment.*

The captured cyclic behaviour originated as the combined effect of the migration of scour region interacting with the outer-wall and the resulting the widthwise expansion of the migrating dunes to occupy the entire width of the curved duct. Continued erosion along the outer-wall seen as localised increased Fluid-granular interactions gradually resulted in the deepening of the outer-wall scour. The change in granular bed profile mutually affected the secondary flow structures responsible for the bed morphology. The mutually coupled nature of this interaction leads to an attenuation in the oscillatory behaviour of the granular bed, gradually trending towards a less volatile stage of interaction.

4.1.3 Interaction stabilisation - Quasi-stable stage

The third stage of interaction defined by the stabilisation of granular bed was seen as the cessation of dynamic changes in granular bed height across the curved duct, with the established bed morphology persisting and slow and gradual erosion continuing so that the absolute bed height decreased almost evenly across the curved duct. This stage is referred as quasi-stable erosion sedimentation stage, owing to the relative stability of fluid-granular interactions.

During the quasi-stable stage, a general deepening of the original scour regions which defined the transient stage occurred. The rate of erosion in this region was seen to reduce gradually, and as such, the granular bed was seen to stabilise. The decrease in the erosion rate and the quasi-stable nature of interaction may be attributed to mutual interaction between bed and helical structure converging into a stable configuration. Additionally, the granular bed profile is maintained by the presence of these vortices; grains seen rolling down the inclined slope of the granular bed, would in turn be lifted back up by the fluid, this interaction occurred consistently throughout the quasi-stable stages.

Observation of the granular bed along the radial extent of the curved duct showed the most predictable and constant interactions occurred at the radial position of 135°. With the final quasi-stable stage occurring at this location with a constant granular bed profile; downstream radial positions varied with respect bed profile but maintained quasi-stable behaviour. The granular bed profile observed at the radial position of 135°, commonly seen at this stage, had the lowest bed height toward the outer-wall with increasing height to towards the inner-wall.

4.1.4 Upstream ridge

The formation of ridge upstream of the main interaction regions (80° to 180°) occurred at the location (30° to 80°). This ridge referred to as an upstream ridge was formed gradually throughout experiments and is categorised by scour along the inner-wall of the ridge (Figure 4.3). Fluid-granular interaction along the outer-wall was dominated by gradual inward erosion in the direction of the inner-wall, the confluence of the rapid motion of fluid at the inner-wall and the inward dominant motion of the outer-wall resulted in the accumulation of granular material along a ridgeline.

The formation of this ridge was formed by the rolling of individual grains along the bed surface from the outer-wall towards the inner-wall, the direction of which is shown by the dashed red arrows in Figure 4.3. The inner-wall side of the ridge was dominated by rolling of individual grains in the direction axial flow, denoted by the black arrow in Figure 4.3.

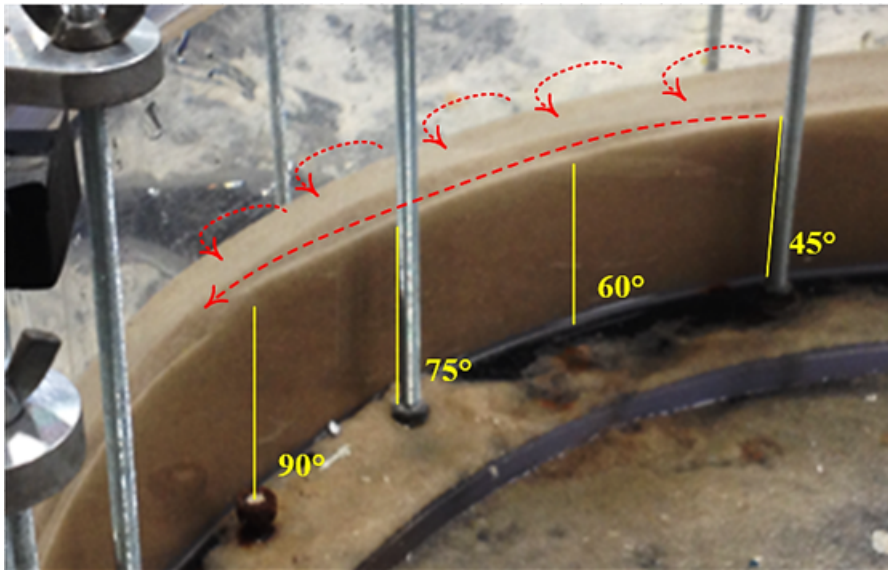

Figure 4.3: *Inner-wall ridge formation and development.*

With increased flowrates (50-63 L/min), the upstream inner-wall ridge is seen to grow due to increased sedimentation along the ridgeline and increased erosion at the outer-wall. At a flow rate of 63 L/min, the granular profile associated with the upstream ridge is translated from its location to the outlet of the curved duct, 180° radial position. This transfer of the upstream ridge along the remainder of the curved duct is also seen when the granular bed grain size is increased to 475–1180 μm with the ridge formed at lower flowrates relative to granular bed size ranges of 150–300 μm and 300–400 μm.

4.1.5 Further Qualitative observation

The sections above described the various stages of interaction; granular bed features providing a general definitional reference for the qualitative observations presented. In order to provide an expanded the disruption of the interaction mentioned previously, a complete qualitative overview is provided. This overview serves to contextualise the earlier description with the broader interactions occurring in the curved duct.

Interactions along the curved fluid passage were seen to dominate along the outlet half (90°-180°) of the curved duct. The specific nature of interactions and the categorisation of three phases, namely initial, traditional and quasi-stable are all observed in this section of the curved fluid passage. A broader overview of the transition between these phases is discussed to provide a qualitative

representation of the complex Fluid-granular interaction at this region. Images showing the evolution of the granular bed, and the influence of secondary flow structures over three discrete stages are shown from both inner-wall and outer-wall perspectives.

As discussed previously, initial interactions are seen as inner-wall dunes with a stable outer-wall region (Figures 4.4a and 4.4b). As the process of initial interaction intensifies the size and number of inner-wall dunes increases, with the base of these dunes expanding outwards towards the outer-wall (Figures 4.4c and 4.4d).The result of these initial interactions as seen from the inner-wall is the accumulation of granular material due to the presence of inner-wall dunes. Additionally, from both the inner and outer-wall perspective the deepening of scour along the perimeter of the inner-wall dunes can be seen (Figures 4.4c and 4.4d)

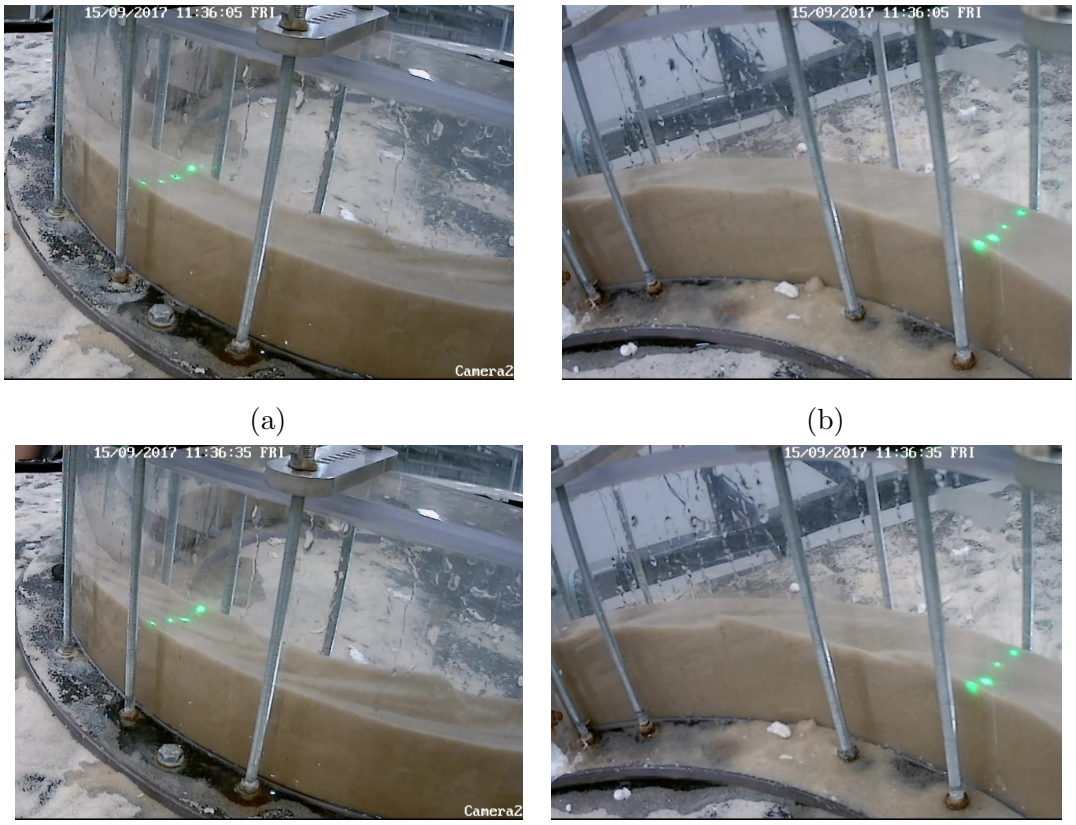

Figure 4.4: *Initial development and formation of inner-wall dunes, outer-wall (a) and (c), inner-wall (b) and (d).*

The migration and growth of inner-wall dunes continued in Figure 4.5a and Figure 4.5b, with deepening in the scour produced by secondary flow structures.

Moreover, the region of scour progressed to the outer-wall marking the start of the transient stage of Fluid-granular interactions. Observations of the commencement of the transitional stage showed the start of oscillatory behaviour of the granular bed at the outer-wall Figure 4.5c and Figure 4.5d. inner-wall interactions were relatively unchanged, showing sedimentation and migrating inner-wall dunes as the dominant interactions.

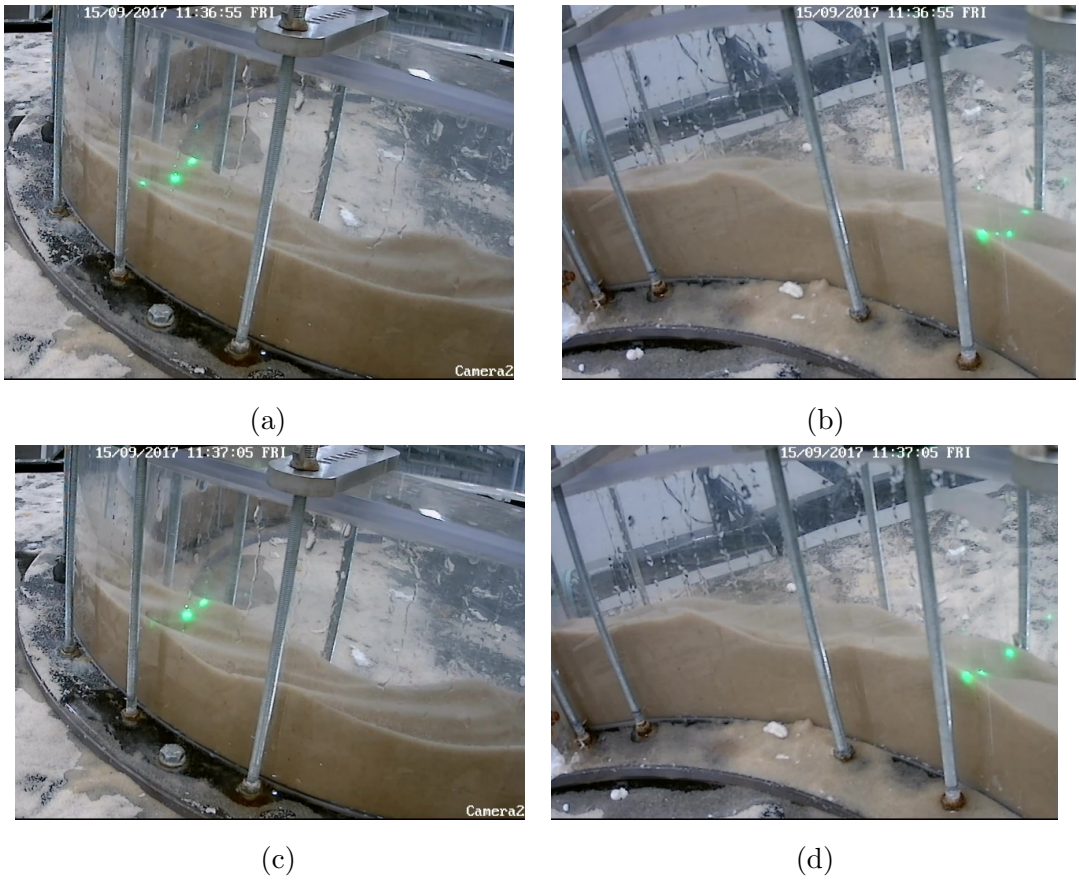

(a) (b)

(c) (d)

Figure 4.5: *Extension and of scour towards the outer-wall, outer-wall (a) and (c), inner-wall (b) and (d).*

The establishment of the transitional stage and the oscillatory nature of outer-wall interaction are seen in Figure 4.6a and 4.6b, with the imprint of secondary flow structures on the granular bed seen as prominent scouring and intensified erosion along these regions. When comparing Figures 4.6c and 4.6d, an increase in the amplitude of the outer-wall oscillatory bed profile was observed, with negligible change in granular bed profile at the inner-wall, when a comparison is made between Figure 4.6b and 4.6d.

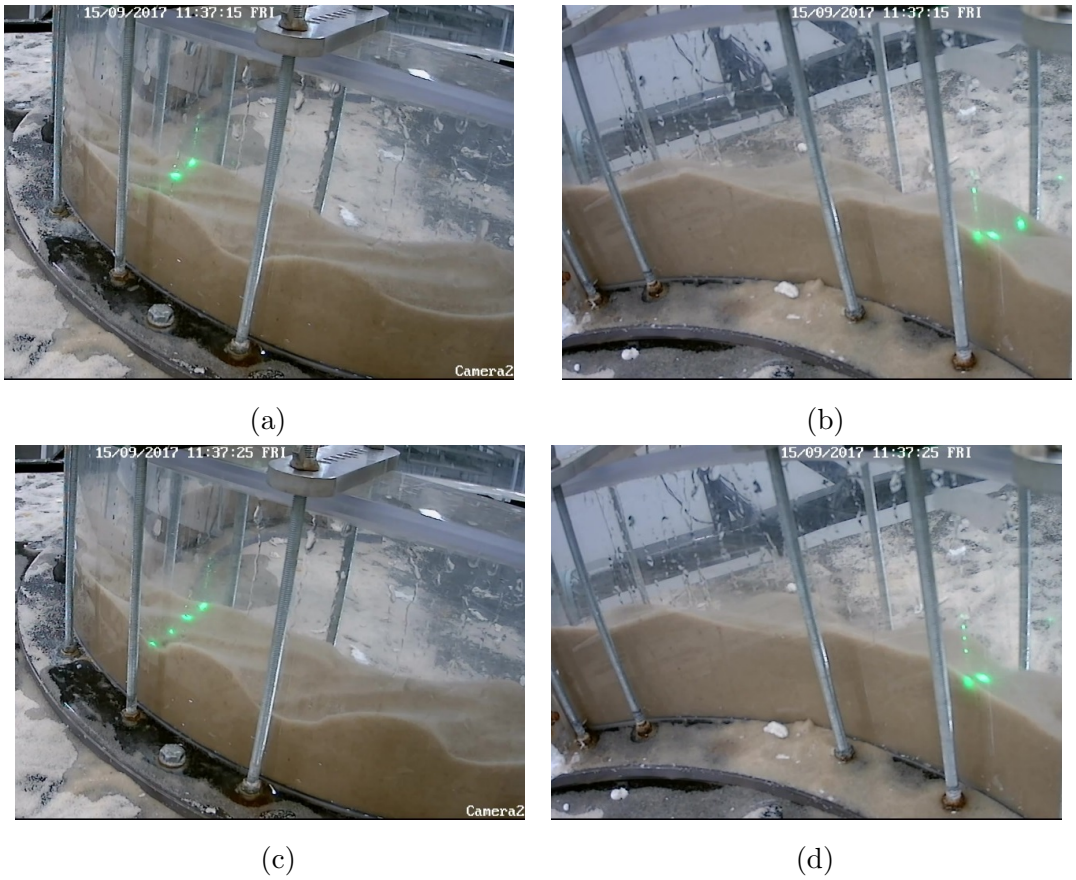

Figure 4.6: *Dynamic and oscillatory interactions during transitional stage, outer-wall (a) and (c), inner-wall (b) and (d).*

The lateral expansion of scour towards the outer-wall marking the progression to the transitional stage can be seen in Figures 4.7a and 4.7b. The oscillatory nature of outer-wall interaction was captured, coupled with a gradual lateral expansion of scour. The change from inner-wall dune and sedimentation dominant interactions at the inner-wall, to oscillatory interaction with dominated by erosion across the width of the curved fluid passage can be seen in Figures 4.7c and 4.7d.

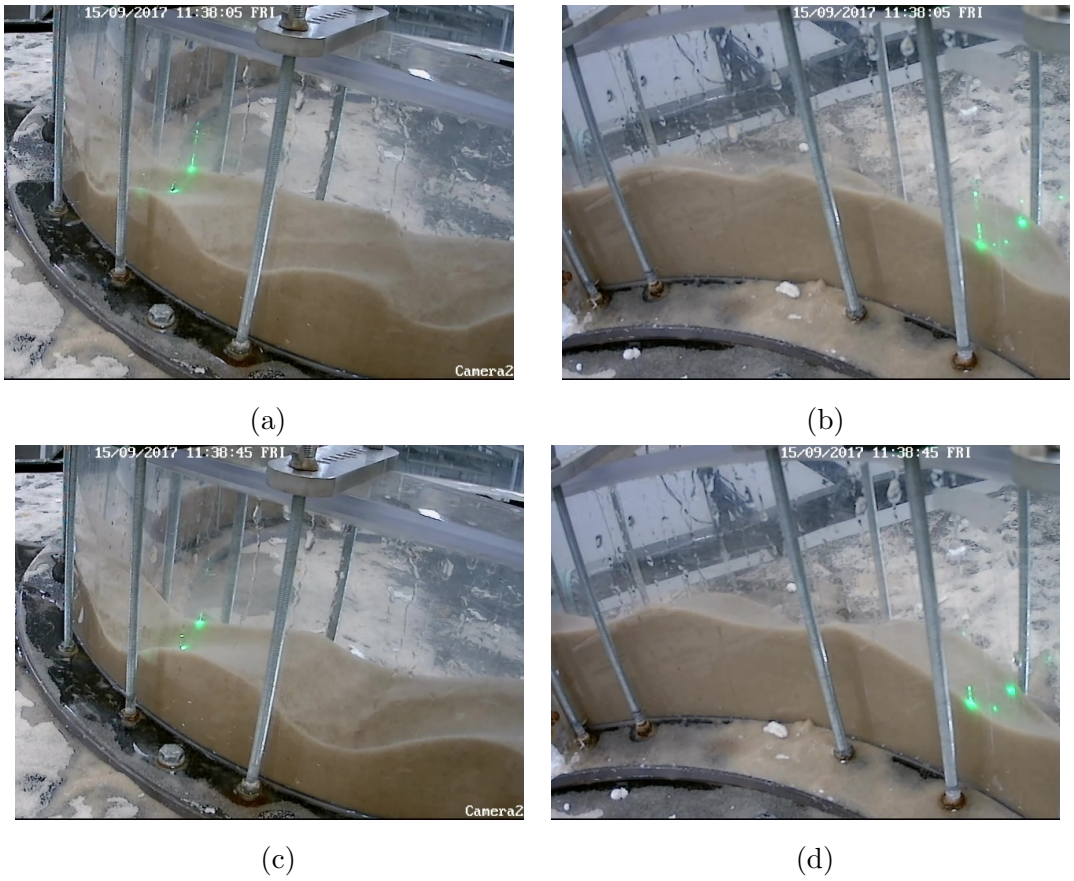

Figure 4.7: *Decay of transient behaviour, outer-wall (a) and (c), inner-wall (b) and (d).*

The expansion of scour regions due to secondary flow structures gradually intensified, creating a granular bedform that no longer showed the dynamic interaction observed previously, seen in Figures 4.8a and 4.8b. Reduced dynamic interaction marked the transition to the quasi-stable stage of Fluid-granular interactions. The characteristic granular bedform during the quasi-stable stage was defined by larger dunes, relatively stable bedform morphology at both the inner and outer-wall. The radial position of 135° was observed to be a reliable location of bedform quasi-stable interaction; this can be seen in Figures 4.8c and 4.8d.

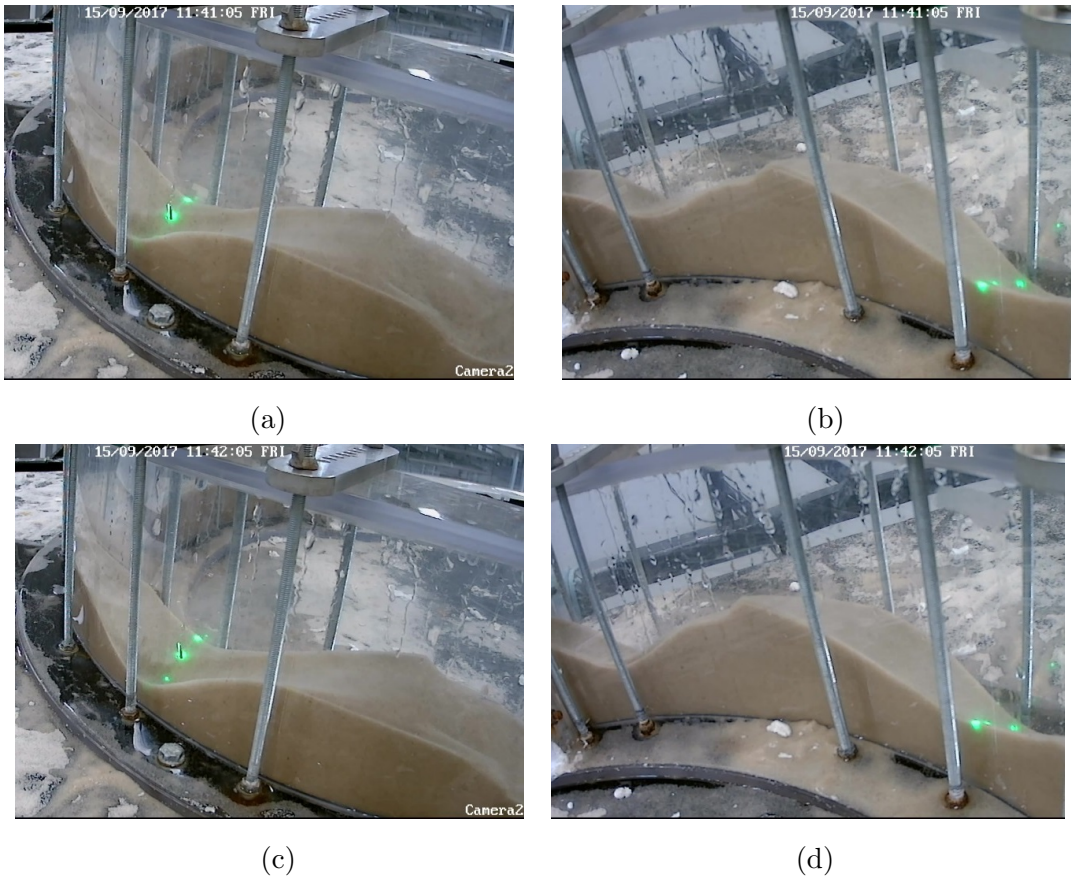

Figure 4.8: *Stabilisation of granular bed, outer-wall (a) and (c), inner-wall (b) and (d).*

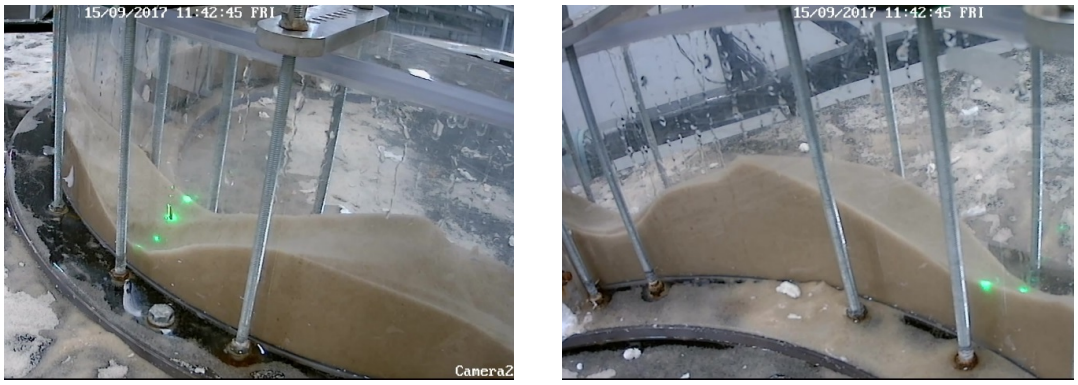

(a) (b)

Figure 4.9: *Quasi-stable granular bed profile, outer-wall (a) and inner-wall (b).*

The initiation of interaction between secondary flow structures and the granular bed was seen to be dominate at the outlet side of the curved fluid passage. The initiation stage defined by the formation of migrating inner-wall dunes and their gradual radial expedition towards the outer-wall showed evidence of scour induced by the interaction of secondary flow cells.

The extension of granular bed scour to the outer-wall marked the transition stage, seen as dynamic Fluid-granular interactions. The complex coupled nature of secondary flow instability and granular bed morphology was seen as an increase in the oscillatory nature of granular bed outer-wall interaction, and the eventual transition of the inner-wall to oscillatory interactions. The value of qualitative observations is shown when identifying points of interest, such as the radial position of 135°, this position showed predictable fluid-granular interaction and granular bed morphology, with the final bed form having the highest bed height at the inner-wall with a downward incline to outer-wall.

As the flow rate is increased, the radial position of initiation is moved upstream when compared to that of lower flow rates, the result of which is an increased transient stage as the upstream initiation position must first reach a quasi-stable state in order for the downstream granular bed to stabilise.

Fluid-granular interaction was dominant in the outlet half of the curved fluid passage (90°-180°). In contrast at the inlet half (0° 90°) interactions comprised of inner-wall ridge formation from 30° to 80° and no visible interactions from 0° 30°, this is illustrated in Figure 4.10. The red hatched area marks the region of no interaction, the orange hatched area the region where the inner-wall ridge formation occurred, and the green hatched area marked the dominate region of interaction.

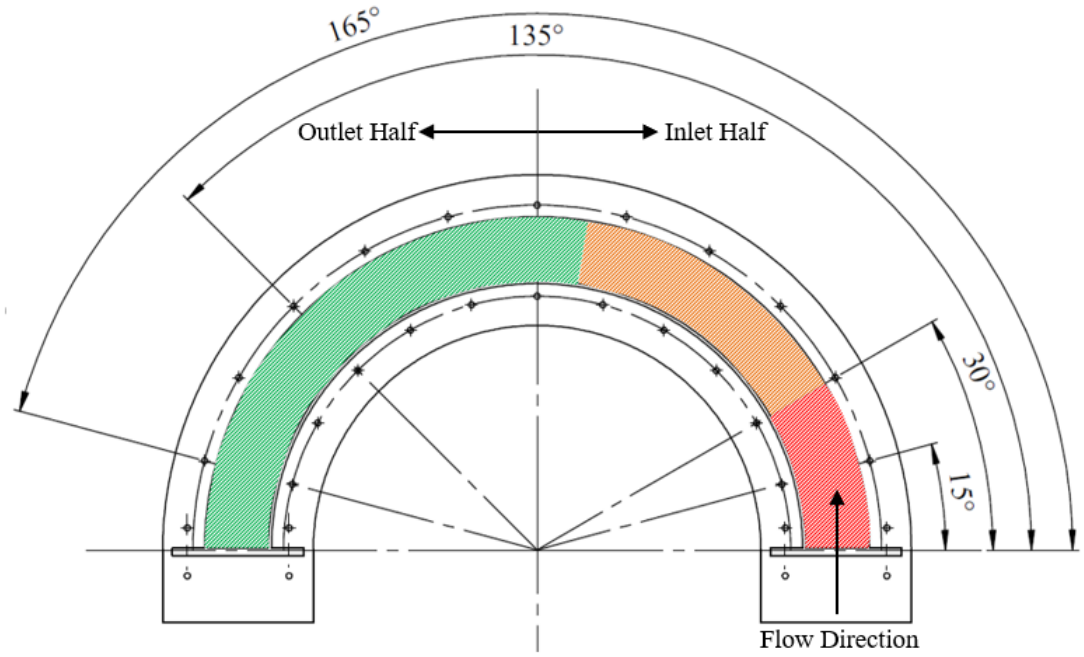

Figure 4.10: *Region of no visible interactions (Red), region of inner-wall ridge formation (Amber), and region where all three stages of fluid-granular interactions occur (Green).*

4.1.6 Effects of perturbation

The interaction between the secondary flow field and the granular bed are stochastic in nature, requiring repeated experimentation to capture meaningful results. The sensitivity of fluid-granular interactions to external disturbances such as granular bed surface perturbations, is seen as the delayed or premature erosion. Moreover, an increase interaction intensity at higher flow rates, and granular bed forms inconsistent with those observed are the result. A description and illustrations of these inconsistencies is provided, and the implication concerning the data presented discussed.

Surface perturbation as used in this context is described as random morphological imperfections on the granular bed surface, arising from the bed preparation process. What is not included in this definition is the surface roughness due to the grain size inherent to the granular bed, as this is an inherent property of the granular bed and cannot be treated as anomalous.

Surface perturbation seen as surface defects, shown in Figure 4.11, resulted in increased unpredictable behaviour of the granular bed. Unpredictable behaviour, seen as delayed or early onset of interactions with respect to other experiments of the same parameters. Formation of granular bedforms inconsistent with those observed for the majority of results presented. In addition, when sources of perturbation occurred near the inlet of the curved fluid passage (0° to 45°) the entire granular bed would undergo dynamic and oscillatory interaction.

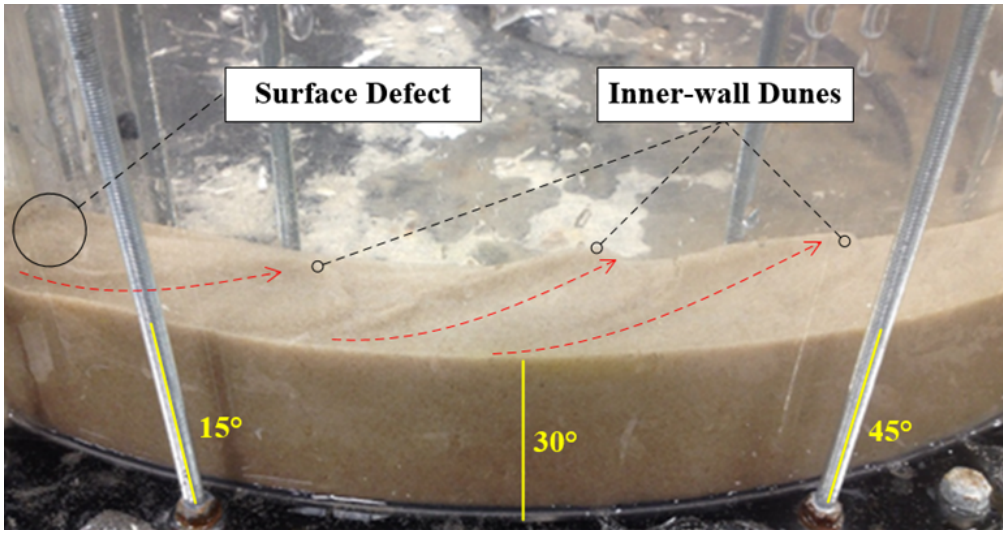

Figure 4.11: *Effects of surface perturbation.*

The precursor to the dynamic and oscillatory interactions described was seen as inner-wall dunes, as described previously, undergoing the same formation process with the only difference being the radial locality (forming at the surface defect location). The inner-wall dunes formed due to protrusions or granular material that had accumulated on the surface of the granular bed, creating a surface defect significant enough to begin the process of inner-wall dune formation.

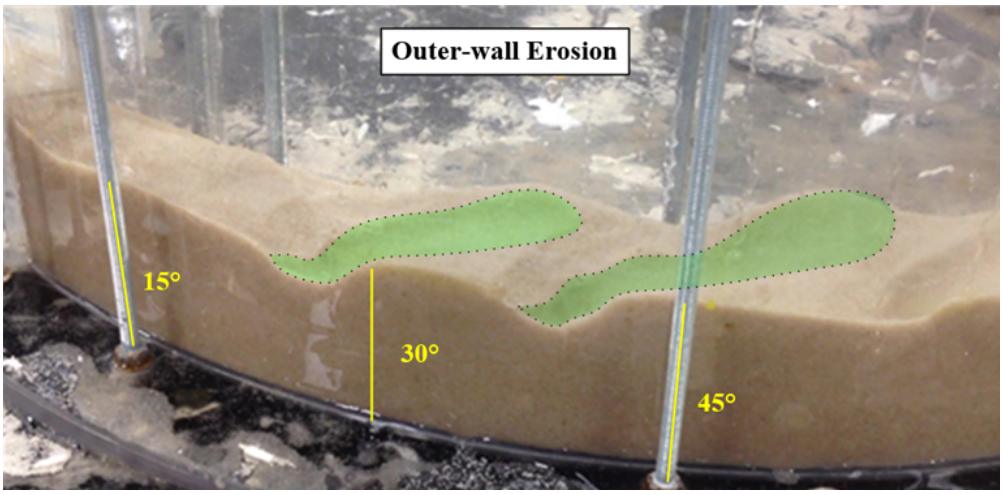

Figure 4.12: *Premature lateral scour due to surface perturbation.*

Interactions at the outlet side of the curved passage still underwent the processes described previously, but as the inlet, half of the curved fluid passage transitioned from inner-wall predominant bedform to a dynamic and oscillatory bed form as a result of the transition to outer-wall erosion shown in Figure 4.12. The interaction upstream of this region were then affected as the dunes formed downstream rapidly moved upstream occupying the entire granular bed across the curved fluid passage. At lower flowrates the presence of surface perturbation lead a delay in Fluid-granular interactions. The result of which was a stable bedform or one which showed little change over time.

The observed effect of surface perturbation though not the aim of this work still underpins a vital aspect the results presented. That a relatively small change in surface morphology can set in motion significant changes in Fluid-granular interactions with both flow field structures and the granular bedform being affected as a result of these changes.

4.2 Summary of Qualitative Observations

Qualitative observation provided the identification of discrete stages of Fluid-granular interactions, the initial stage, transient stage and quasi-stable stage. At the initial stage (Stage.1), the presences of bedforms such as inner-wall dunes and inner-wall ridges provided clues to the behaviour of fluid structures present in the curved fluid passage interactions with the granular phase. The formation of inner-wall dunes, location and motion along the channel point to the influence of helix-like flow structure in a curved fluid passage.

The transient stage (Stage.2), seen as a direct result of the outward widening of scour around the parameter of inner-wall dunes and eventual contact with the outer-wall (Figure 4.6a) was defined by prominent Fluid-granular interactions. The transient nature of interactions seen as dynamic and complex granular bed profiles captured in Figures 4.7a and Figures 4.7c, show increased intensity of Fluid-granular interactions to be attributed to helix-like structures in the curved fluid passage, with the footprint of these structures seen in the scour paths produced on the granular phase.

The dynamic and oscillatory reshaping of the granular bed during the transient stage subsided marking the final stage of interactions, the quasi-stable stage (Stage.3). A defining characteristic of this stage is the stable granular bed profile seen in Figure 4.8a and Figure 4.8c. Moreover, the majority of the cases captured show the granular bed profile during the quasi-stable stage dominated by outer-wall erosion, with increased bed height towards the inner-wall. outer-wall dominated erosion could be associated with the local intensity of secondary vortices, which are expected to be higher at the outer-wall. The stabilisation of a previously dynamic granular bed, suggests that mutual interaction between bed and local vortex shape have converged providing the stable bed form.

A valuable contribution of the qualitative observations presented is the identification of the radial position of 135° as providing reliable and repeatable Fluid-granular interactions for temporal investigation. Additionally, a general description of interactions along the entire curved fluid passage is provided, with Fluid-granular interactions dominant along the outlet halve of the curved passage (90°-180°), with the inlet half (0°-90°) interactions comprised of inner-wall ridge formation from 30° to 80° and no visible interactions from 0°-30°.

Qualitative observations provided additional insight into the sensitivity of Fluid-granular interactions to surface perturbations, which resulted in the unpredictable initiation of erosion/sedimentation along the curved fluid passage. Small surface defects at the curved fluid passage inlet propagated the premature formation of inner-wall dunes, initiating the three stages of interaction mentioned above at locations that remained relatively unchanged for the majority of experiments undertaken.

Chapter 5

Quantitative Experimental Results and Discussion

The quantitative results presented in this section are separated into a Lagrangian and Eulerian overview. The Lagrangian approach provides a spatial perspective for Fluid-granular interaction along the curved duct; represented by four cross-sections. Spatial information obtained is then used for the identification of regions of interest for further investigation using a Eulerian approach. Quantitative results using a Eulerian approach are represented at a fixed cross-section providing detailed temporal information. The final overview presented for quantitative results is seen as a sensitivity analysis by varying the mean grain diameter of the granular bed.

5.1 Spatial investigation: A Lagrangian overview across the channel

The monitoring positions and time steps, presented in the Figures 5.1 to 5.10, consisted of a granular bed with an average grain size range of 300 – 400 μm with interactions captured for flow rates 47, 50, 53, 57 and 60 L/min. Locations of Spatial investigation were 15°, 60°, 135° and 165° for all results presented in this section. The positioning of investigation locations is based on qualitative observations presented in Section 4.1 and positioned symmetrically about the 90° radial position to best illustrate interactions of secondary flow structure with the granular bed across the curved fluid passage. The figures depict the process of bed reshaping as a result of mutual interaction between the bed interface and spiral structure of secondary flow. Column 1–4 from left to right for all figures presented in this section, show position 15°, 60°, 135° and 165° respectively. The starting flow rate of 47 L/min was selected based on qualitative observations, which determined the minimum flow rate required for reliable Fluid-granular interactions to occur.

5.1.1 Flow rate 47 L/min

For a flow rate of 47 L/min, the first indication of initial interactions (Figure 5.1) occurred at t = 440 sec, with the collection of granular bed material resulting in the formation of an inner-wall ridge at 60°. Continued development of interaction continued at t = 600 sec, seen as sedimentation at the inner-wall (Point 4) for both positions 135° and 165°, this sedimentation is a result of the presence of inner-wall dunes as described and illustrated in Section 4.1.1, with the continued development occurring at 165° for time step t = 750 sec.

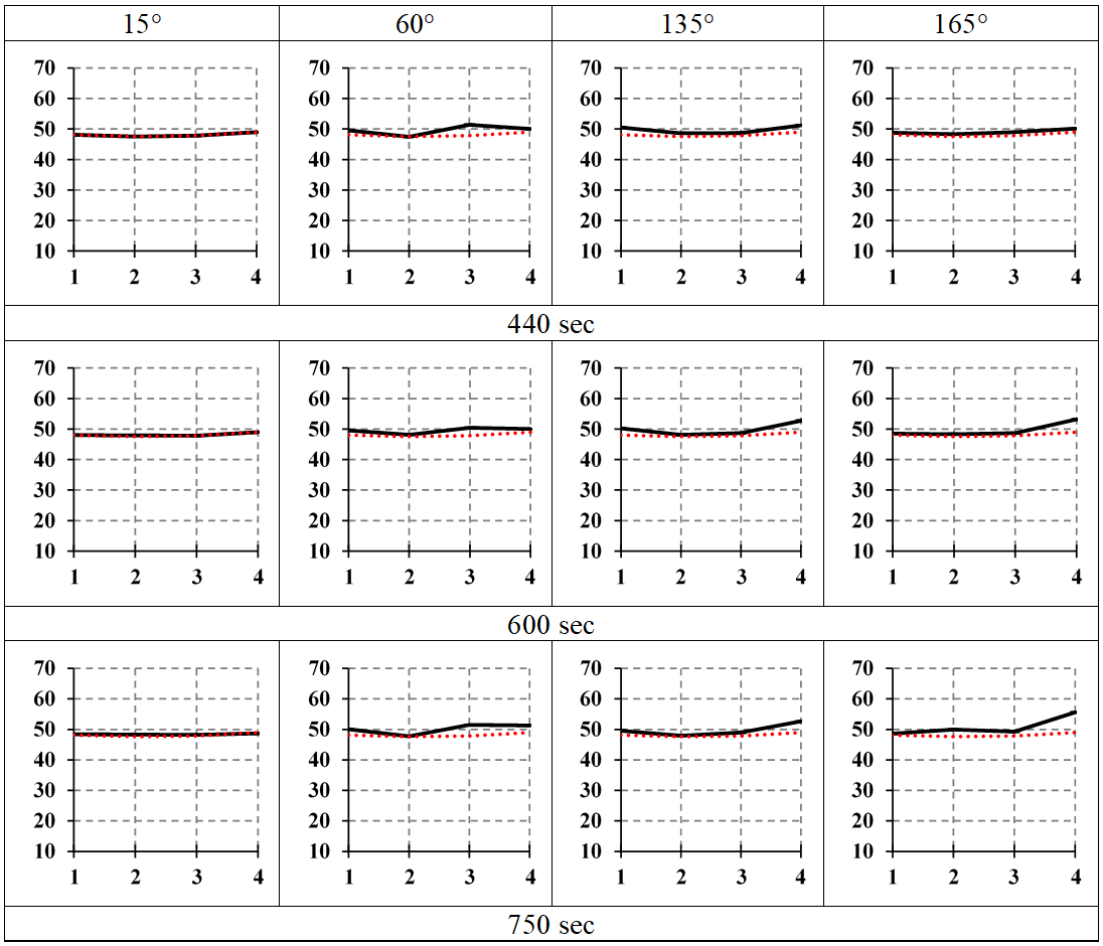

Figure 5.1: *Spatial evolution of bed profile @ 47 L/min. Y-axis shows bed height in mm, 1-4 on the X-axis indicates points arranged from the outer to inner-wall.*

The gradual expansion of inner-wall sedimentation is seen for position 165°, with the expansion of sedimentation at Point 4 and Point 2 across the curved fluid passage for time steps t = 920 sec. Position 135° is seen to be stable with the presence of the inner-wall dune maintained during this time step.

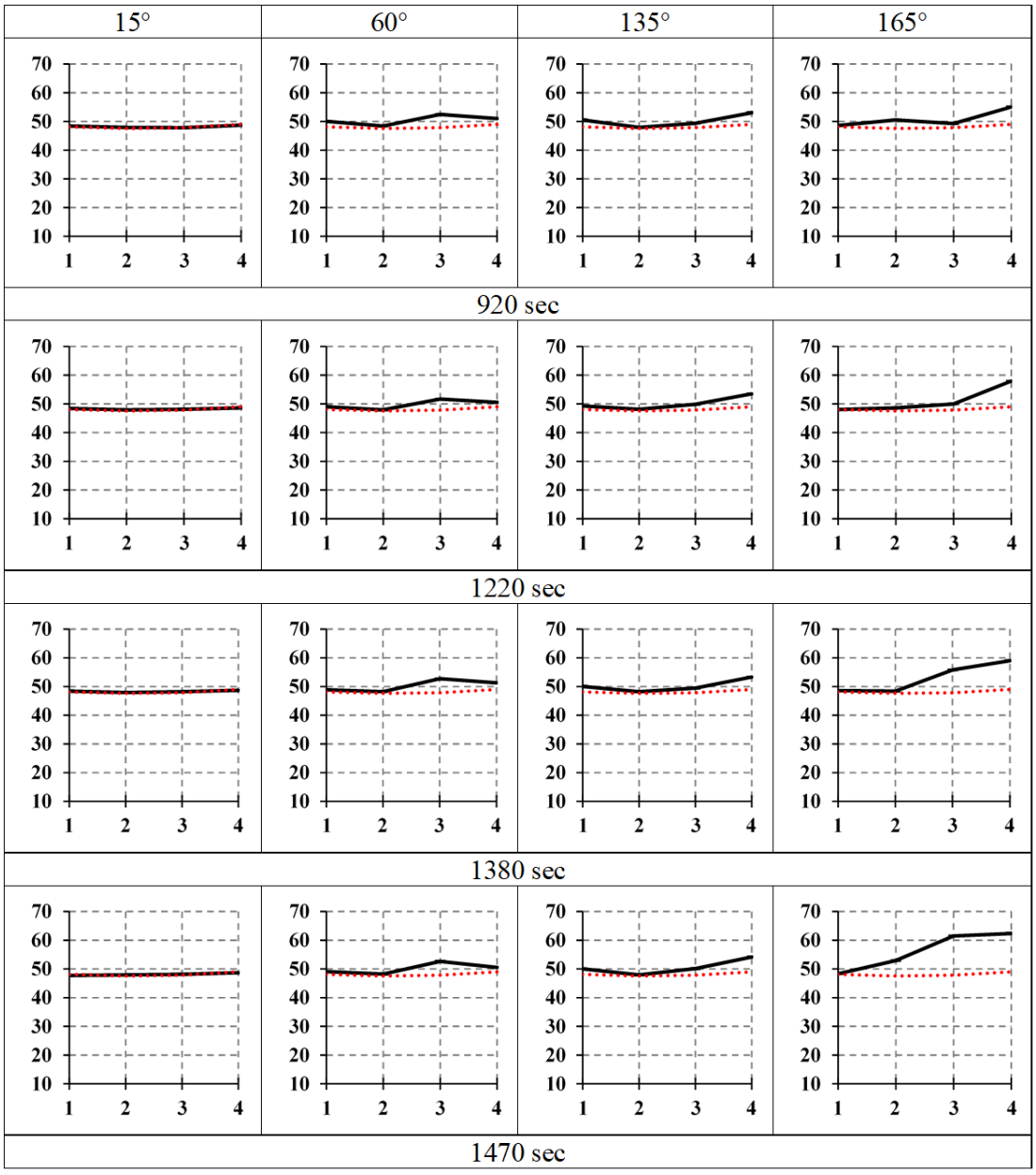

Figure 5.2: *Spatial evolution of bed profile @ 47 L/min. Y-axis shows bed height in mm, 1-4 on the X-axis indicates points arranged from the outer to inner-wall.*

Increased inner-wall sedimentation is seen at 165° and 135° at t = 1220 sec with position 165° showing the passing of an inner-wall dune. The transient inner-wall dune at t = 1380 sec is seen as increased granular bed height for Point 3 at 165°. The bed profile at 135° during this same time step was seen as stable. With

respect to the 15° position, no measurable change in bed height was captured for all time steps. Interactions at 60° show a stable inner-wall ridge from t = 920 sec to t = 1470 sec with the bed profile remaining unchanged over this period. The final time step of t = 1470 sec, saw the continued passing of an inner-wall dune at 165°, seen as an increase in bed height occurring at Points 2, 3 and 4 across the cross-section. For position 135°, the continued occupation of an inner-wall dune at the same time step with the slow and gradual migration of this dune, when comparison of each cross-section over time is made.

5.1.2 Flow rate 50 L/min

Initial interactions were seen within t = 130 sec, shown in Figure 5.3, with the presence of inner-wall dunes at the 135° and 165° positions, occurring within a shorter period when compared to a flow rate of 47 L/min. A notable transition occurs at t = 300 sec, with the intuition of outer-wall erosion at both 135° and 165°. Moreover, this marks beginning the transient stage of Fluid-granular interactions, and the oscillatory behaviour observed during this stage.

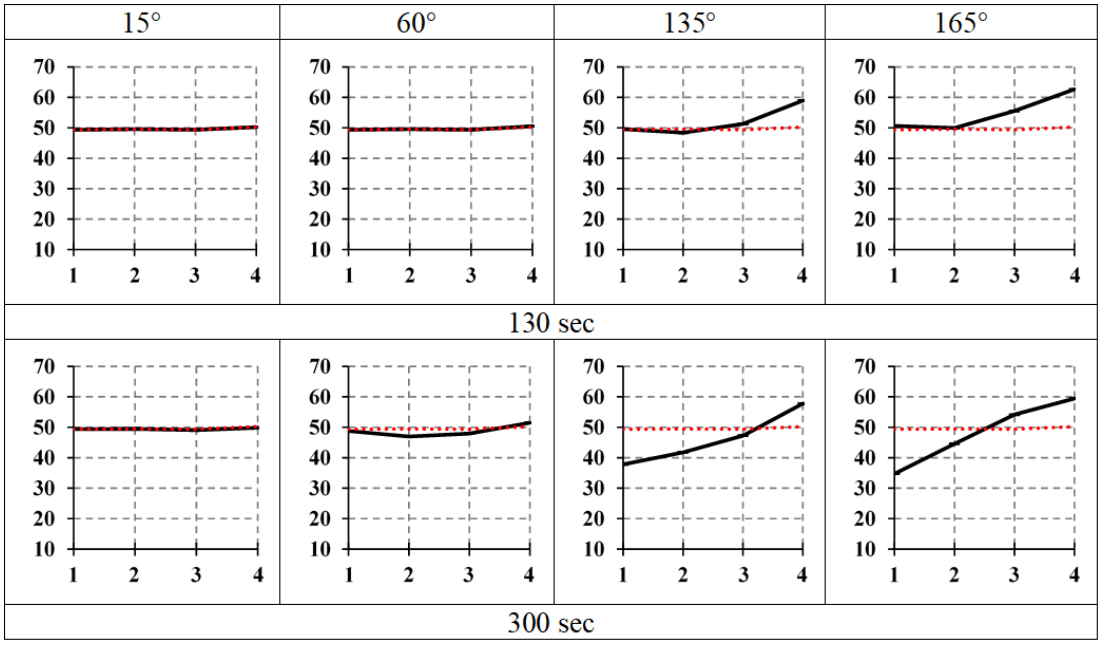

Figure 5.3: *Spatial evolution of bed profile @ 50 L/min. Y-axis shows bed height in mm, 1-4 on the X-axis indicates points arranged from the outer to inner-wall.*

The oscillatory nature of interaction is seen at t = 490 sec with the 135° position showing sedimentation at the outer-wall and a general increase in height for all points across the bed. The oscillatory interaction described is a result of the Fluid-granular interaction described in Figure 4.7a and Figure 4.7c, Section 4.1, where the imprint of local secondary flow structures on the granular bed is captured.

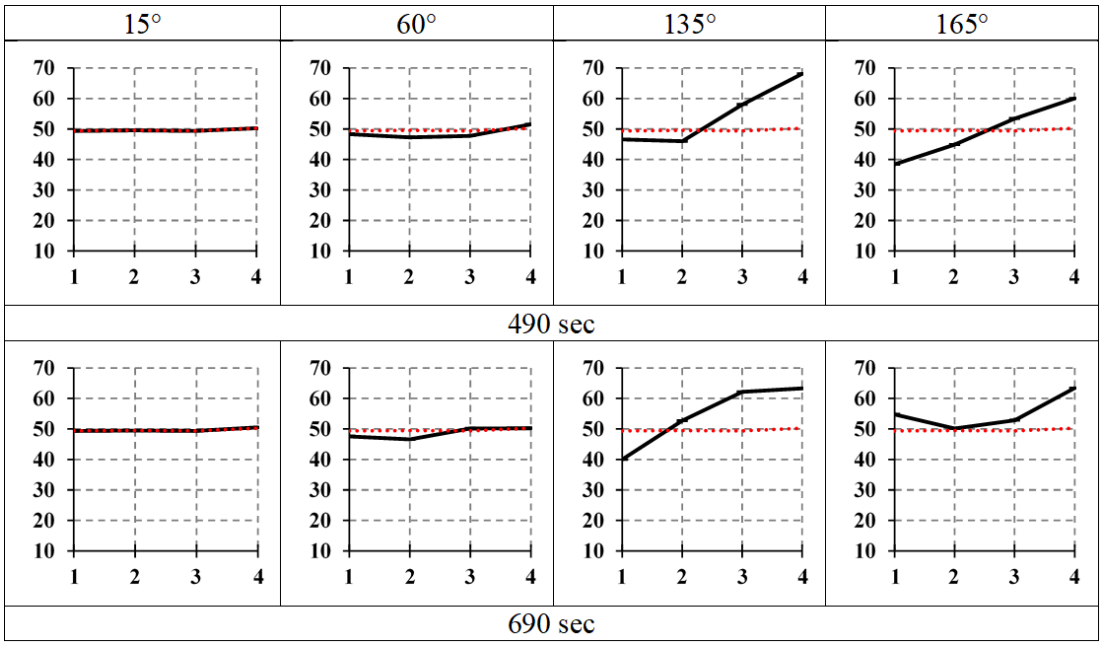

Figure 5.4: *Spatial evolution of bed profile @ 50 L/min. Y-axis shows bed height in mm, 1-4 on the X-axis indicates points arranged from the outer to inner-wall.*

Oscillatory interactions continued for time step t = 690 sec at 135° and 165°. With resulting interactions at 135° seen transitioning once more to the outer-wall (Point 1) erosion. In contrast position 165° transitioned to outer-wall sedimentation, this transition is a result of the migration of the bed form seen in Figure 3.6 and Figure 3.7 along the curved fluid passage in the direction of flow, this is seen when comparing Points 3 and 4 with the previous time step where there is no change in the respective bed heights. Position 60° showed gradual localised erosion at Point 2, however did not develop the same inner-wall ridge as seen previously. The gradual and consistent erosion at Point 2 suggests the influence of secondary flow effects on interaction at this position along the curved fluid passage. Consistent with observation made at 47 L/min the 15° position is seen to be stable for all time steps presented.

5.1.3 Flow rate 53 L/min

With an increase in flow rate to 53 L/min, the formation of inner-wall dune at t = 130 sec for both 135° and 165° was captured seen as a localised increase in bed height at point 4 for both cross-sections. The migration of an inner-wall dune is seen at t = 300 sec for position 135°, with the granular bed returning the original bed height; marked by the red dashed line. In contrast, the 165° position showed a transition to oscillatory behaviour described previously, with a concentration of erosion across Points 1 and 2.

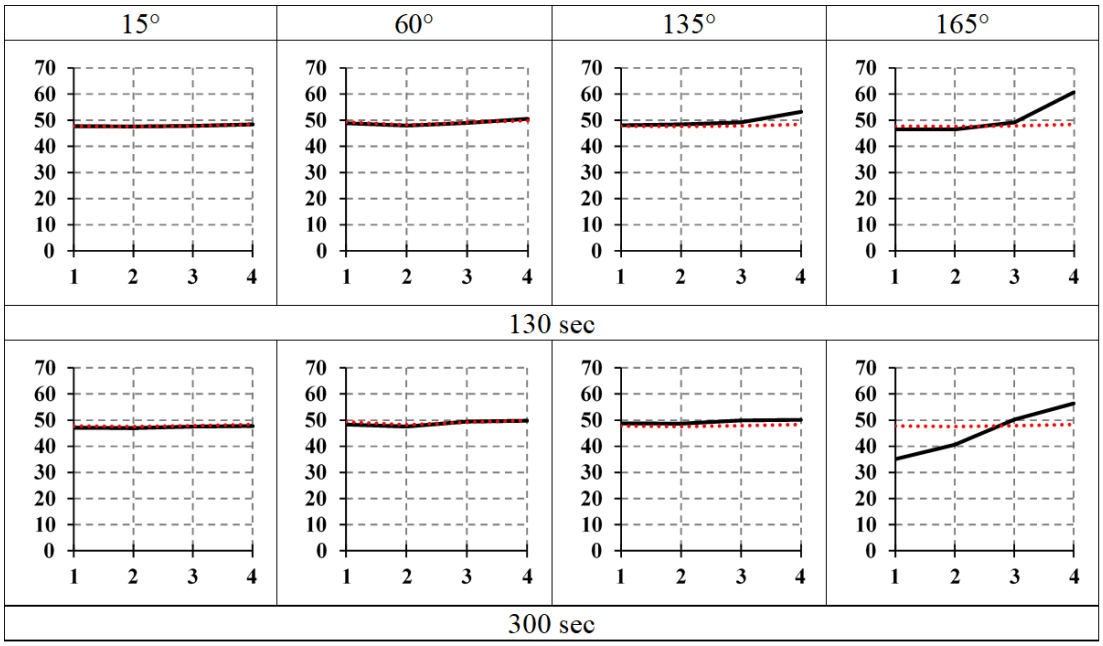

Figure 5.5: *Spatial evolution of bed profile @ 53 L/min. Y-axis shows bed height in mm, 1-4 on the X-axis indicates points arranged from the outer to inner-wall.*

At the t = 490 sec, interaction at 135° and 165° transition to that of inner-wall dominate erosion, at both positions the change in bed profile is dramatic with changes in inclination and bed height occurring. The transition to inner-wall erosion is a result of Fluid-granular interaction upstream of the 135° position, leading to the creation of a localised regions of erosion and the deposition of granular material downstream at the 165° position along Points 1(outer-wall), 2 and 3.

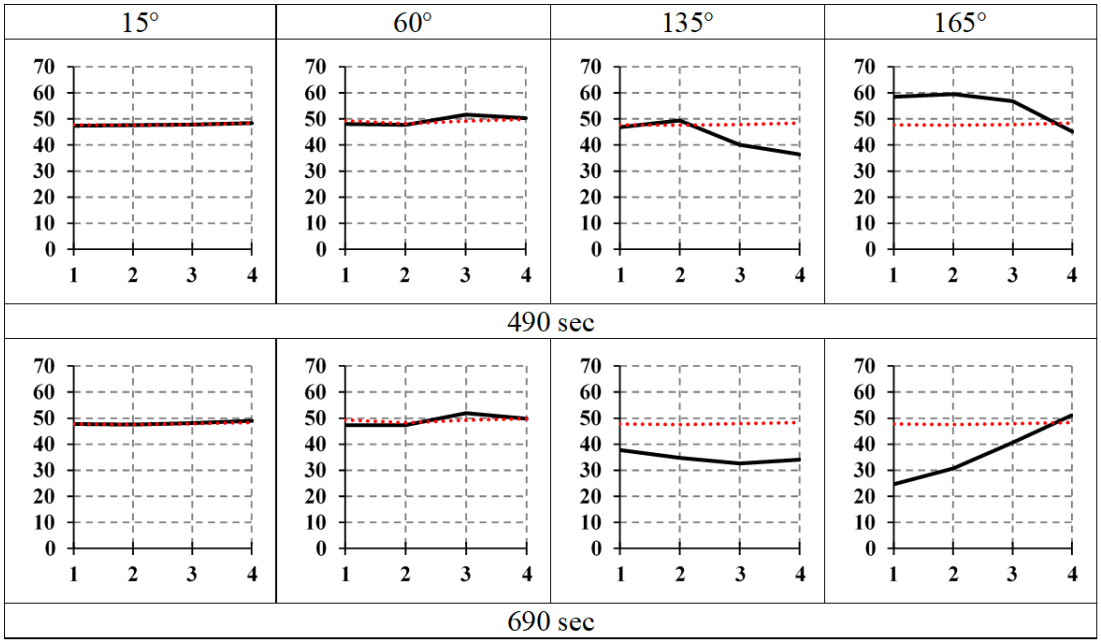

Figure 5.6: *Spatial evolution of bed profile @ 53 L/min, Y-axis shows bed height in mm, 1-4 on the X-axis indicates points arranged from the outer to inner-wall.*

For the final time step t = 690 sec position 165° showed a dramatic transition from the previous time step, with significant erosion occurring across the outer-wall. Position 135° showed gradual and sustained erosion across all points; this bed profile is associated with the trough of a passing dune in the traditional stage seen in Figure 4.7d. The absence of interactions is repeated for the 15° position. The development of an inner-wall ridge is seen to have developed at 60°, with the localised erosion at Points 1 and 2 and a clear ridge formation at Point 3 at t = 690 sec.

5.1.4 Flow rate 57 L/min

At a flow rate of 57 L/min, when compared to previous flow rates, establishment of dynamic bed interaction occurs earlier at t = 210 sec. The presence of complex Fluid-granular interaction seen for bed profile at 135°, with the scour due to the inner-wall dune formation and the development of outer-wall interaction seen in Figure 5.7. For position 165° interactions show the presence of a developed migrating inner-wall dune with the initiation of outer-wall interactions.

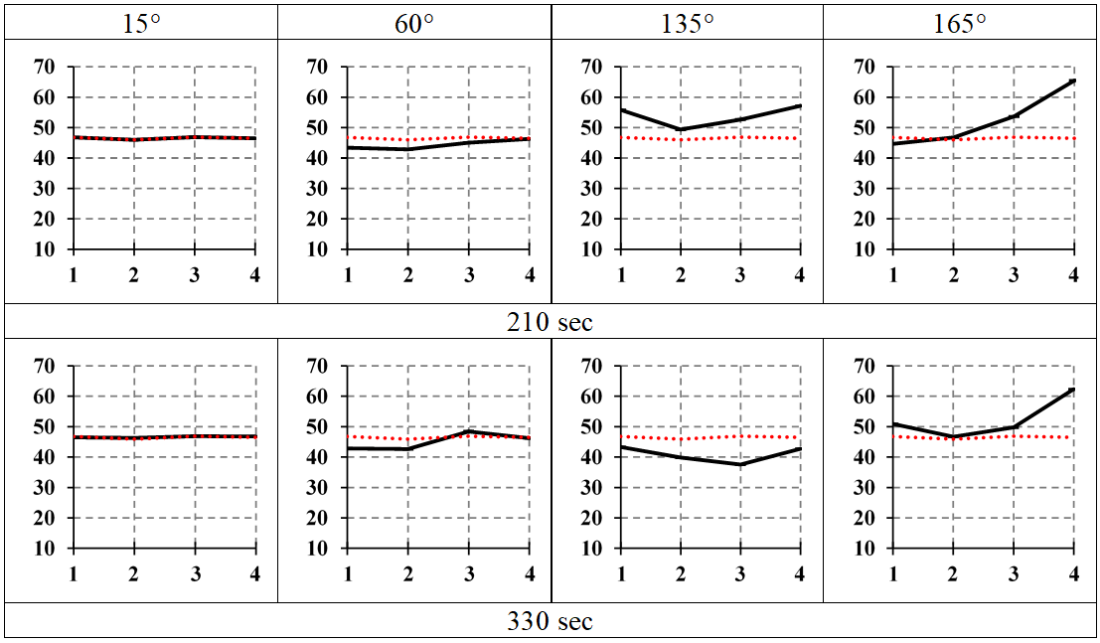

Figure 5.7: *Spatial evolution of bed profile @ 57 L/min flow rate. Y-axis shows bed height in mm, 1-4 on the X-axis indicates points arranged from the outer to inner-wall.*

At time step t = 330 sec the localised region of scour seen at t = 210 sec is shown tracking towards the inner-wall for 135°, with the lowest point across the bed at 135° moving from Point 2 to Point 3 at t = 330 sec. The complex bedform seen at 135° at t = 210 sec is seen being translated to the 165° position at t = 330 sec with the previously established inner-wall dune showing localised scour at its parameter with outer-wall interaction, seen as sedimentation.

At time step t = 570 sec, both positions 135° and 165° have progressed from complex interactions to the those of an oscillatory nature, with both showing the typically inclined bedforms previously described.

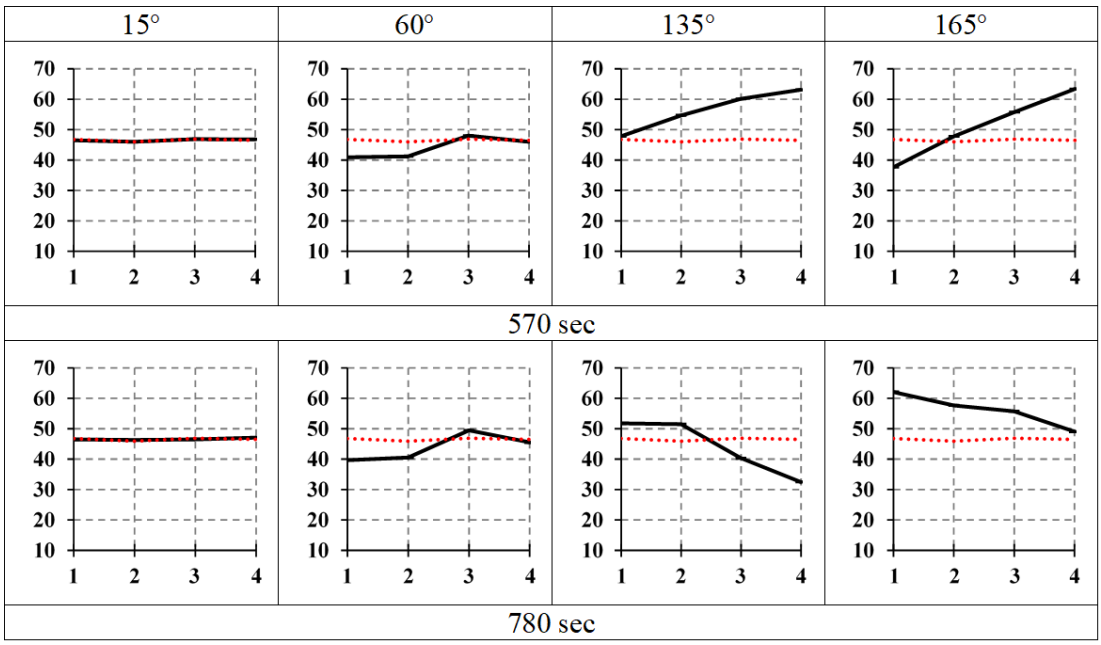

Figure 5.8: *Spatial evolution of bed profile @ 57 L/min flow rate. Y-axis shows bed height in mm, 1-4 on the X-axis indicates points arranged from the outer to inner-wall.*

The last time step t = 780 sec showed a continuation of dynamic interaction at both the 135° and 165° positions. Dynamic interactions are seen as a change in inclination for both positions, with the localised concentration of erosion occurring at the inner-wall region of the 135° position, showing a reduction in bed height at Points 3 and 4. The effects of interaction occurring 135° coupled with the migration of the oscillatory bed form upstream towards the outlet of the curved fluid passage are seen in the bed profile of 165°, with the bed experiencing significant outer-wall sedimentation along points 1 and 2 and erosion occurring at the inner-wall.

At an increased flow rate consistent behaviour at the 15° position along the curved fluid passage is observed, with the granular bed remaining stable with no measurable change in height. Moreover, as was the case for previous flow rates, the formation and presence of an inner-wall ridge at 60° were captured. The inner-wall ridge showed continued growth and development for all time steps, with the ridge-like nature seen by the bed profile at t = 780 sec. Furthermore, inwards transportation of eroded outer-wall granular bed material can be seen by

the concurrent decrease in outer-wall bed height and subsequent increase in the inner-wall ridge formation with increasing time.

5.1.5 Flow rate 60 L/min

The final spatial investigation was done for the flow rate of 60 L/min. At t = 130 sec interactions 135° showed complex Fluid-granular interactions also seen in previous flow rates, with the presence of an inner-wall and scour path located at the outer-wall (Point 1). The 165° position showed a rapid transition to an inclined bedform, with sedimentation increasing towards the inner-wall along the cross-section. At time step t = 300 sec position 135° transitioned to oscillatory interactions with the erosion seen as scour at t = 130 sec taking effect and producing strong localised erosion at Points 1 (outer-wall) and 2. Localised erosion was seen at the same time step to take place at 165°, with the change in bedform seen when comparing the cross-sections of t = 130 sec and t = 300 sec.

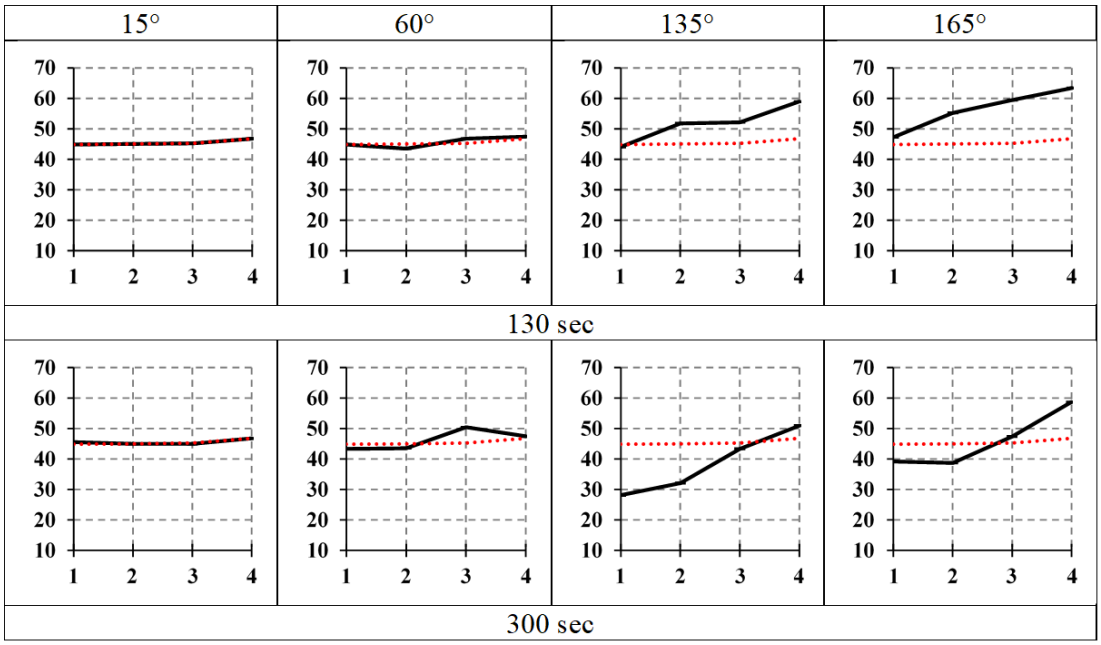

Figure 5.9: *Spatial evolution of bed profile @ 60 L/min flow rate. Y-axis shows bed height in mm, 1-4 on the X-axis indicates points arranged from the outer to inner-wall.*

Continued dynamic changes in bed height and profile continued at t = 490 sec. For the 135° position general increase in bed height along all points was seen. Similarly, at 165° with a substantial increase in bed height is recorded with a typical inclined bed profile dominated with inner-wall sedimentation.

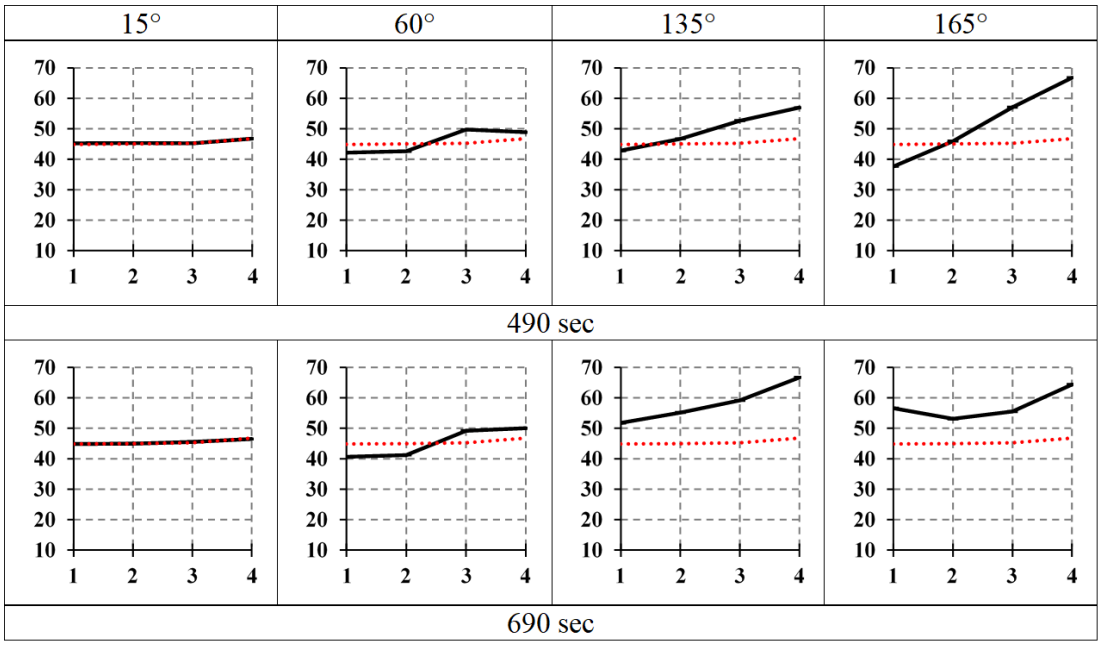

Figure 5.10: *Spatial evolution of bed profile @ 60 L/min flow rate. Y-axis shows bed height in mm, 1-4 on the X-axis indicates points arranged from the outer to inner-wall.*

In the last time step of t = 690 sec, the general trend of interaction at 135° is continued with an increase across all points. For position 165°, the sedimentation dominant conditions experienced upstream are seen to influence the sedimentation of granular material at Points 1 (outer-wall) and 2 when compared to the previous time step.

For the flow rate of 60 L/min, the 15° is recorded to be stable with no interactions captured over all the time steps presented. As with previous, the development of an inner-wall ridge at 60° was seen with a more prominent ridge developing at t = 300s and widening of the ridge towards the inner-wall at t = 690 sec. Furthermore, localised erosion can be seen at Points 1 and 2, in line with the observations for a flow rate of 57 L/min.

5.1.6 Summary of Spatial Investigation

Observations pertaining to spatial results show the dominance of interactions along the outlet half (90°-180°) of the curved fluid passage, with no measurable interaction occurring within the first 15° and the consistent formation of an inner-wall ridge located along the 60° position. The presence of an inner-wall ridge was observed for all flow rates (47, 50, 53, 57 and 60 L/min) during spatial investigation. Observations made during the qualitative assessment of Fluid-granular interaction correspond to those seen during spatial investigations. Two of the three stages of interactions described during the qualitative description of interactions, namely the initial stage and transient stage are captured during spatial investigation. With the formation and migration of inner-wall dunes seen at both 135° and 165° along the curved fluid passage during the initial stage, and the transitional stage marked by oscillatory and dynamic changes in the granular bed, seen at flow rates 50, 53, 57 and 60 L/min. The third stage, the quasi-stable stage was not captured during the spatial investigation.

Bed profiles showing uneven interactions and sudden and dynamic changes, those shown for positions 135° and 165°, and the development of the inner-wall ridge at 60° suggest the influence of secondary flow structures, and a mutually coupled relationship between these structures and the granular bed formations produced as a result of these interactions. Moreover, the effects of this mutually coupled relationship are seen to increase towards the outlet (180°) of the curved fluid passage.

Results obtained during the spatial investigation assist in the visualisation of dune formation, migration and bed erosion patterns attributed to dominant secondary flow effects. Nevertheless, as discussed earlier, the quasi-stable state was not captured and cannot easily be explained through spatial investigation alone. The time-dependent nature of quasi-stable interactions would best be investigated using temporal analysis. Hence, the final stage and the transitions between stages are illustrated in the subsequent section of temporal analysis.

The insight gained from spatial investigation allowed for the identification of a radial position of interest for temporal analysis, namely 135°. This position presented the most likely location for capturing dynamic Fluid-granular interactions, based on both qualitative observations and those gathered during spatial investigation. Selection of this position in favour of 165° also enabled the exclusion of any potential effect due to the outlet duct on the results presented.

5.2 Temporal investigation: An Eulerian overview at a fixed cross-section

Temporal investigation of critical parameters, namely, flow rate and particle mean diameter are expected to play a pivotal role in Fluid-granular interactions. The current section investigates the influence of these parameters to quantify the effect on timescale. To achieve these ends, temporal analysis is carried out at the fixed cross-section of 135° for combinations of various flow rates and mean particle diameter of the granular bed.

The results presented in this section are chosen from repeated tests to ensure all three stages are illustrated well, spaning flow rates 47, 50, 53, 57, 60 and 63 L/min. The measured bed height has been normalised using an initial height of 50 mm. The temporal investigation was continued until the quasi-stable stage of interactions is reached, seen as an asymptotic temporal plot for all four points across the 135° position. The test was run to allow the capture of all three stages identified previously; premature termination of experiments was due to the presence of scour persisting at the solid edge of the outlet's straight section. This localised scour induced a new mechanism of erosion, resulting from backflow created by the exposed solid edge of the outlet straight section. The prevention of backflow induced by this localised scour is the main reason for the difference between recording duration of various flow rate cases, represented the current section.

5.2.1 Granular Bed: 300 – 400 μm

The majority of experiments undertaken for temporal analysis presented are for a granular bed containing material of a size range 300 – 400 μm. Size range selection was made by taking the range which would provided the most substantial amount of sieved material for experimentation. Additionally, this allowed for two size ranges one smaller and one larger to be selected for parametric analysis, allowing all three beds to meet of the definitional requirements for granular material.

5.2.2 Flow rate 47 L/min

The minimum flowrate required to observe interactions between the fluid and the granular bed, with the given particle size range (300 – 400 μm), was determined through trials of flow variation. At a flow rate of 46 L/min, individual grains were observed being displaced from the granular bed and proceeded to roll along the surface; this occurred sporadically. This flow rate is seen to demarcate the inception of interaction between the fluid phase, and the granular bed, occurring gradually with slow sedimentation along the inner-wall (Point 4). Figure 5.11 represents Fluid-granular interaction across four points at a fixed cross-section for a flow rate of 46 L/min, with the black dashed vertical lines demarcating the transition between different stages of interaction.

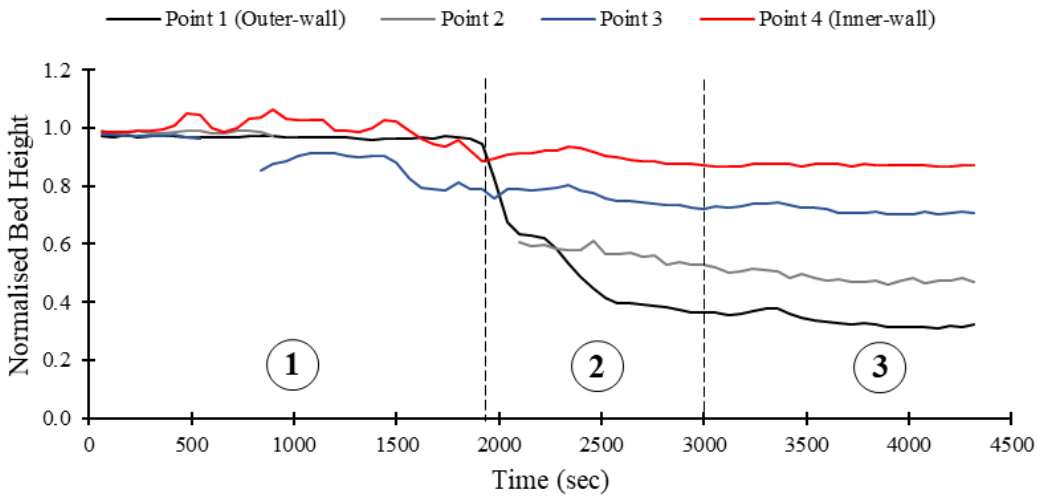

Figure 5.11: *Temporal plot for 300 – 400 μm, Flow rate = 47±2 L/min, EXP-135-300-47-03*

Initial interaction occurred at the inner-wall (Point 4), seen by the formation of inner-wall dunes, the effect of which are height fluctuation at this location, with the passing of inner-wall dunes seen at t = 500, 900 and 1500 sec. The gradual transition of Fluid-granular interactions towards the outer-wall is seen. As previously discussed, the gradual outward movement of interaction is characteristic of interactions described during the initial stage (Stage.1).

At t = 1900 sec, interaction has extended towards the outer-wall (Point 1). The transition of which demarcated the start of the transient stage (Stage.2). The transient stage at 46 L/min was characterised by the gradual progression of

erosion dominant interaction towards the outer-wall (Point 1), with the most significant degree of interaction occurring at this location. The transition from initial outer-wall erosion to the quasi-stable stage (Stage.3), denoted by the asymptotic profile of each point, occurred over approximately 1100 sec. From this point onward, the quasi-stable period (Stage.3) continues with minimal variation in the granular bed profile.

5.2.3 Flow rate 50 L/min

Interactions captured for an increased target flow rate of 50 L/min, Figure 5.12, show the initial result of such interactions to be inner-wall dominate in nature. Localised scour is seen at Point 3 for t ≈ 300 sec marking the initial identifiable interaction. The development of an inner-wall dune occurred at t ≈ 350 sec, seen as the gradual rise in bed height due to sedimentation at Point4 (inner-wall). Progression of interactions towards the outer-wall (Point 1) is shown, with the transient stage (Stage.2) beginning with the onset of erosion at t ≈ 500 sec.

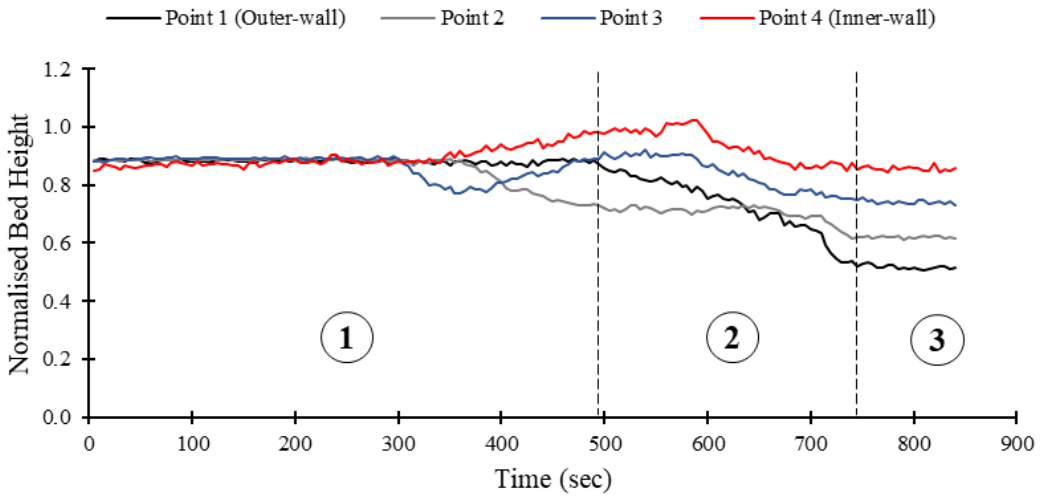

Figure 5.12: *Temporal plot for 300 – 400 µm, Flow rate = 51±1 L/min, EXP-135-300-50-10*

Interactions during the transient stage (Stage.2) consists of a general trend of erosion at all Points across the investigation area (135°). Quasi-stable stage (Stage.3) was reached at t ≈ 740 sec when compared to results obtained for Figure 5.11, a comparable temporal profile can be seen, with Figure 5.12 showing a marked decrease in temporal scale for the establishment and transition of stages to occur. Many of the results presented for 50 L/min, were seen to be sensitive to perturbation, and show inconstant behaviour.

5.2.4 Flow rate 53 L/min

A more consistent and general trend is seen developing for results at a target flow rate of 50 L/min. Seen in Figure 5.13, initial Fluid-granular interactions occurred at the inner-wall (Point 4) within 100 sec, denoted by an increase in bed height due to sedimentation. The general trend of interactions moving towards the outer-wall (Point 1) is continued, with the transient stage (Stage.2) occurring at t ≈ 200 sec. The transient nature of this stage can be seen in Figure 5.13, with the temporal profile for Point 4 (inner-wall) transitioning between periods of erosion and sedimentation. At t ≈ 670 sec Fluid-granular interaction seen in Figure 5.13, transition into the quasi-stable stage (Stage.3)

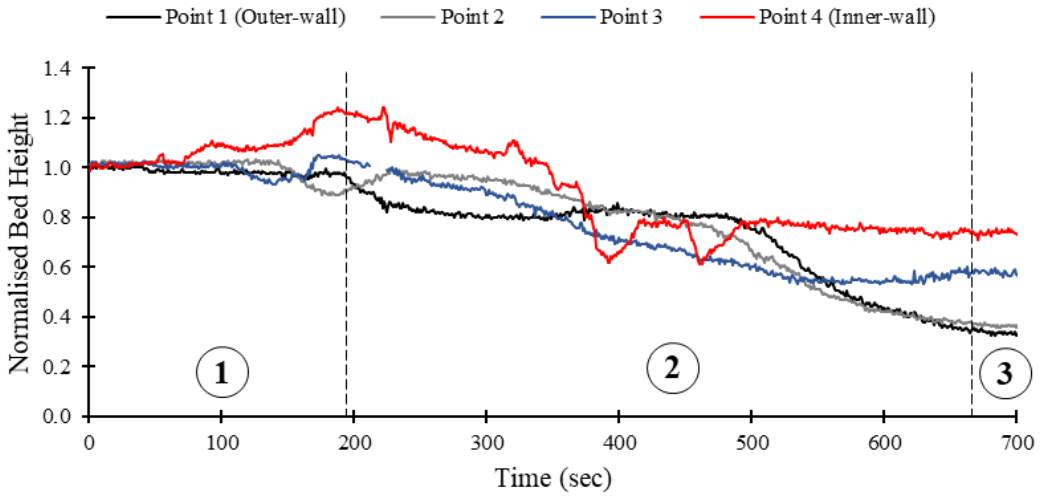

Figure 5.13: *Temporal plot for 300 – 400 μm, Flow rate = 54±2 L/min, EXP-135-300-53-02*

For Figure 5.14, initial interaction occurred at the inner-wall (Point 4), with a gradual increase in bed height this gradual increase shows the growth of inner-wall dunes, coupled with the rapid growth of these dunes during the initial stages of interaction. The presence of this inner-wall dune can be seen by the increase in bed height at Points 3 and 4 at t = 150 sec, corresponding erosion seen at this same temporal position at Point 2 is a result of scour occurring around the parameter of the dune. The widening of inner-wall dunes and the displacement of localised scour towards the outer-wall (Point 1) can be seen at the onset of the transient stage (Stage.2) at t ≈ 170 sec, with the scour region extending outward from Point 3 to Point 1(outer-wall) as time progressed.

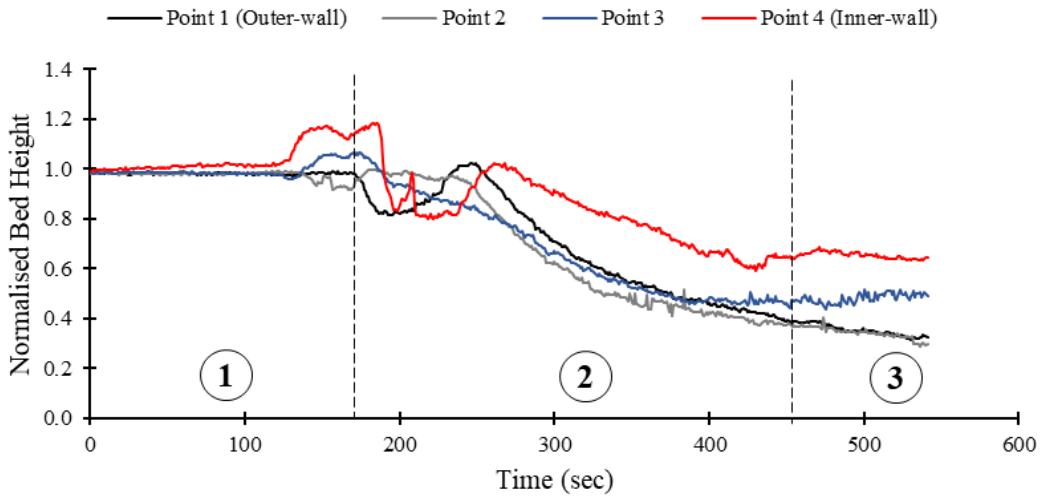

Figure 5.14: *Temporal plot for 300 – 400 µm, Flow rate = 53±2 L/min, EXP-135-300-53-04*

The transient stage (Stage.2) for Figure 5.14, shows dynamic interaction occurring both at the inner-wall (Point 4) and outer-wall (Point 1), showing oscillatory behaviour between t =170 sec and t = 300 sec. The gradual process of interaction stabilisation seen from t = 300 sec, with all Points continuing a general decrease in bed height with the transition to quasi-stable Fluid-granular interaction occurring at t ≈ 450 sec.

5.2.5 Flow rate 57 L/min

The flow rate of 57 L/min, produced the most constant and repeatable set of interaction. The basis for the categorisation and temporal description of the three staged of fluid-granular interactions are the most prominent flow rate. For Figure 5.15, the initiation of interaction seen by the presence of inner-wall dunes is seen early. The transition of interactions to the outer-wall (Point 1) occurred at t $\approx$ 50 sec, demarcating the start of the transient stage (Stage.2). The inner-wall (Point 4) shows the most significant instability, with the bed height transitioning between periods of erosion and sedimentation several times. The gradual stabilisations of interactions are seen at t $\approx$ 220 sec with the granular bed decreasing in height across all Points, with the quasi-stable stage staring at t = 600 sec.

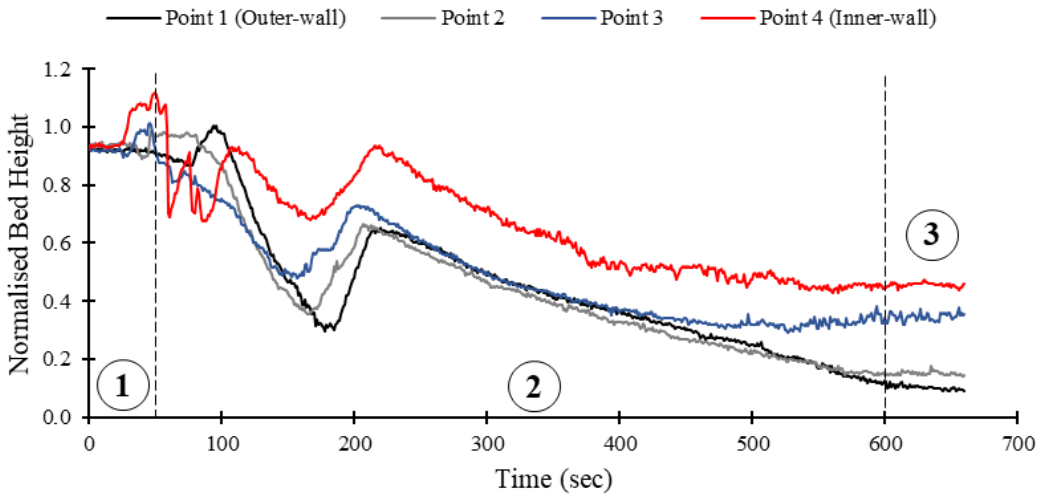

Figure 5.15: *Temporal plot for 300 – 400 µm, Flow rate = 57±2 L/min, EXP-135-300-57-01*

Interactions are shown in Figure 5.16, show the start of the transient stage (Stage.2) at t ≈ 140 sec. Dynamic behaviour of Fluid-granular interactions is seen increasing towards the outer-wall, with the temporal profiles of Point 3, 2 and 1 showing increased oscillatory behaviour. The oscillatory behaviour halted at t ≈ 270 sec with a gradual transition to the quasi-stable interaction (Stage.3) occurring at t ≈ 520 sec.

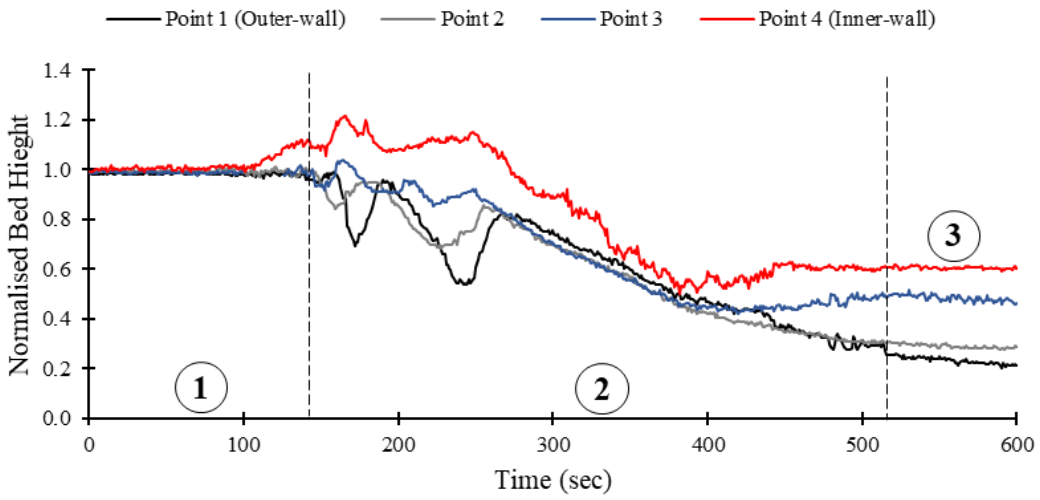

Figure 5.16: *Temporal plot for 300 – 400 μm, Flow rate = 58±2 L/min, EXP-135-300-57-07*

A more rapid set of interaction is captured in Figure 5.17, which shows the best temporal description of the initial, transient and quasi-stable stages. The initial formation of inner-wall dunes is seen with the increase in height at Point 3, and 4 (inner-wall). Additionally, the scour produced due to the growth of the inner-wall dune can be seen between t = 180 sec and t = 200 sec with the decrease in bed height for point 2. The transient stage beginning at t = 200 sec is marked by the displacement of localised scour to the outer-wall (Point 1). The repeated pattern of oscillatory temporal profiles is seen during the transient stage, with the outer-wall (Point 1) experiencing the most dynamic interactions. Stabilisation of interactions occurs relatively rapidly with the quasi-stable stage (Stage.3) being reached at t = 400 sec. The quasi-stable nature of this period can be seen by the consistent bed height for the remainder of temporal results.

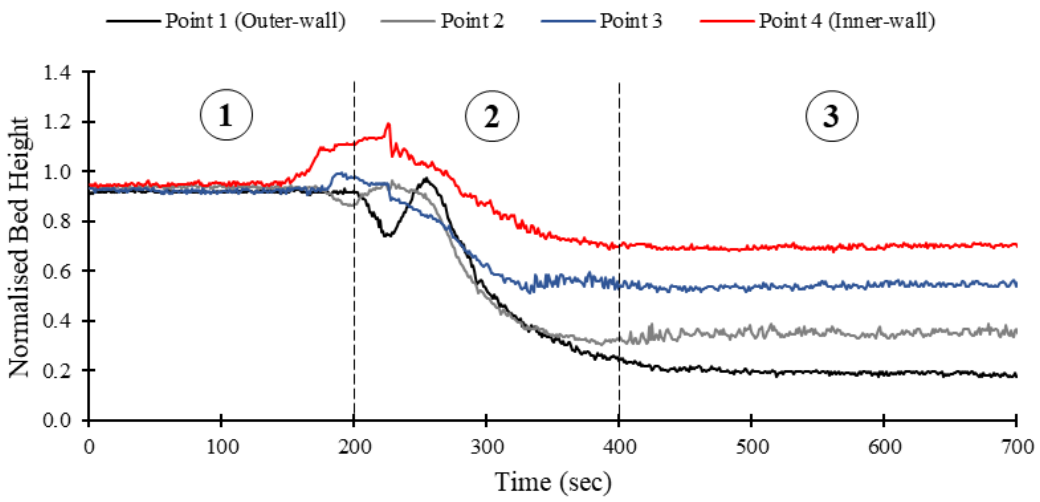

Figure 5.17: *Temporal plot for 300 – 400 µm, Flow rate = 58±2 L/min, EXP-135-300-57-02*

The remarkable similarity in temporal profiles and can be seen in Figure 5.17 when comparison is made to Figure 5.18. The intuition of the transient stage being at t ≈ 180 sec, with transient behaviour occurring at all Points. The gradual decay to stable Fluid-granular interaction is initiated at t ≈ 250 sec, with the process continuing till t = 500 sec marking the quasi-stable stage (Stage.3).

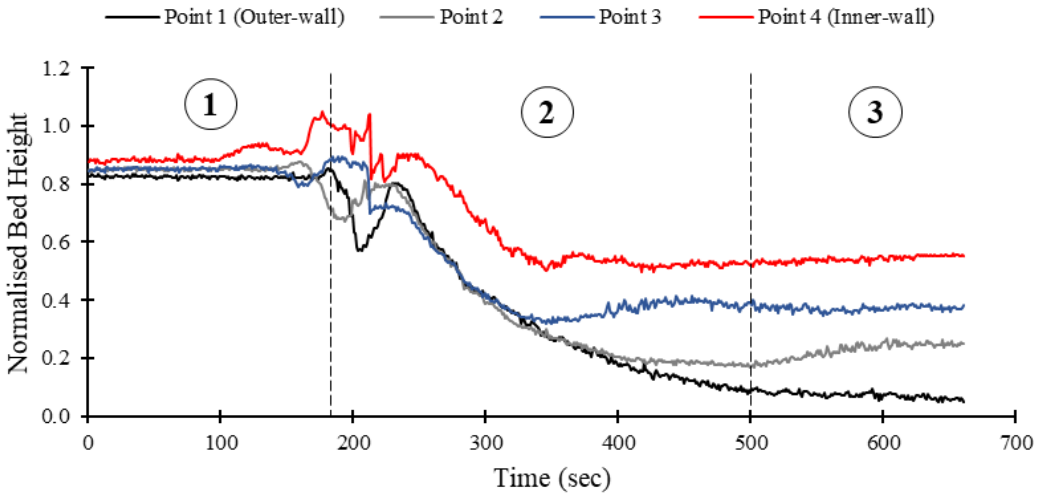

Figure 5.18: *Temporal plot for 300 – 400 µm, Flow rate = 57±2 L/min, EXP-135-300-57-04*

5.2.6 Flow rate 60 L/min

With an increase in flow rate to 60 L/min, a change in the transient stage (Stage.2) is seen. Figure 5.19 shows the transient stage (Stage.2) beginning at t ≈ 60 sec, the transient nature of Fluid-granular interaction is seen to persist for a more extended period when compared to previous flow rates. Between t = 60 – 150 sec, interaction at the inner-wall (Point 4) and outer-wall (Point 1) differ in the dominate process occurring, with erosion being dominate at the outer-wall (Point 1) and sedimentation at the inner-wall (Point 4). At t ≈ 200 sec, all four Points are seen to oscillate, seen as a convergence in temporal behaviour. This is a result of the granular bed taking the form of migrating dunes extending the entire width of the investigation area. The prolonged transient nature of interaction continues with a change in bed inclination seen starting at t ≈ 340 sec with the inner-wall (Point 4) being eroded to the lowest bed height. The inclination is then reversed once more, at t ≈ 460 sec at which point the granular bed is seen to enter the quasi-stable stage (Stage.3) at t ≈ 560 sec.

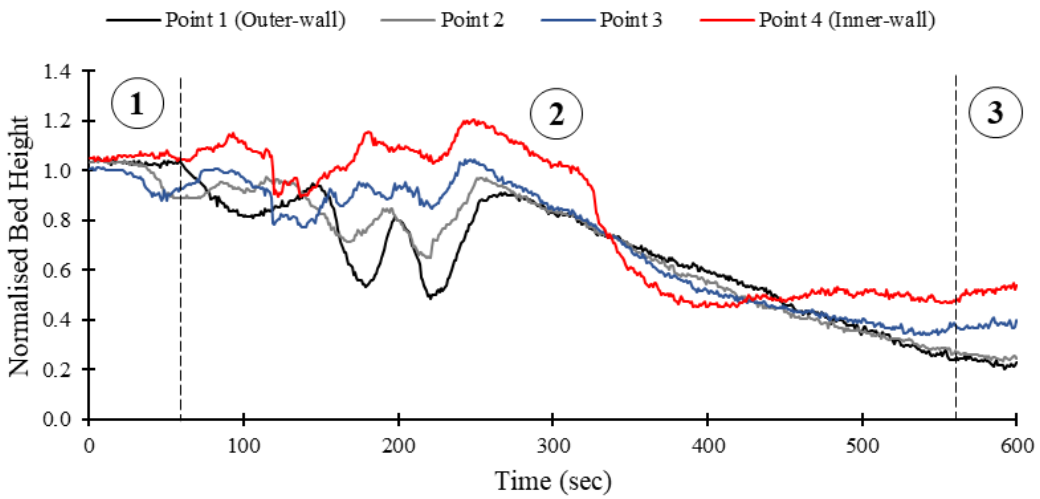

Figure 5.19: *Temporal plot for 300 – 400 μm, Flow rate = 62±3 L/min, EXP-135-300-60-02*

Interactions captured in Figure 5.20, show the initiation of the transient stage (Stage.2) occurring at t ≈ 40 sec. An extended transient stage also captured for Figure 5.20, with all four Points showing oscillatory convergence, seen as in phase temporal behaviour of bed height fluctuations. After t ≈ 250 sec interactions are dominated by erosion for all four Points, with the establishment of quasi-stable Fluid-granular interactions at t ≈ 570 sec.

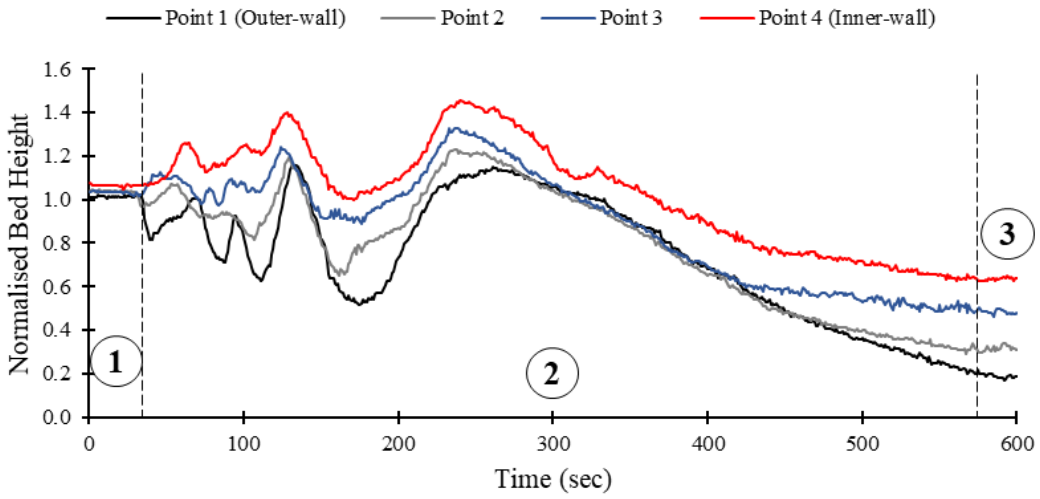

Figure 5.20: *Temporal plot for 300 – 400 µm, Flow rate = 61±3 L/min, EXP-135-300-60-03*

The continued theme of an extended transient stage (Stage.2) is seen in Figure 5.21. The transient stage beginning at t ≈ 40 sec, with all four Points temporally converging at t ≈ 80 sec. For Figure 5.21, the transient stage is seen to be dominated by sedimentation at the inner-wall with the granular bed increasing in height substantially at t ≈ 260 sec. As with previous results, the transition to quasi-stable Fluid-granular interactions is gradual with erosion dominating this transition until at t ≈ 580 sec the quasi-stable stage (Stage.3) is reached.

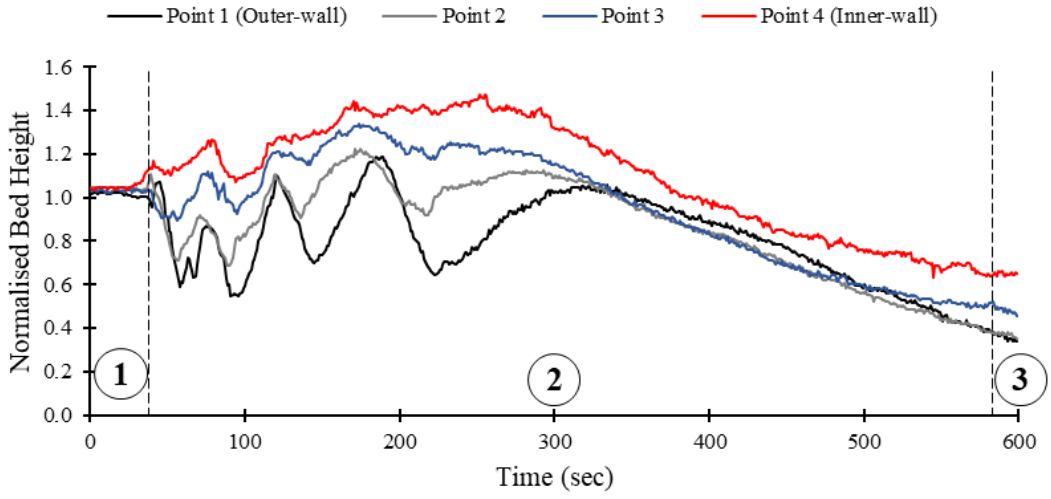

Figure 5.21: *Temporal plot for 300 – 400 µm, Flow rate = 62±3 L/min, EXP-135-300-60-04*

5.2.7 Flow rate 63 L/min

The final flow rate investigated for a particle size range of 300 – 400 μm, showed a notable change in resulting granular bed profile due to Fluid-granular interactions. The transient stage (Stage.2) began at t $\approx$ 110 sec. The now characteristic dynamic and oscillatory interactions which were observed at previous flow rates no longer occurred. The transient stage (Stage.2) was ended at t = 200 sec with all points at the stabilising about respective bed heights, with sedimentation dominating Point 4 (inner-wall) and Point 3 and erosion Point 2 and 1 (Inner-wall).

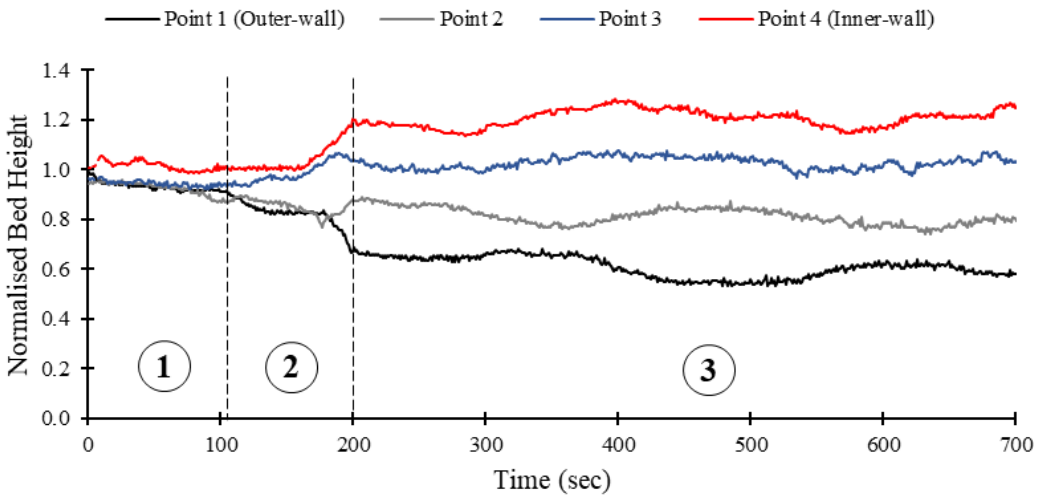

Figure 5.22: *Temporal plot for 300 – 400 μm, Flow rate = 64±3 L/min, EXP-135-300-63-01*

5.2.8 Summary of Temporal Investigation

Temporal analysis of undertaken for a granular bed of size range 300 - 400 μm, identified three distinct stages of interaction, namely the initial stage (Stage.1), transient stage (Stage.2) and the Quasi-stable stage (Stage.3). These three stages are seen to be present over the range of flow rates examined (47 – 63 L/min). The effects of flow rate on Fluid-granular interactions are seen when a comparison of the bed reshaping process, for various flow rates is made. Consistent evolution of the granular bed configuration and the faster progress toward established (quasi-stable) Fluid-granular interactions, is captured with increasing flow rate.

Observations made during the transient stage showed that with an increase in flow rate coinciding with an increase in dynamic interactions, noting that these dynamic interactions were captured first for a flow rate of 53 L/min (Figure 5.13 and 5.14). The nature of Fluid-granular interactions occurring during the transient stage shows the most reliable evidence of the effects of secondary flow instability and the subsequent effect on granular bed reshaping. Additionally, the effects of secondary flow instability are seen to be strongest at the outer-wall. The temporal profiles of Point 1 in Figures 5.17, 5.18 and 5.18 showing both the effects of localised erosion attributed to increased velocity, but also the oscillatory and transient nature of these profiles suggest an intricate mutually coupled relationship between secondary flow structures present in the curved duct and the granular bed.

The duration of the transient stage is seen to decrease with flow rate, with the notable exception of 60 L/min were, as can be seen in Figures 5.19, 5.20 and 5.21, the transient stage is extended with a subsequent delay in the onset of the quasi-stable stage. This extended transient stage is marked by increased oscillatory interaction, seen as dunes passing the investigation area. At higher flow rates the temporal convergence is captured for all points seen as temporal in phase behaviour.

The quasi-stable stage previously described is captured for all the flow rates presented (47, 50, 53, 57, 60 and 63 L/min). The nature of the quasi-stable stage was seen by the general asymptotic nature of the temporal profiles for all for points across the investigation area. This asymptotic nature in the temporal profiles, suggest the stabilisation of Fluid-granular interactions. This stabilisation may be a result of the presence of localised secondary flow structures coupled with the granular bed morphology acting to stabilise the granular bed. Moreover, the

general trend for quasi-stable stage was seen as a granular bed profile with the outer-wall (Point 1) showing the most significant degree of erosion, and therefore the highest degree of interaction, with the bed height increasing towards the inner-wall (Point 4). The inner-wall inclined granular bed profile is the predominate behaviour captured, which is consistent with the broadest range of flow rates and selected as such. A change in temporal behaviour was seen at 63 L/min (Figure 5.22), with the quasi-stable stage maintained for the majority of the experimental time scale. Additionally, when compared to temporal profiles of previous flow rates a definite change in the behaviour of Fluid-granular interactions is seen.

The effect of perturbation may explain the stochastic nature of interaction at lower flow rates. Perturbation effects are seen to be reduced with increasing flow rate owing to the increased momentum transfer between the fluid phase and granular phase, therefore negating the effects of surface imperfects or uneven bed morphology.

5.3 Particles dimensions

Particle dimensions are a key parameter concerning drag analysis of individual particles and for investigation of two-phase interaction. Therefore, any systematic sensitivity analysis of fluid-granular interactions involves a change in granular bed particle dimensions. Temporal analysis has been carried out at a fixed cross-section (135°), for two different granular beds of particle size ranges (150 – 300 μm and 475 – 1180 μm) and compared to that of the reference granular bed (300 – 400 μm), presented in Section 3. Temporal behaviour is captured for the respective granular beds at increasing flow rates with a comparative investigation represented in Figures 5.30, 5.31 and 5.32.

5.3.1 Particles dimensions 150 - 300 μm

The granular bed size range of 150 – 300 μm represents the smallest particle range presented and is close to the definitional limits for a granular material; where particles must be greater than 100 μm. Temporal analysis is undertaken, using the same methods used for the reference granular bed (300 – 400 μm), with the minimum flow rate determined using the same criteria, namely the point at which individual grains can be seen being displaced along the granular bed. Once the minimum flow rate is established, the flow rate is increased for each subsequent experiment, allow for the comparison of temporal behaviour.

5.3.1.1 Flow rate 47 L/min

Incipient particle movement was identified at a flow rate of 47 L/min; initial displacement occurred early during the initiation stage (Stage.1), seen as the increase in granular bed height at the inner-wall (Point 4). The majority of the initiation stage was dominated by interactions at the inner-wall, where an inner-wall dune is seen occupying Point 4.

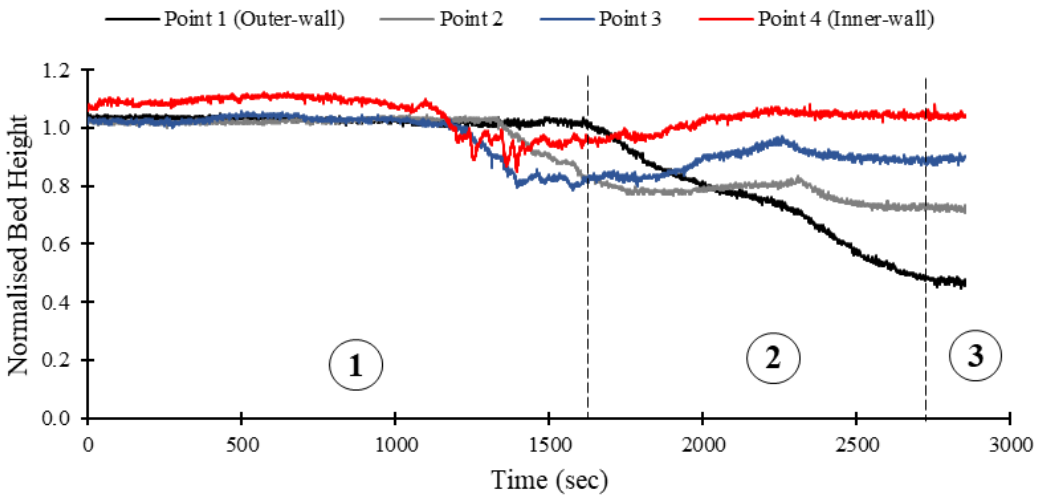

Figure 5.23: *Temporal plot for 150 – 300 μm, Flow rate = 46±1 L/min, EXP-135-150-47-02*

Transition to outer-wall erosion can be seen to occur gradually as Fluid-granular interaction progress steadily in an outward direction. At t ≈ 1650 sec, interactions enter the transient stage (stage.2), identified by erosion at the outer-wall (Point 1). Interactions during the transient stage were less dynamic in comparison to those at later stages of the initial stage (t ≈ 1200 – 1650 sec). Temporal profiles were seen in Figure 5.23, show the gradual decay of interactions and the initiation of the quasi-stable stage (Stage.3), seen to begin at t ≈ 2750 sec.

5.3.1.2 Flow rate 50 L/min

An increased flow rate of 50 L/min, shows interaction in Figure 5.24 to be comparable in temporal profile to Figures 5.20 and 5.20. The prevailing trend of inner-wall dune formation seen in Figure 5.24 associated with the gradual increase in bed height of Point 4 (inner-wall) and Point 3 is captured. The transient stage (Stage.2) is reached at t ≈ 75 sec, seen by concentrated erosion at the outer-wall (Point 1).

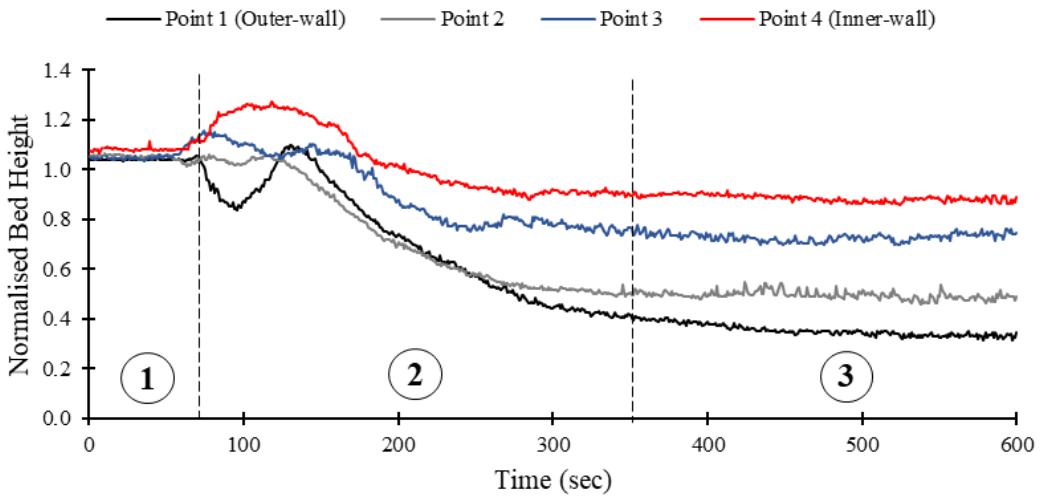

Figure 5.24: *Temporal plot for 150 – 300 μm, Flow rate = 50±1 L/min, EXP-135-150-50-01*

Interactions at the outer-wall exhibit oscillatory behaviour in line with previous observations. The gradual transition towards quasi-stable interactions is seen for all points across the investigation area with the quasi-stable stage (Stage.3) staring at t ≈ 350 sec. Interaction during the quasi-stable stage is remarkably stable with this period making up almost half of the temporal scale of the experiment.

5.3.1.3 Flow rate 53 L/min

At a flow rate of 53 L/min, interaction during the initial stage (Stage.1) show the development of inner-wall dunes and the gradual transition to outer-wall interactions. Regions of localised scour can be seen during this period at Point 3 and for Point 2. This behaviour is shown in Figure 5.25 is linked to regions of scour seen in Figure 4.5a and 4.5b, Section 4.1.

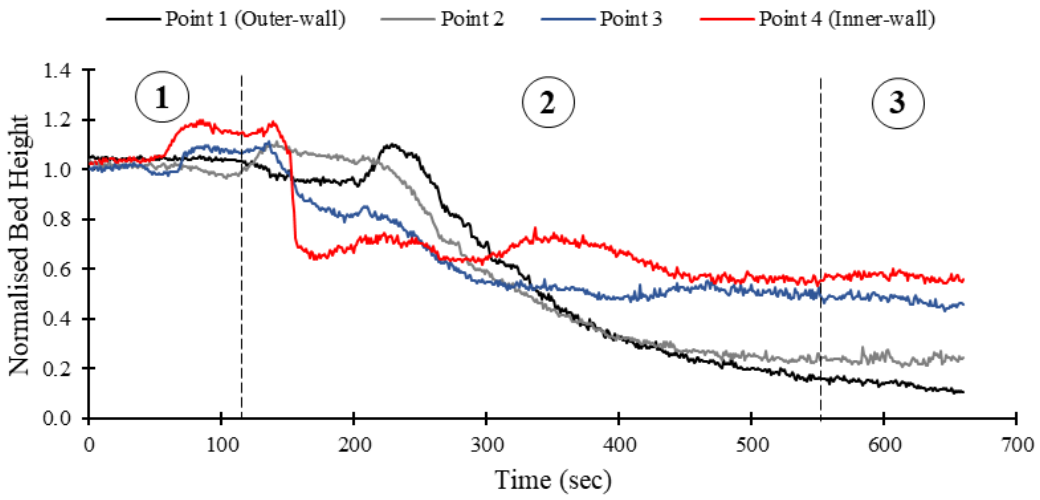

Figure 5.25: *Temporal plot for 150 – 300 µm, Flow rate = 53±1 L/min, EXP-135-150-53-01*

The gradual outward movement of scour and the eventual interaction at the outer-wall (Point 1) marked the start of the transient stage (Stage.2) at t ≈ 115 sec. During the transient stage, an intense period of erosion occurred at the inner-wall (Point 4), with a sharp decrease in the granular bed height at this point. Increased dynamic Fluid-granular interactions occurred during the transient stage (Stage.2) relative to previous flow rates. Moreover, the transient stage (Stage.2) is extended when compared to Figure 5.25, with the quasi-stable stage (Stage.3) initiated at t ≈ 560 sec.

5.3.1.4 Flow rate 57 L/min

The final flow rate tested for the granular bed size range of 150 – 300 μm, seen in Figure 5.26, was 57 L/min. Interactions during the initial stage (Stage.1), showed little measurable change in granular bed height, with no formation or development of inner-wall dunes present. At t $\approx$ 60 sec interactions across all four points are seen, with the formation of an inner-wall dune which occupied Points 4, 3 and 2 across the integration area. Additionally, this marked the start of the transient stage (Stage.2), with erosion occurring at the outer-wall (Point 1).

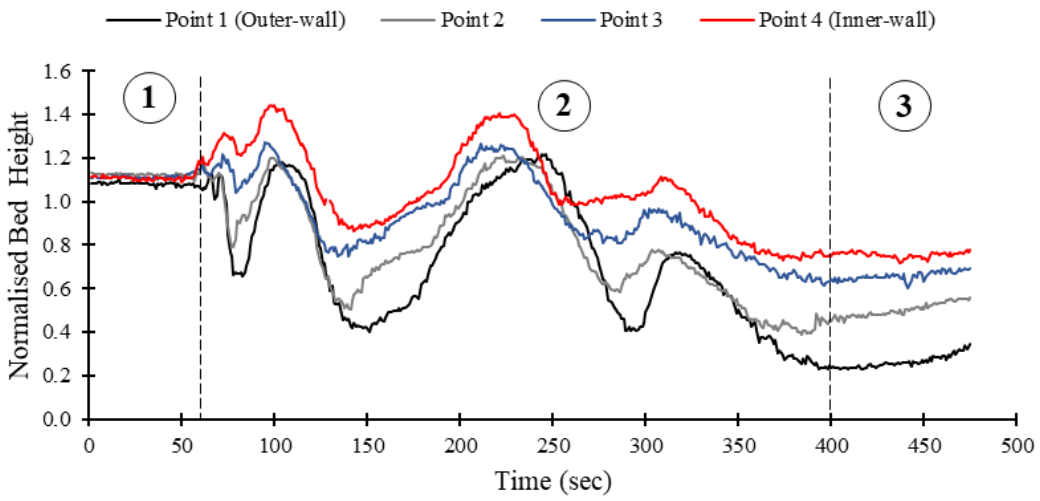

Figure 5.26: *Temporal plot for 150 – 300 μm, Flow rate = 57±1 L/min, EXP-135-150-57-04*

The transient stage (Stage.2) shows strong oscillatory behaviour for all points across the investigation area. An extended period of interactions is seen, and the transient nature of this stage is best illustrated by the profiles shown above. Furthermore, the temporal behaviour of Figure 5.26 is more in line with that of Figure 5.20, both of which show the extended transient stage to occur at increased flow rates. Fluid-granular interactions are seen stabilising when entering the quasi-stable stage (Stage.3) at t = 400 sec.

5.4 Particles dimensions 475 – 1180 μm

The difference in particles sizes for previous granular bed size ranges investigated (150 – 300 μm and 300 – 400 μm) are relatively small. The granular bed investigated in this section comprises of particles with the largest size variation, with a range of 475 – 1180 μm. The effects of larger particles on Fluid-granular interaction due to both increased relative weight, but also due to increased effects of drag form the primary motivation for this size selection.

5.4.1 Flow rate 57 L/min

For a particle size range of 475 – 1180 μm, the incipient movement of granular material was seen to initiate at a flow rate of 57 L/min, see Figure 5.27. Fluid-granular interactions comprised of individual grains rolling along the surface of the granular bed. At t $\approx$ 100 sec, the transient stage (Stage.2) is initiated, seen by a marked transition across all points in the investigation area. Marked by the characteristic profile of inner-wall (Point 4) sedimentation and erosion progressing towards the outer-wall (Point 1). The quasi-stable stage (Stage.3) which initiated at t $\approx$ 190 sec, exhibited a continued and stable period of Fluid-granular interactions with the majority of the temporal profile taking place within this stage. Moreover, the temporal profiles were seen in Figure 5.27, show characteristics similar to that of Figure 5.22, with the granular bed transition into the quasi-stable stage with limited dynamic or oscillatory behaviour.

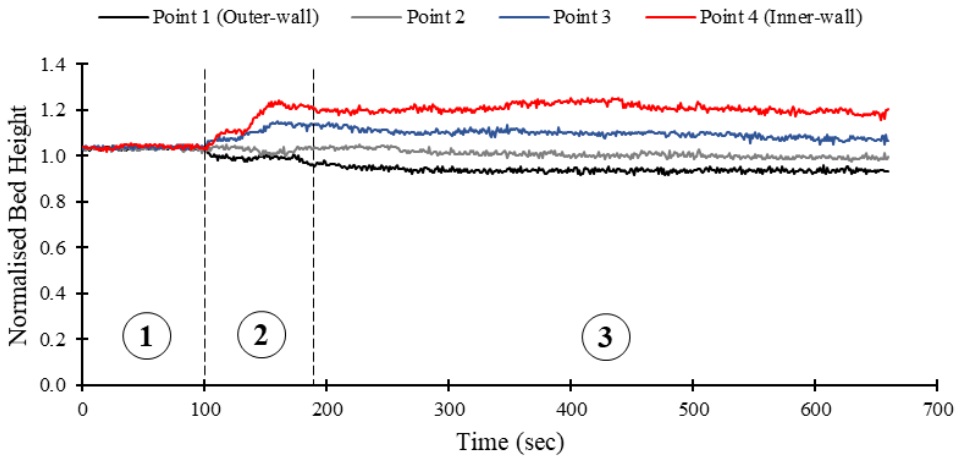

Figure 5.27: *Temporal plot for 475 – 1180 μm, Flow rate = 58±1 L/min, EXP-135-475-57-01*

5.4.2 Flow rate 60 L/min

An increased flow rate of 60 L/min seen in Figure 5.28, showed similar interaction to the previous flow rate, with the transient stage (Stage.2) occurring at t $\approx$ 70 sec. Interactions during the transient stage show more significant interaction at the outer-wall (Point 1) and Point 2 relative to Figure 5.27 during the same stage. Continued inner-wall (Point 4) sedimentation dominated interaction is seen during this period. The quasi-stable stage (Stage.3) of Fluid-granular interactions is reached at t $\approx$ 140 sec, with the granular bed showing relatively stable temporal behaviour during the remainder of the experiment.

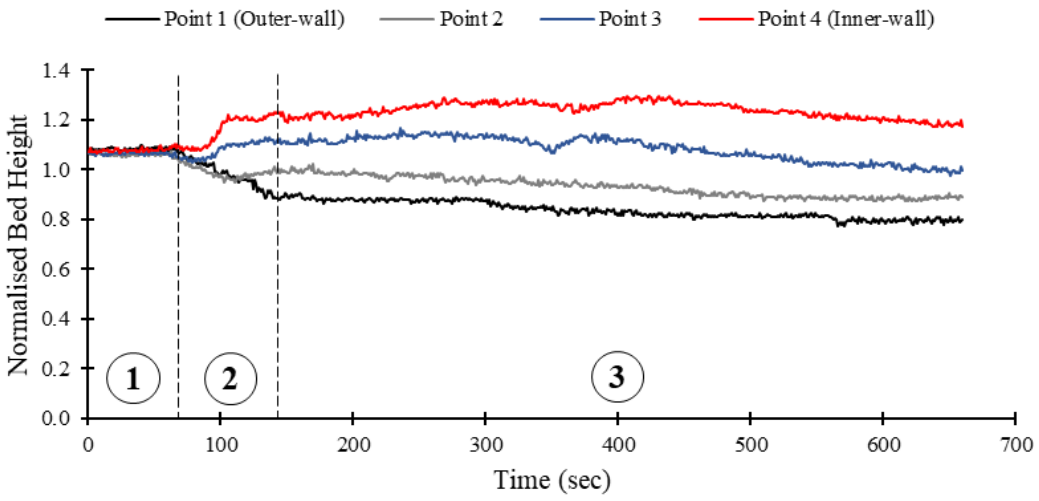

Figure 5.28: *Temporal plot for 475 – 1180 µm, Flow rate = 62±1 L/min, EXP-135-475-60-01*

5.4.3 Flow rate 63 L/min

The final flow rate investigated for a granular bed size range of 475 – 1180 μm was 63 L/min. The initiation stage (Stage.1) of interaction saw a gradual increase in inner-wall granular bed height, with the start of the transient stage (Stage.2) at t = 100 sec. Continued sedimentation seen as increased bed height is captured during this stage at Point 4 (inner-wall) and Point 3. At the outer-wall (Point 1) the predominant interaction is one of gradual erosion. Additionally, the transient stage is extended relative to those captured in Figures 5.27 and 5.28, with the transition to the quasi-stable stage (Stage.3) occurring at t $\approx$ 340 sec. The quasi-stable stage showed similar behaviour for all points across the investigation area, with stable Fluid-granular interactions continuing for the remainder of the temporal investigation.

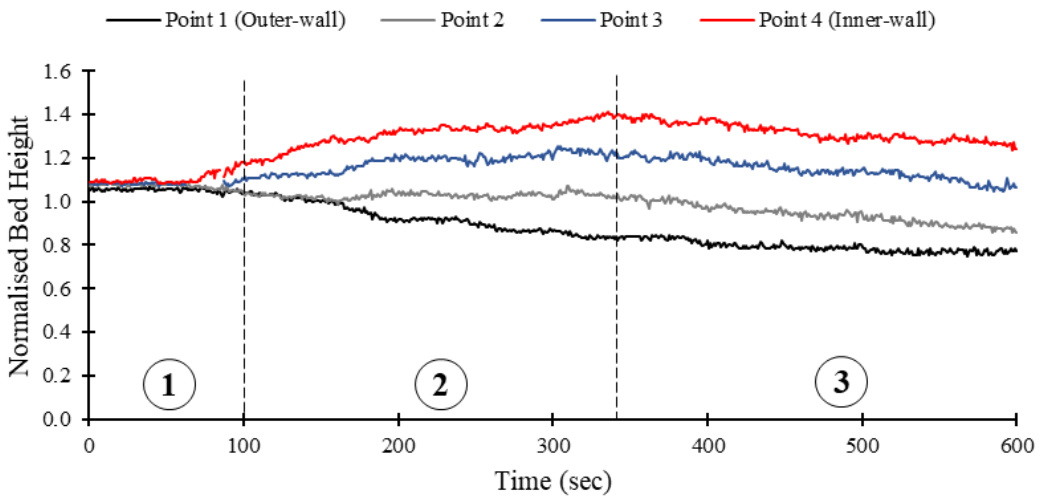

Figure 5.29: *Temporal plot for 475 – 1180 μm, Flow rate = 65±1 L/min, EXP-135-475-63-02*

5.5 Summary of Quantitative Experimental Results

Comparison between particle size range 100 – 300 μm and 475 – 1180 μm to the reference granular bed size range of 300 – 400 μm is made, owing to the reference granular bed's more substantial experimental data set, and the particle size range laying in the middle of the other granular beds.

Temporal analysis for the smallest of the granular bed size ranges (100 – 300 μm) determined that the flow rate required to observe grain movement along the granular bed surface was 47 L/min, showing the initiation of interactions to occur at the same flow rate as the reference granular bed of 300 – 400 μm. Similar initial interactions occurred at the inner-wall (point 4) at 47 L/min when comparing Figures 5.23 to Figure 5.11, noting the delayed onset of the transient stage for the granular bed of 100 – 300 μm. This is explained by the relationship between drag force experienced by the particles comprising the granular bed and the buoyancy force, the ratio of which is defined by the Shields number. Smaller particles experience reduced drag force due to the smaller contact surface area presented to the fluid phase, therefore delaying initial interaction. At an increased flow rate of 50 L/min the temporal behaviour shown in Figure 5.24 corresponds to interactions captured for the reference granular bed at a flow rate of 53 L/min and 57 L/min, see Figure 5.14 Figures 5.18.

These observed interactions at a reduced flow rate are due to the smaller particle weight relative to larger particles of the same density, once displaced the force required to remove and entrain the particle into the fluid phase is reduced. The effects of particle entrainment are captured at an increased flow rate 53 L/min, showing intensification in dynamic behaviour, with an extended transient stage (Stage.2) captured. The trend of increased dynamic interaction with an increase in flow rate is seen for a flow rate of 57 L/min (Figure 5.26). An increased transient stage (Stage.2) showing clear oscillatory Fluid-granular interaction marking a distinct change in interactions when compared to previous flow rates, and is comparable in behaviour to interactions seen in the reference granular bed at 60 L/min (Figure 5.21).

The largest granular bed particle size range of 475 – 1180 μm, demonstrates the sensitivity of Fluid-granular interaction to granular bed particle size range. The minimum flow rate required to capture reliable interactions was 57 L/min. Unlike, smaller granular bed particles sizes, temporal analysis showed that Fluid-granular interactions lacked the dynamic and oscillatory behaviour captured previously. The temporal behaviour captured at 57 L/min for 475 – 1180 μm (Figure 5.27) occurs at a lower flow rate than that of the reference granular bed (300 – 400 μm), which exhibits similar temporal behaviour at a higher flow rate of 63 L/min, seen in Figure 5.22.

As explained previously, the relationship between drag force and buoyancy force acting on a particle plays a significant role in the initiation of granular bed particle displacement and entrainment. Fluid phase interactions for larger grains are dominated by drag force, owing to the increased contact surface area presented to the fluid phase. The increased particle weight relative to smaller particles of the same density significantly reduces particle entrainment into the fluid phase; therefore interactions consist of rolling grains being displaced and deposited in relation to local flow conditions, creating the temporal profiles associated with the larger granular bed size of 475 – 1180 μm. The resulting temporal profiles for flow rates 57 L/min and 60 L/min, showed a reduced transient stage (Stage.2) and a prolonged quasi-stable stage (Stage.3). The reduced transient stage and the extended quasi-stable stage is attributed to the heavier grains which are less affected by smaller eddies, therefore allowing for the accumulation of displaced granular bed material from upstream of the area of investigation, and the resulting stabilisation of the granular bed and hence quasi-stable conditions is achieved faster.

A summary of the experimental results is presented in Figures 5.30, 5.31 and 5.32. Figure 5.30 shows the onset time for the transient stage (Stage.2) with respect to flow rate for all granular bed size ranges investigated. For a granular bed comprised of particles between 300 – 400 μm at lower flow rates the onset is delayed relative to higher flow rates, as flow rate is increased the onset time for the transient stage is seen to asymptote with flow rates 53 L/min to 61 L/min transitioning to the transient stage at similar times.

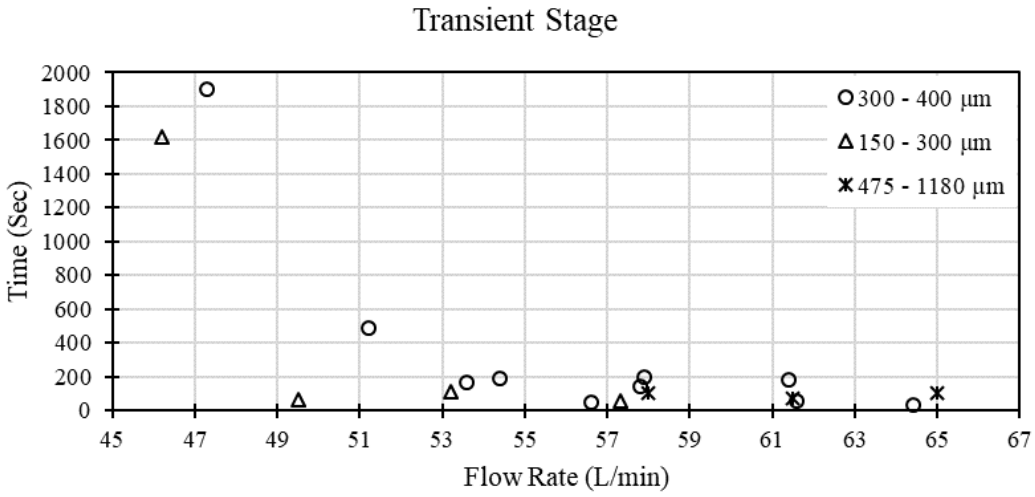

Figure 5.30: *The onset of transient stage for 150 – 300 μm, 300 – 400 μm and 475 – 1180 μm.*

For a granular bed comprising particles of 150 – 300 μm, similar behaviour at lower flow rates to the reference granular bed are seen, with a delayed onset 46 L/min. With increased flow rate the onset of the transient stage is again seen to asymptote, compared to the granular bed of 300 – 400 μm this occurred at reduced time. For the largest of granular bed particle size range 475 – 1180 μm, the transient stage lacked a delayed onset time as with the previous granular beds. Moreover, the onset time captured remained relatively unchanged with an increase in flow rate. It is noted that the transition process is shortened for beds with larger particles due to the reduced sensitivity to smaller eddies and perturbations.

The onset of the quasi-stable regime is shown in Figure 5.31, a similar trend to that captured in Figure 5.32 is seen. With the reference granular bed comprised of particles of 300 – 400 μm showing initial delayed onset of the quasi-stable stage, at increased flow rates similar asymptotic behaviour is observed for flow rates 51 L/min to 64 L/min. A similar trend is seen for the granular bed comprising of particles of 150 – 300 μm, seen as the delayed onset of quasi-stable stage at 46 L/min. With increased flow rate, onset times remained relatively unchanged, the relative difference between the onset times relative to the reference bed (300 – 400 μm) is reduced. For the largest granular bed of 475 1180 μm, the onset of the quasi-stable stage is relatively stable, noting that at 65 L/min an increased onset time was captured.

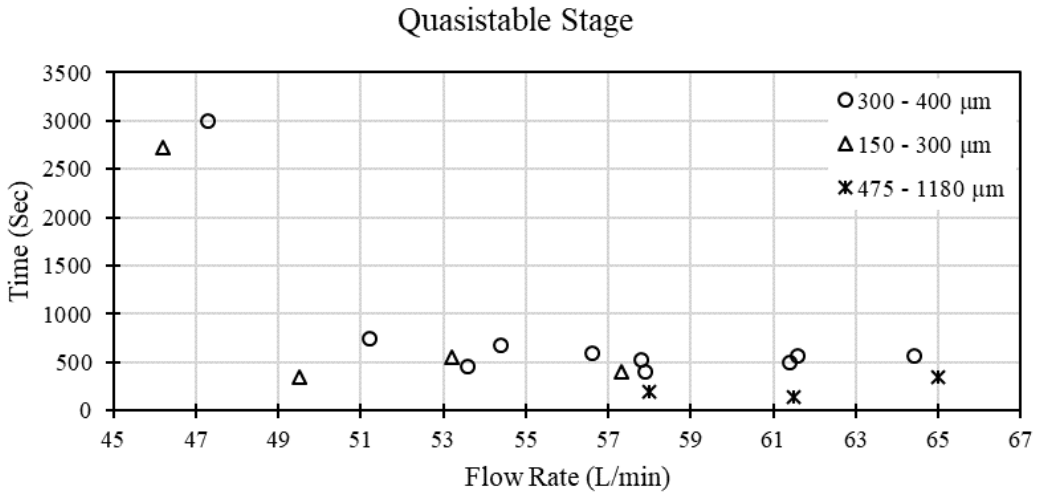

Figure 5.31: *The onset of quasi-stable stage for 150 – 300 μm, 300 – 400 μm and 475 – 1180 μm.*

As discussed the transient stage exhibited the most significant degree of dynamic Fluid-granular interaction. The dynamic interaction, and the associated complex granular bed profiles are seen to be resulting from complex vortex structure interaction with the granular phase. The duration of the transient stage, therefore, is of interest when a comparison of granular bed particle sizes is made. Figure 5.32 shows the duration of the transient stage as the difference between the onset of the quasi-stable stage and the transient stage. For granular bed 300 – 400 μm increased flow rate did not correspond to a shortening in the transient stage.

Moreover, from flow rates 51 L/min to 64 L/min, the duration of the transient stage showed increased scattered from 200 – 550 sec. The smaller granular bed of 150 – 300 μm showed similar behaviour to the reference granular bed, with the duration of the transient stage remaining relatively consistent with increased flow rate. For the granular bed comprising particle of 475 – 1180 μm, an increase in the duration of the transient stage is seen at 65 L/min.

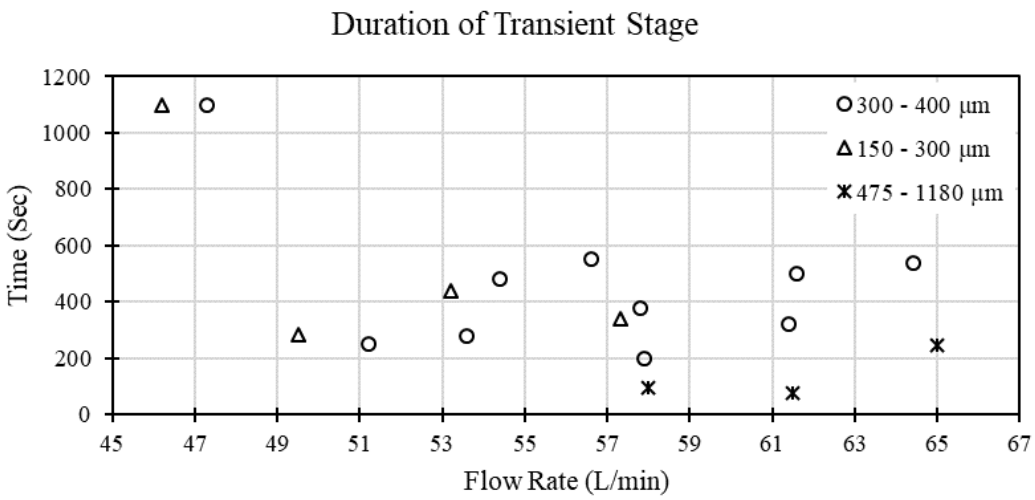

Figure 5.32: *Duration of the transient stage for 150 – 300 μm, 300 – 400 μm and 475 – 1180 μm.*

The scatter captured for transient stage duration suggests that axial flow is not the primary mechanism for the dynamic reshaping of the granular bed during the transient stage. Secondary flow instability, coupled with the stochastic nature of granular materials accounts for the scattered nature of transient stage duration. In contrast, drag force dominated interactions seen for the 475 – 1180 μm granular bed showed a marked difference in temporal behaviour with respect to smaller granular bed particle size ranges. The difference in behavior suggests that the relatively weaker secondary flow effects when compared to axial flow make a more significant contribution to interaction at lower flow rates for granular beds 150 – 300 μm and 300 – 400 μm.

Chapter 6

Multiphase Numerical Modelling

Multiphase flow is typical both in natural processes and industrial systems alike, with systems as diverse as formations of dunes in the desert to fluidised bed reactors in chemical processing plants. Adverse operational conditions such as high pressure and high-temperature environments seen in industrial applications are challenging and costly to replicate and sometimes hard-to-measure under experimental condition[51]. This highlights the importance of validated numerical models that deal with complex multiphase problems. The broad applicability of multiphase models is limited by the increase in complexity of the model relative to those of single-phase systems.

A key feature of multiphase flow is that each phase has an inertial response to interactions with the other phases present in the system. Two commonly employed methods for modelling multiphase flows are the Lagrangian approach and the Eulerian approach. The Lagrangian approach solves Newtonian equations of motion for individual particles, accounting for particle-particle collisions using collision laws to account for the dissipation of energy[52]. The Eulerian approach mathematically represents multiple phases as interpenetrating continua[53], using generalisations of the Navier-Stokes equations for interacting phases. The employment of interpenetrating continua necessitates the concept of phasic volume fraction, which requires that the sum of volume fraction between phases must sum to one. Additionally, conservation equations for each phase must be derived, with the closure of these equations being achieved through empirical information and specifically for the case of solid phases, granular flow kinetic theory, which is an extension of classical kinetic theory of dense flow[52].

The use of Eulerian treatment provides more precise and realistic field information by solving independent momentum equation for each phase, where all phases receive a Eulerian treatment. The complexity of the Eulerian model relative to the VOF (Volume of Fluid) and Mixture models is well documented[53]. A reason for this complexity is the dynamic coupled relationship between the phases being modelled. Each phase requires momentum and continuity equations to be solved with pressure and interphase exchanges coefficients translating interactions between phases.

The numerical method, used for the simulations presented, is explained. Equations and terms pertaining to these results are shown and discussed and the reasoning for the selection and use relative to other available methods.

6.1 Euler-Euler Granular Phase model

Euler-Euler Granular Phase models the granular phase as a pseudo-fluid, properties such as viscosity solid pressure and stress are determined using the kinetic theory of granular flow[54]. The use of Euler-Euler Granular Phase model has shown its utility in modelling processes where high local solid concentrations such as stirred tanks[55] and scour around submerged pipes[56]. This hints at the potential for use in erosion and sedimentation problems, more specifically a system that has complex and dynamic secondary flow effects interactions with a dense solid phase. Conservation of fluid momentum is accounted for using the fluid phase momentum equation (Equation 6.1), with the fluid phase (f), and the solid phases (s) represented.

$$\frac{\delta}{\delta_t}\left(\alpha_f \rho_f \vec{v}_f\right) + \nabla.\left(\alpha_f \rho_f \vec{v}_f \vec{v}_f\right) = -\alpha_f \nabla.p + \nabla.\bar{\bar{\tau}} + \alpha_f \rho_f \vec{g} + k_{fs}\left(\vec{v}_s - \vec{v}_f\right) \quad (6.1)$$

The continuity equation for each phase is represented by Equation 6.2, the secondary phase solution and the stipulation that volume fraction (α) sum to one allows for the primary phase volume fraction to be computed. The assumption of no mass transfer between phases is made, and therefore the right-hand side of the continuity equation is equal to zero.

$$\frac{1}{\rho_{rq}}\left[\frac{\delta}{\delta_t}\left(\alpha_q \rho_q\right) + \nabla.\left(\alpha_q \rho_q \vec{v}_q\right)\right] = 0 \quad (6.2)$$

Interactions between fluid and solid phases are derived based using an analogy based on the kinetic theory of gases, were random particle-particle collisions in the solid phase are treated as a pseudo-thermal phenomenon; with particle collisions treated as inelastic[53]. This adaptation of the kinetic theory of gases captures the effects of internal velocity fluctuations within the solid phase. Internal stresses, viscosity and pressure terms are seen in the Fluid-Solid momentum equation (Equation 6.3).

$$\frac{\delta}{\delta_t}\left(\alpha_s \rho_s \vec{v}_s\right) + \nabla.\left(\alpha_s \rho_s \vec{v}_s \vec{v}_s\right) = -\alpha_s - _s + \nabla.\bar{\bar{\tau}}_s + \alpha_s \rho_s \vec{g} + k_{fs}\left(\vec{v}_f - \vec{v}_s\right) \tag{6.3}$$

6.1.1 Momentum exchange

Momentum exchange between phases is described using the Fluid-Solid Exchange coefficient (k_{fs}). This term is used to couple momentum interfacial exchange between Fluid and solid phases within the Eulerian framework. The majority of drag force models, in a turbulent regime, are empirical closures obtained and valid for particular flow configuration (mostly packed and fluidised beds). Hence, the model applied here is selected using the resolution provided by the literature and accordingly, a brief sensitivity analysis comparing the performance of short-listed closures. The model utilised for determining the Fluid-solid exchange coefficient is the Gibilaro Drag model[57]. The Gibilaro model has been validated against pressure drop experiments using both gas and liquid as fluid phases, with particles arranged in cubical arrays or randomly packed beds. An essential aspect of the Gibilaro Drag model is its utility for a range of flow conditions from laminar to turbulent flow.

$$k_{fs} = \left(\frac{18}{Re} + 0.33\right)\frac{\rho_f \left|v_s - v_f\right|}{d_p}\alpha_s \alpha_f^{-1.8} \tag{6.4}$$

With Reynolds number represented by:

$$Re = \frac{\alpha_f \rho_f d_p \left|v_s - v_f\right|}{\mu_f} \tag{6.5}$$

6.1.2 Lift Coefficient

To account for the vorticity-induced lift present due to the duct curvature, a lift component was included. The Moraga model[58], uses an empirical correlation accounting for tethered submerged spheres in turbulent shear flow, and determined that vortex shedding-induced lateral forces correlated to the product of $Re_p Re_\omega$[58], defined in terms of particle Reynolds number (Re_p) and vorticity Reynolds number (Re_ω)[53]. Lift force ($\vec{F}_{lift}$) is determined using Equation 6.6:

$$\vec{F}_{lift} = -C_l \rho_f \alpha_s \left(\vec{v}_f - \vec{v}_s\right) \times \left(\nabla \times \vec{v}_f\right) \tag{6.6}$$

With (C_l) the lift coefficient with $\varphi = Re_p Re_\omega$:

$$C_l = \begin{Bmatrix} 0.0767 & \varphi \leq 6000 \\ -\left(0.12 - 0.2e^{-\frac{\varphi}{3.6}\times 10^{-5}}\right) e^{-\frac{\varphi}{3}\times 10^{-7}} & 6000 < \varphi > 5 \times 10^7 \\ -0.6353 & \varphi \geq 5 \times 10^7 \end{Bmatrix} \tag{6.7}$$

6.1.3 Turbulence dispersion force

Turbulent dispersion is also modelled using the diffusion in the VOF model, with the governing equation for the volume fraction of the solid phase shown in Equation 6.8, where (γ_f) is the diffusion coefficient for the fluid phase, and $\nabla\left(\gamma_f \nabla \alpha_f\right)$ the turbulence dispersion.

$$\frac{\partial}{\partial_t}\left(\alpha_f \rho_f\right) + \nabla\left(\alpha_f \rho_f \vec{v}_f\right) = \nabla\left(\gamma_f \nabla \alpha_f\right) + S_s \tag{6.8}$$

6.1.4 Solid shear stresses

Momentum exchange due to translation and collision is accounted for using shear viscosity (μ_s), given by Equation 6.9. Collisional viscosity ($\mu_{s,col}$) and kinetic viscosity ($\mu_{s,kin}$) are based on the kinetic theory of granular flow[59]. The viscous-plastic effects of the granular phase at maximum solid volume fraction are captured by the inclusion of friction viscosity (μ_{fr}), with the bulk viscosity (λ_s) modelling of the resistance to compression and expansion of inelastic particles representative of granular material[53, 60].

$$\mu_s = \mu_{s,col} + \mu_{s,kin} + \mu_{fr} + \lambda_s \tag{6.9}$$

Collisional viscosity ($\mu_{s,col}$) and kinetic viscosity ($\mu_{s,kin}$) are modelled using Equation 6.10 and 6.11 respectively and were selected due to their validity for both dilute and dense granular flows[61]:

$$\mu_{s,col} = \frac{4}{5}\alpha_s \rho_s d_s g_{0,ss} \left(1 + e_{ss}\right) \left(\frac{\Theta_s}{\pi}\right)^{1/2} \alpha_s \tag{6.10}$$

$$\mu_{s,kin} = \frac{\rho_s d_s \sqrt{\Theta_s \pi}}{96\alpha_s \left(1 + e_{ss}\right) g_{0,ss}} \left[1 + \frac{4}{5} g_{0,ss} \alpha_s \left(1 + e_{ss}\right)\right]^2 \alpha_s \tag{6.11}$$

For bulk viscosity (λ_s) the Lun et al.[62] expression for bulk viscosity of inelastic particles was used:

$$\lambda_s = \frac{4}{3}\alpha_s^2 \rho_s d_s g_{0,ss} \left(1 + e_{ss}\right) \left(\frac{\Theta_s}{\pi}\right)^{1/2} \tag{6.12}$$

Fictional viscosity (μ_{fr}) is included, allowing for the effects of the dense granular phase reaching its packing limits. Using Scaeffer's expression Equation 6.13[63], with solid pressure (p_s), internal friction angle ($\emptyset$).

$$\mu_{fr} = \frac{p_s sin\emptyset}{2\sqrt{I_{2D}}} \tag{6.13}$$

6.1.5 Granular temperature

A key parameter of the granular phase component of the Euler-Euler Granular Phase model is granular temperature theory. This is an extension of the kinetic theory of gases from the micro-scale to that of the mesoscale and is known as the Kinetic Theory for Granular Flow (KTGF)[62] and accounts for particle-particle interactions. This is a measure of the kinetic energy of random velocity fluctuations of particles in the granular phase. Interaction are fundamentally non-conservative, with energy dissipation due to inelastic deformation of particles and additionally accounts for the dissipation of energy due to fluid-particle interactions. The generation, dissipation and exchange of energy is seen in the transport equation for granular temperature (Equation 6.14). Coefficient of restitution for particle collision (e_{ss}), $g_{0,ss}$ is the radial distribution function, (Θ_s) the granular temperature formally represented by Equation 6.15, and the component of fluctuating solids velocity denoted by ($u_{s,i}$). The granular temperature was solved using the default algebraic formulation which is made possible by the removal of convection and diffusion terms ($k_{\Theta s}\nabla\Theta_s$) from the transport equation (Equation 6.15).

$$\Theta_s = \frac{1}{3}u_{s,i}u_{s,i} \tag{6.14}$$

$$\frac{3}{2}\left[\frac{\partial}{\partial_t}\left(\rho_s\alpha_s\Theta_s\right) + \nabla.\left(\rho_s\alpha_s\vec{v}_s\Theta_s\right)\right] = \left(-\rho_s\bar{\bar{I}}_s + \bar{\bar{\tau}}_s\right) : \nabla\vec{v}_s - \gamma_{\Theta s} + \phi_{fs} \tag{6.15}$$

With solid stress tensor energy generation component of the transport equation:

$$\left(-\rho_s\bar{\bar{I}}_s + \bar{\bar{\tau}}_s\right) : \nabla\vec{v}_s \tag{6.16}$$

Collisional dissipation of energy ($\gamma_{\Theta m}$):

$$\gamma_{\Theta m} = \frac{12\left(1-e_{ss}^2\right)g_{0,ss}}{d_s\sqrt{\pi}}\rho_s\alpha_s^2\Theta^{3/2} \tag{6.17}$$

Energy exchange coefficient:

$$\phi_{fs} = 3k_{fs}\Theta_s \tag{6.18}$$

6.1.6 Fluid Phase Turbulence Model (Mixture Model)

The turbulence model employed was the k-ε mixture model due to its application in phases with separate stratified multiphase flows[53]. This lends itself well to the case being modelled where the granular phase (quartz sand) is separated and eroded by the fluid phase. The constants used in equations 6.19 and 6.20 are the same as the standard k-ε model. Turbulence kinetic energy generation for the mixture model is represented using the term $G_{k,m}$, turbulence kinetic energy generation due to buoyancy effects are neglected, with the constants in the below equation $C_{1\varepsilon}$=1.44, $C_{2\varepsilon}$=1.92

$$\frac{\delta}{\delta_t}\left(\rho_m k\right) + \nabla\left(\rho_m \vec{v}_m k\right) = \nabla.\left(\left(\mu_m + \frac{\mu_{t,m}}{\sigma_k}\right)\nabla k\right) + G_{k,m} - \rho_m \epsilon + \Pi_{k_m} \quad (6.19)$$

$$\frac{\delta}{\delta_t}\left(\rho_m \varepsilon\right) + \nabla\left(\rho_m \vec{v}_m \varepsilon\right) = \nabla.\left(\left(\mu_m + \frac{\mu_{t,m}}{\sigma_\varepsilon}\right)\nabla\varepsilon\right) + \frac{\varepsilon}{k}\left(C_{1\varepsilon}G_{k,m} - C_{2\varepsilon}\rho_m\epsilon\right) + \Pi_{\varepsilon_m} \quad (6.20)$$

Mixing density ($\rho_{m'}$), molecular viscosity ($\mu_{m'}$) and velocity ($\vec{v}_{m'}$) are computed using Equations 6.21, 6.22 and 6.23 respectively, with terms for volume fraction (α_i), density, viscosity and velocity being representative of the iTH phase in the below equations:

$$\rho_m = \sum_{i=1}^{N} \alpha_i \rho_i \quad (6.21)$$

$$\mu_m = \sum_{i=1}^{n} \alpha_i \mu_i \quad (6.22)$$

$$\vec{v}_m = \frac{\sum_{i=1}^{N} \alpha_i \rho_i \vec{v}_i}{\sum_{i=1}^{N} \alpha_i \rho_i} \quad (6.23)$$

6.2 Parallelisation and computational scaling

The Euler-Euler Granular Phase model is known to be a highly unstable model, demanding proper adjustment of discretisation schemes, under-relaxation coefficients and Courant number to achieve convergence. Such settings make the model computationally resource-demanding, requiring parallel computational arrangement to obtain necessary results. For majority of cases modelled the computational time-step is in order of 10^{-6}, representing the number of time steps essential for one minute of real-time results.

Magnus Cray XC40 computer, available to Australian researchers, has been utilised as the computational hardware. The specified case, with final mesh and setting, is tested to find an optimal number of cores. Figure 6.1 representing a brief overview of parallel performance of the model with a varying number of cores.

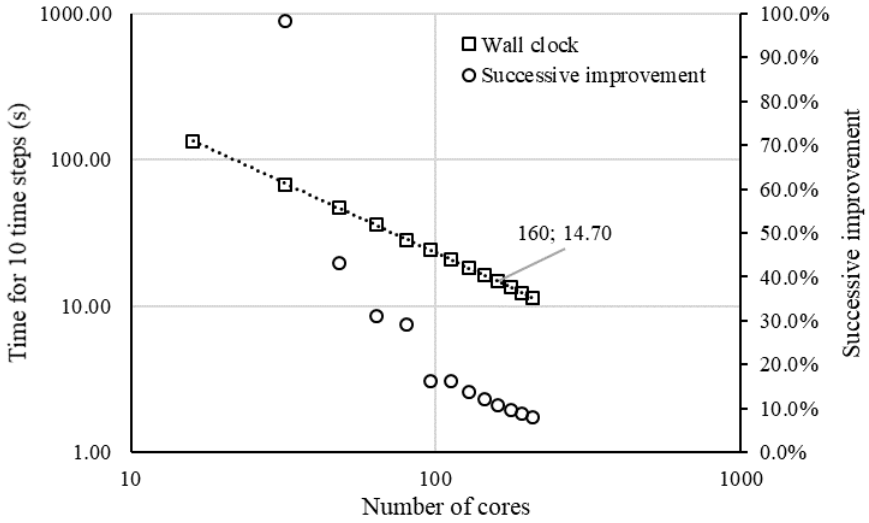

Figure 6.1: *Performance evaluation of scaled cases on a parallel computing platform.*

As the number of cores increases by 16 (cores on each rack) the time required for 10 time steps is recorded and compared. This indicated a logarithmic return in computational speed, represented on the left axis. The successive percentage improvement is assessed by comparing the current required time to the previous step and is represented on the right axis. Accordingly, 160 cores are selected as the optimum number of cores, where beyond which improvement drops below 10%.

6.3 Sensitivity Analysis

A sensitivity analysis is carried out to determine the appropriate drag model and mesh size to be used. Drag model analysis consists of a comparison between three models commonly employed for the current range of granular phase volume fraction, namely, Gibilaro[57], Huilin-Gidaspow[52] and Syamlal-Obrien models[64]. The effects of mesh size is also assessed, and an informed selection is made based on this assessment.

6.3.1 Drag Comparison

The effect of drag model with respect to the granular bed is shown in Figure 6.2. Analysis compares the bed height obtained from the three models 10 second after initiation. The Huilin-Gidaspow model shows the highest rate of granular bed erosion, followed by the Syamlal-Obrien model. The Gibilaro drag model produced the most stable granular bed, with a final granular bed height higher than the other models. Granular bed shape for all three models show similarity; noting that the profile produced using the Gibilaro drag model shows less distinctive profile features.

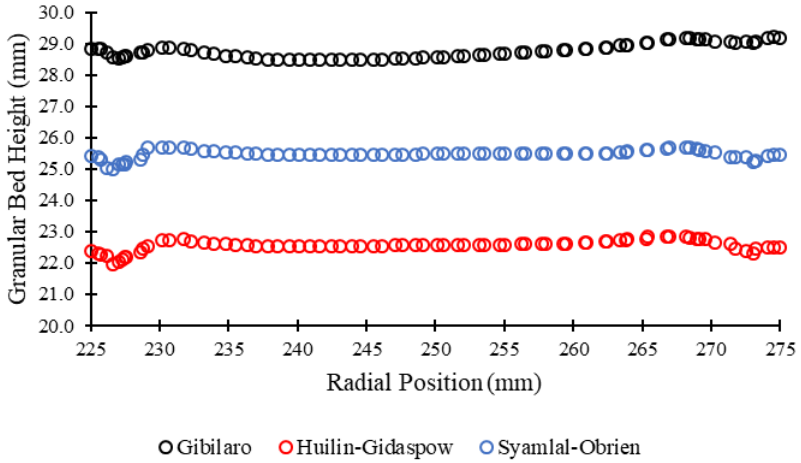

Figure 6.2: *Comparison of granular bed height produced by Gibilaro, Huilin-Gidaspow and Syamlal-Obrien drag models.*

The effects of drag model is also compared with respect to granular phase velocity, shown in Figure 6.3. This is done to ensure spurious velocity a well-known numerical issue in multi-phase models, is not experienced at the interface. All three drag models show similar predictions of granular phase velocity, with the Gibilaro and Huilin-Gidaspow models showing the highest granular phase velocities respectively. The observed velocity profiles match the boundary values, defined for each phase, and hence are physically meaningful.

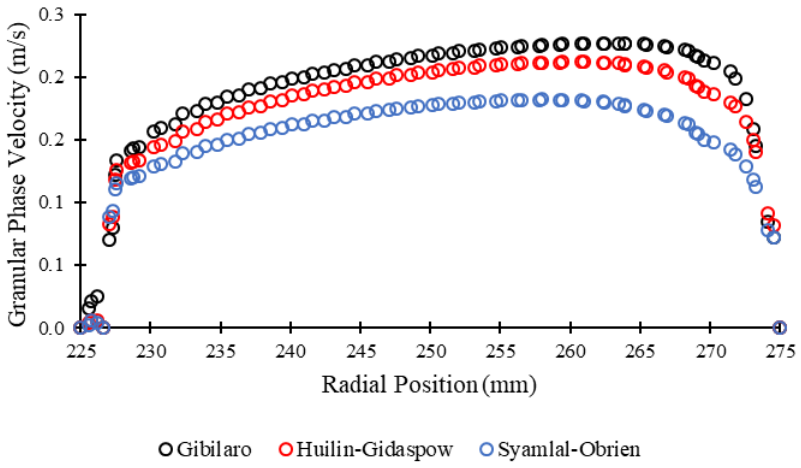

Figure 6.3: *Comparison of granular phase velocity produced by Gibilaro, Huilin-Gidaspow and Syamlal-Obrien drag models.*

Selection of the Gibilaro drag model is made based on a comparison between experimental observations and the sensitivity analysis. The greater rate of erosion captured for Huilin-Gidaspow and Syamlal-Obrien models eludes to potential discrepancies between numerical and experimental results. The effect of drag model selection with respect to granular phase velocity is seen to be of secondary concern, with all three models showing similar velocities across the duct cross-section.

6.3.2 Mesh Sensitivity

Selection of appropriate mesh size is based on a mesh size sensitivity analysis shown in Figure 6.4. The effects of mesh size on granular bed height has been examined for mesh sizes 2 mm, 1.5 mm and 1 mm using the Gibilaro drag model. The resulting analysis suggests that for mesh sizes 2 mm and 1.5 mm; there is no significant difference in granular bed height whereas for a mesh size of 1 mm significant changes in granular bed height is observed. This suggest mesh size resolution of 1 mm could be considered as the optimised mesh size beyond which the excessive computational requirements do not offer much improvements in the numerical accuracy.

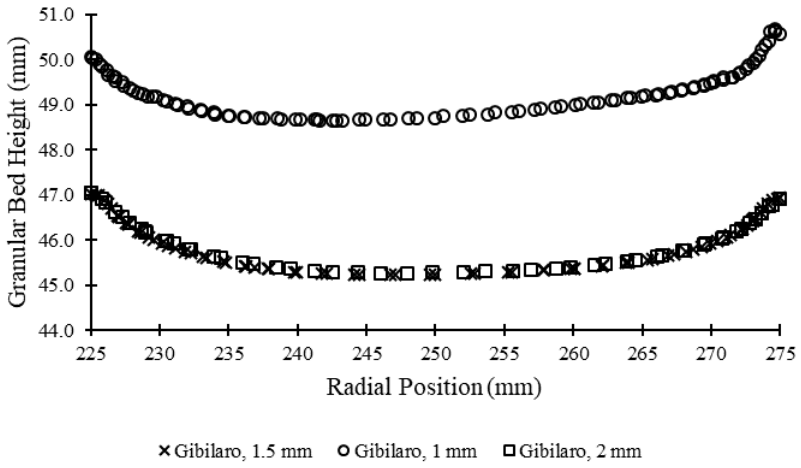

Figure 6.4: *Mesh sensitivity of Gibilaro drag model, with respect to granular bed height.*

Chapter 7

Numerical Results and Discussion

Numerical results obtained using a Euler-Euler Granular Phase model are presented in this section. Granular beds of grain size ranges 150 – 300 μm, 300 – 400 μm and 475 – 1180 μm with Flow rates of 45 L/min, 50 L/min, and 55 L/min are investigated. A fixed cross-section at 135° is selected for spatial and temporal investigation of fluid-granular interactions, with comparison made between the standard and modified Gibilaro drag model. Representation of the granular phase is made using the volume fraction (VOF) of the granular phase. The interface between the granular bed and fluid phase is indicated by a solid black line and represents a granular bed VOF value of 0.5. Secondary flow instability is represented using normalised helicity function (H) allowing for the position and direction of rotation of vortex structures to be captured.

To enable comparison across numerical results dimensionless helicity (H^*) is used, with clockwise and counter-clockwise rotation represented by solid blue and solid red lines respectively. To eliminate spurious helical flow structures, a threshold is applied to dimensionless helicity exclude values between $-0.01 \geq H^* \leq 0.01$.

7.1 Overview of the flow field

An overview of the flow field and fluid-granular interactions are provided in this section. The overview presented provides a general illustration of self-induced acceleration in the flow field exposed to curvature. This is seen by the formation of counter-rotating vortex cores. Additionally, the mutual influence of these structure on the granular bed is captured.

7.1.1 Vortex core formations

Figure 7.1 shows the presence and pattern of counter-rotating vortex cores in the curved passage interacting with the granular phase during the initial stages of interaction (t = 20 sec), where direction of flow is indicated by the black arrow. Vortex core rotation direction are denoted by using red (clockwise) and blue (counter-clockwise) rotation. The presence of vortex cores can be seen in Figure 7.1 located at the outer-wall and at the fluid passage upper-face.

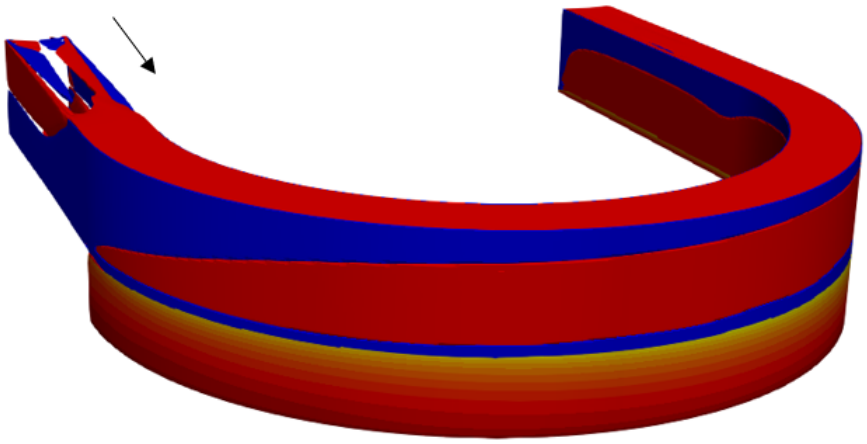

Figure 7.1: *Flow overview of vortex cores in the curved duct for a flow rate of 55 L/min.*

7.1.2 Fluid-granular Interactions

As captured in experimental results (Section 4.1), the results of fluid-granular interaction are seen by the formation of bed structures across and along the granular bed. A qualitatively consistent result of flow field interaction with the granular bed was the formation of migrating inner-wall dunes. An overview of numerical results showing such interaction is shown in Figure 7.2, 7.3 and 7.4 for time steps t = 20, 30, 40 sec respectively. The granular bed interface is selected based on a granular phase VOF = 0.5, with both the colour map and contour lines denoting the vertical height of the deformed granular beds, therefore allowing for the identification of granular bed features.

Interactions captured at t = 20 sec (Figure 7.2), shows the initial stages of fluid-granular interaction. Dune formations are seen along the inlet and outlet halves of the curved passage. With erosion occurring at the inlet half of the curved passage and sedimentation being dominate on the outer half.

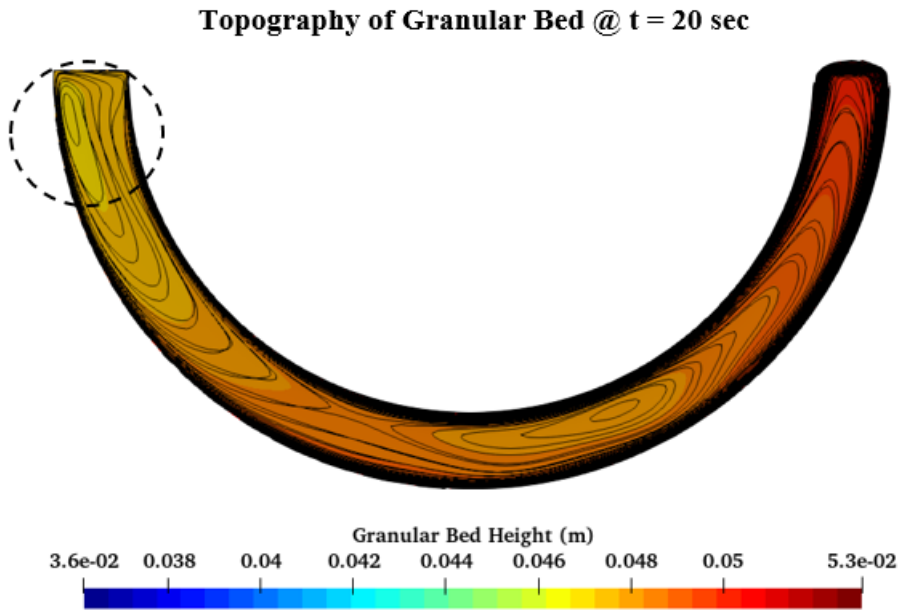

Figure 7.2: *Topographical overview of granular bed height for a flow rate of 55 L/min at t = 20 sec.*

At t = 30 sec, numerical results show a clear indication of the presence of inner-wall dunes captured in experimental results (Section 4.1.1, Figures 4.1a, 4.1b). Inner-wall dunes are migrating in the direction of the outlet half of the curved passage, with an inward inclination of dune formations captured. Additionally, similarity to the inner-wall ridge described in Section 4.1.4 Figure 4.3 is captured at 25° – 70° along with the curved passage location.

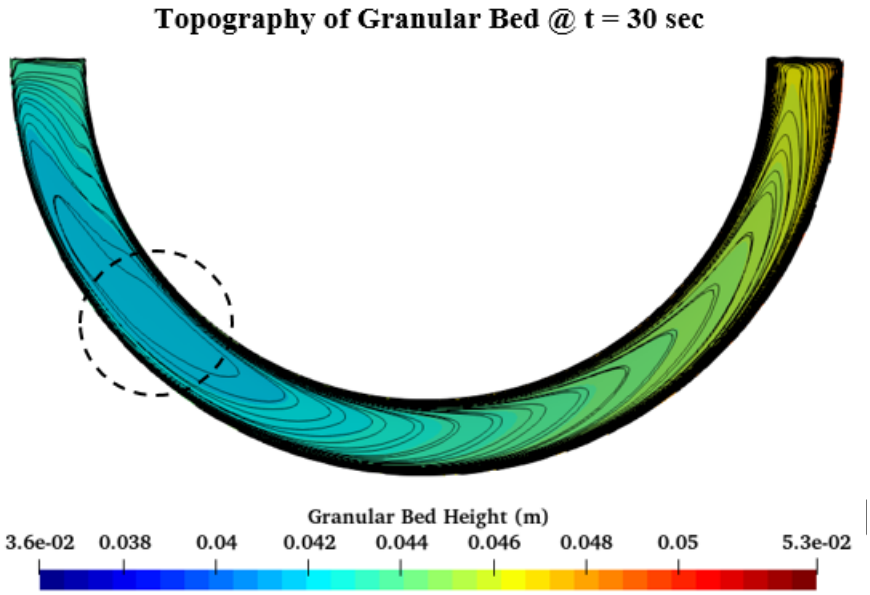

Figure 7.3: *Topographical overview of granular bed height for a flow rate of 55 L/min at t = 30 sec.*

With the progress of time and decreased granular bed height, a change in bed profile is captured in Fig 7.4. Numerical results show the continued presence of inner-wall dune structures located from 100° – 165° along the curved passage. With the remainder of the granular bed showing a relatively flat bed profile.

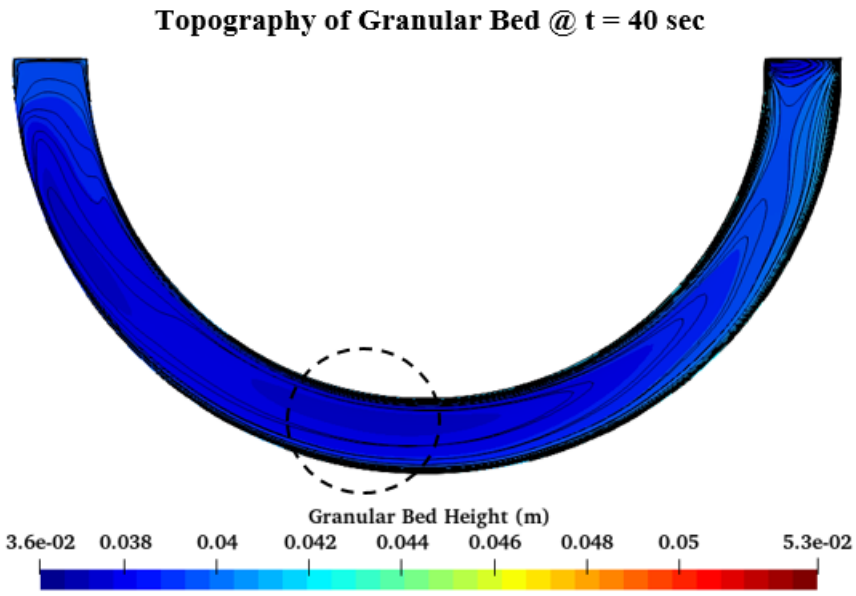

Figure 7.4: *Topographical overview of granular bed height for a flow rate of 55 L/min at t = 40 sec.*

Numerical results shown in Figure 7.2, 7.3, and 7.4 show qualitative agreement with the initial stages of fluid-granular interactions captured in experimental results. The transition from initial bed deformation which creates the larger dune structures and eventual oscillatory behaviour in granular bed height is absent, with bed features captured from numerical results showing little difference in height relative to the average granular bed height.

7.2 Spatial and Temporal Investigation

This section provides both a spatial and temporal overview of numerical results. A spatial investigation is presented with cross-sectional views of the flow field representing dimensionless helicity (H*) and the VOF with respect to the granular phase at discrete time steps. Temporal overviews are subsequently presented to show the complete temporal evolution of the bed (at four key measurement points), for the respective case. The points of investigation, presented for a temporal overview, are selected to align with those of experimental results namely, Point 1 (outer-wall), Point 2, Point 3 and Point 4 (inner-wall).

Numerical cases simulate the process for three granular bed size ranges, 150 – 300 μm, 300 – 400 μm and 475 – 1180 μm. Parametric analysis is also carried out for flow rates of 45 L/min, 50 L/min, and 55 L/min. Finally, modified drag coefficient cases are examined to investigate sensitivity of the erosion rate to this critical coupling scheme.

7.2.1 Case-1: D=150 – 300 μm, Q=55 L/min

Numerical results obtained for the Case-1 captured the formation of helical structures, with the effects of a closed duct on the flow field supported by the presence of strong counter-clockwise helicity located at the top duct cross-section. The presence of counter-rotating vortex pairs is captured with the most prominent formation seen at t = 50 sec and t = 60 sec. It is noted that the formation of counter-rotating vortex structures is seen to form away from the granular bed interface, demarcated by the solid black line. When a comparison is made to the VOF cross-sections, the diffused granular phase is seen influencing the flow structure of the fluid phase, with vortices forming above the diffused granular phase.

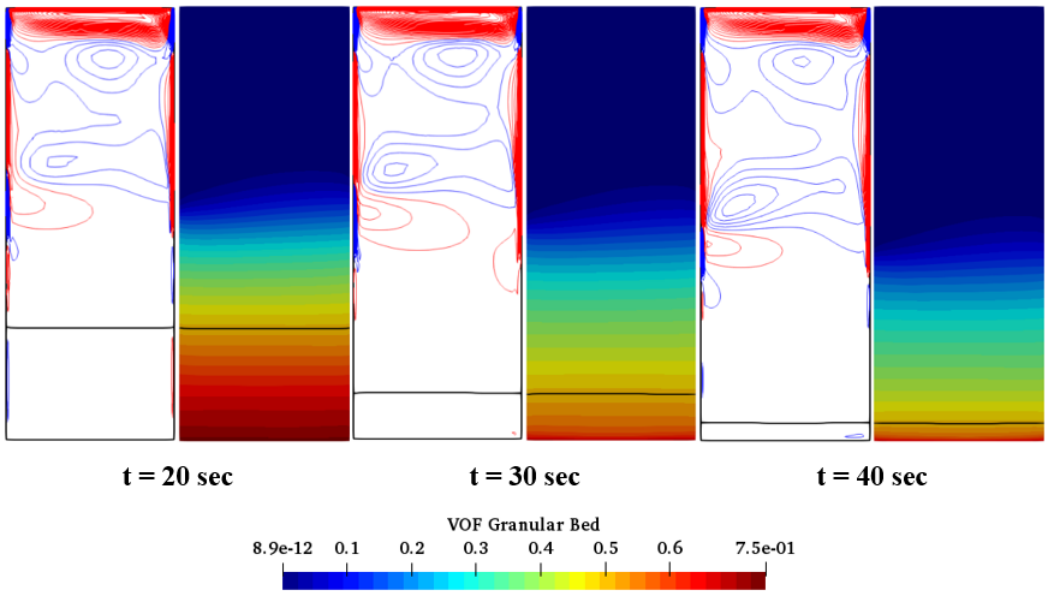

Figure 7.5: *Spatial overview of 135° position, showing H* and granular phase VOF respectively for case Case-1 over t = 20 – 40 sec.*

The diffuse nature of the granular phase shown in Figure 7.5 and 7.6 for numerical case Case-1 results in increasingly dilute granular bed over time. The diffusive nature of the granular bed is seen to undergo rapid erosion, with the granular bed almost completely eroded within 40 sec and can be considered completely eroded at t = 50 and 60 sec. When a comparison is made to experimental results under similar parameters, numerical results diverge from experimental observation both qualitatively and quantitatively.

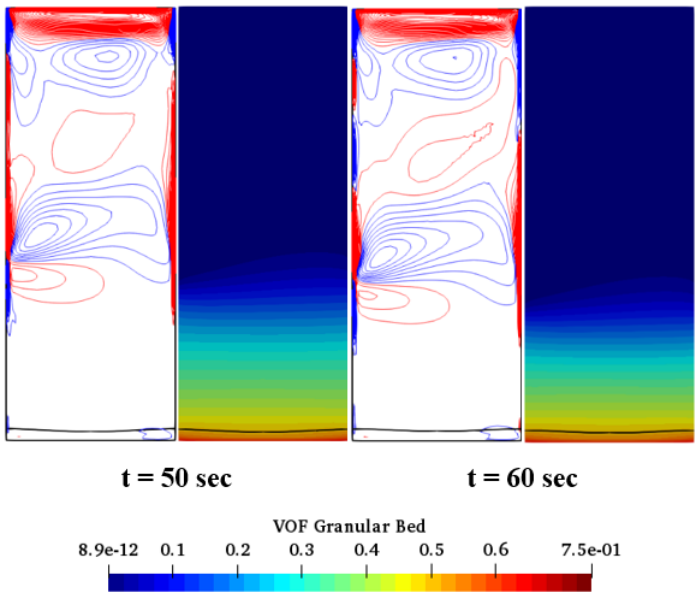

Figure 7.6: *Spatial overview of 135° position, showing H* and granular phase VOF respectively for Case-1 over t = 50 – 60 sec.*

A temporal plot of Case-1 is shown in Figure 7.7. The effect of the dispersed interface on the erosion rate can be seen by the rapid and removal of the granular bed over 60 sec. Temporal results, indicate the granular bed rapidly eroding and entering the quasi-stable stage at t ≈ 45 sec. Fluid-granular interactions captured for Case-1 also show an absence of oscillatory behaviour in granular bed height, present in experimental results. The diffuse nature of the granular phase and the subsequent effect on helical flow structure may be responsible for both the lack of oscillatory behaviour and the rapid erosion of the granular bed.

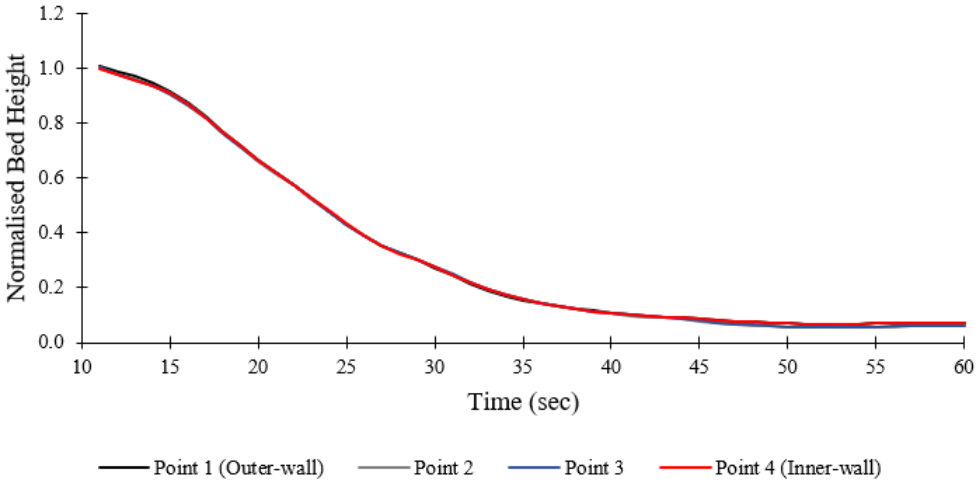

Figure 7.7: *Temporal overview of 135° position for numerical Case-1, showing the normalised granular bed height with respect to time.*

7.2.2 Case-2: D=300 – 400 μm, Q=45 L/min

For the numerical Case-2, the presence of counter-rotating vortex structures and the expected concentration of helicity at the top of the duct is captured. Numerical results show a less diffuse granular bed when compared to that of Case-1 (Figure 7.5 and 7.6). Consequently, vortex structures are located closer to the fluid-granular interface. The presence of counter-rotating vortex pair at the outer-wall and the granular bed interface is seen to develop as the granular bed is eroded across each time step.

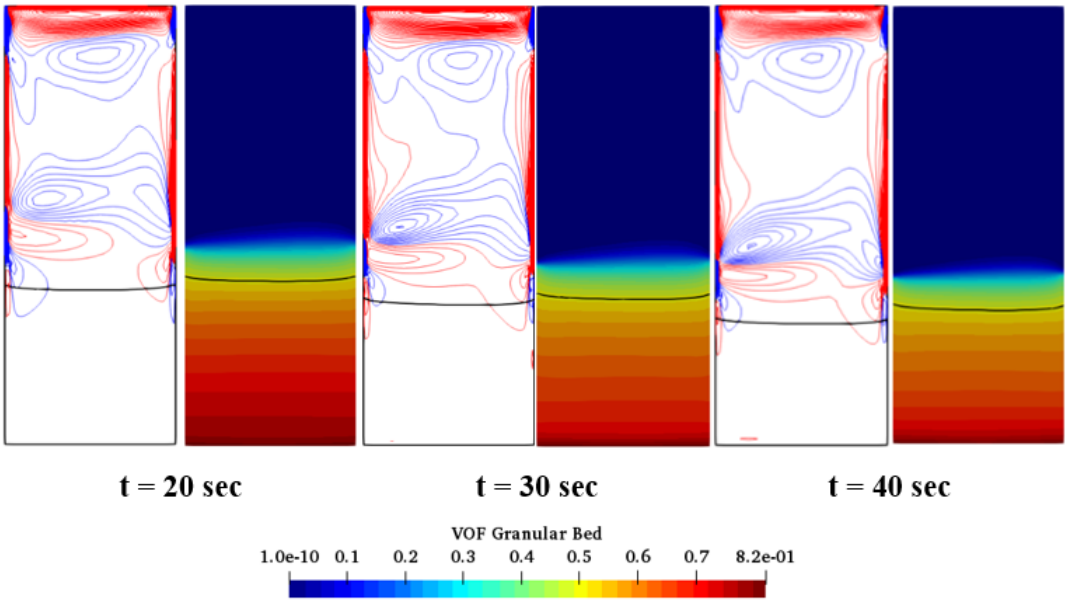

Figure 7.8: *Spatial overview of 135° position, showing H* and granular phase VOF respectively for Case-2 over t = 20 – 40 sec.*

The granular interface, captured in Figure 7.5 and 7.6, lacks the complex granular bed profiles captured in experimental results, with relatively uniform erosion according across the granular bed width. The rate of granular bed erosion is seen to decay, for time steps t = 50 sec and t = 60 sec with the vortex structure showing similar stability.

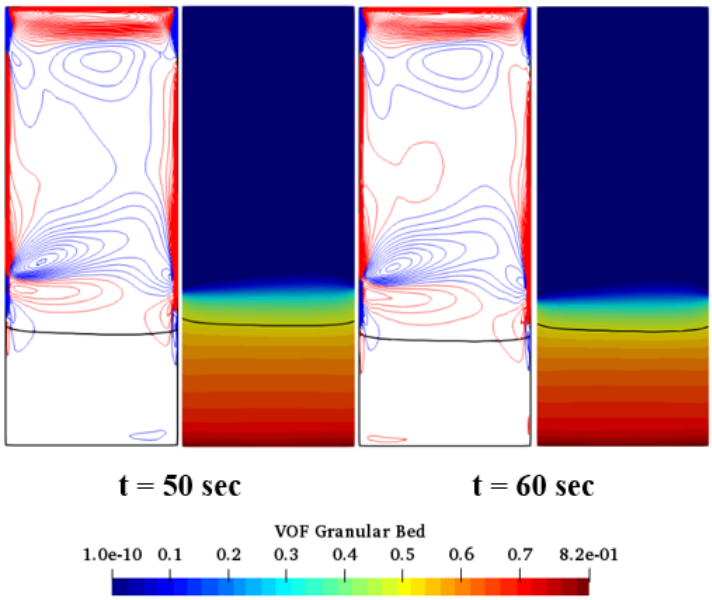

Figure 7.9: *Spatial overview of 135° position, showing H* and granular phase VOF respectively for case Case-2 over t = 50 – 60 sec.*

The temporal overview shown in Fig 7.10 , as captured in the spatial overview, a less diffused interface is observed for a granular bed comprising grains of 300 – 400 μm. A temporal overview shows a greatly reduced erosion rate when compared to the Case-1. The granular bed can be seen to momentarily increase and stabilise at t = 20 sec, after which the general trend of erosion continues. Granular bed height is seen trending towards stable fluid-granular interactions corresponding to the quasi-stable stage.

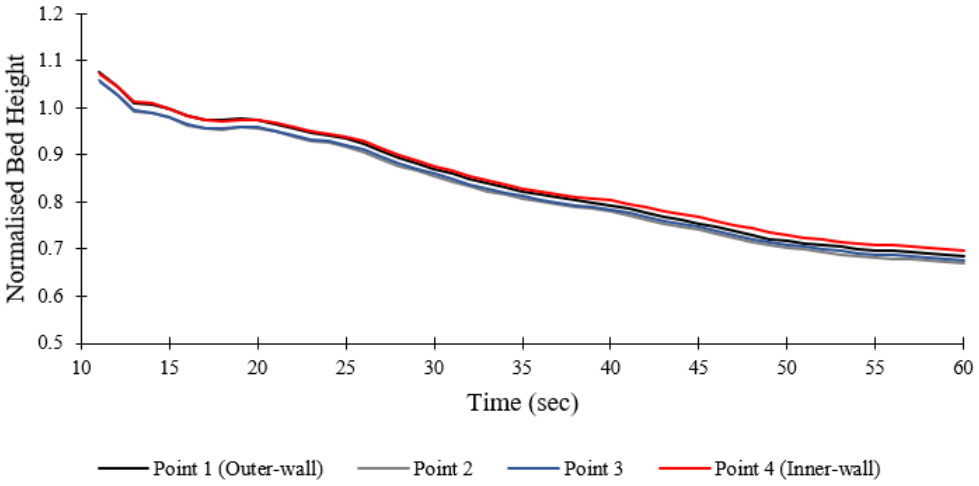

Figure 7.10: *Temporal overview of 135° position for numerical case Case-2, showing the normalised granular bed height with respect to time.*

7.2.3 Case-3: D=300 – 400 μm, Q=50 L/min

At an increased flow rate of 50 L/min, numerical results show similar behaviour to that of Case-2. Similar to the previous numerical case, the granular phase is eroded over a shorter temporal scale than that of the corresponding experimental results. Counter-rotating vortices seen at the outer-wall located near the fluid-granular interface, noting the influence the diffused granular phase has on the proximity of these vortices to the granular bed interface demarcated by the solid black line.

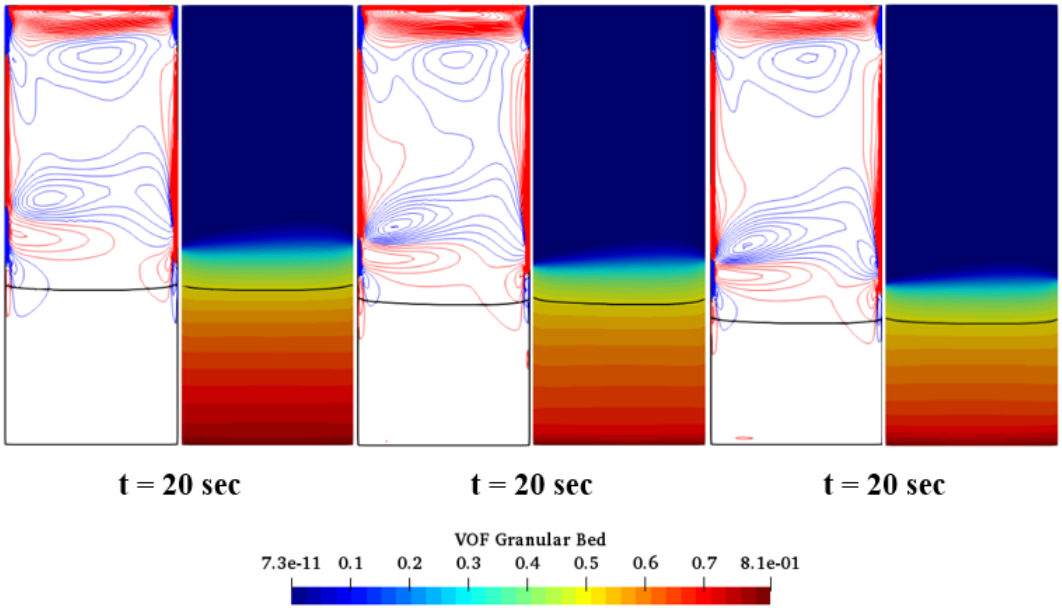

Figure 7.11: *Spatial overview of 135° position, showing H* and granular phase VOF respectively for Case-3 over t = 20 – 40 sec.*

Similar to numerical Case-2, the granular interface, seen in Figure 7.12, lacks the complex granular bed profiles captured in experimental results. Additionally, stabilisation of the flow field is captured for time steps t = 50 sec and t = 60 sec, with vortex structures above the granular bed occupying a similar position over this period.

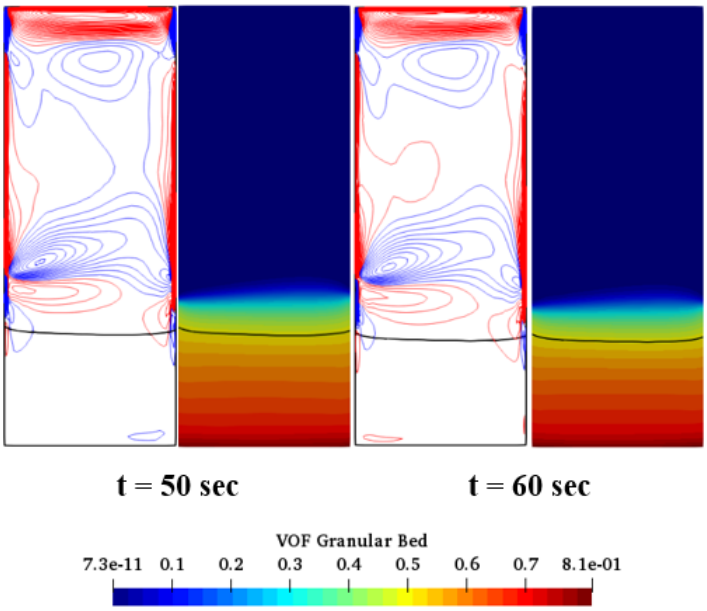

Figure 7.12: *Spatial overview of 135° position, showing H* and granular phase VOF respectively for case Case-3 over t = 50 – 60 sec.*

Similar temporal behaviour to Case-2 is observed at an increased flow rate of 50 L/min, shown in Figure 7.13. An increased flow rate is seen to produce more pronounced granular bed height fluctuations relative to case Case-2. The most prominent occurring at t ≈ 22 sec with a less pronounced increase in granular bed height occurring at t ≈ 45 sec. As with case Case-2, Case-3 lacks clearly defined stages of interaction captured by experimental results but shows a similar trend towards a quasi-stable stage of fluid-granular interaction.

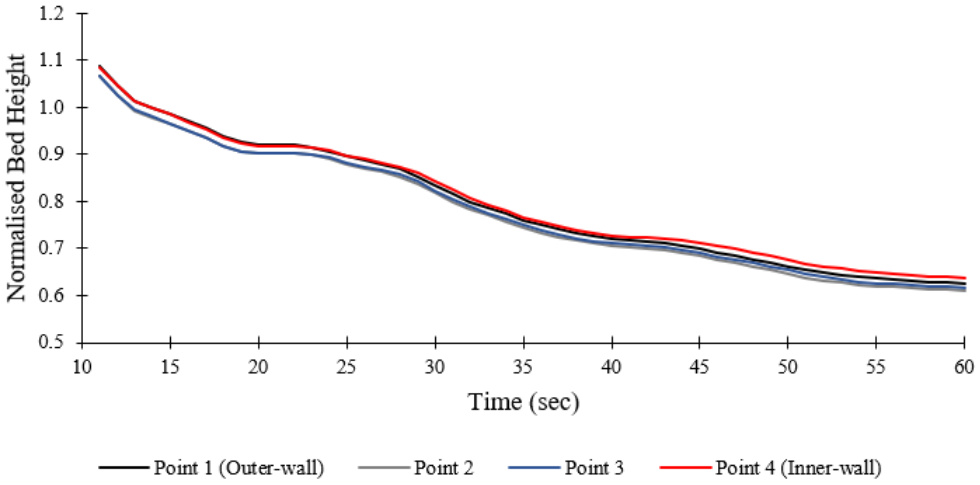

Figure 7.13: *Temporal overview of 135° position for numerical case Case-3, showing the normalised granular bed height with respect to time.*

7.2.4 Case-4: D=300 – 400 μm, Q=55 L/min

For a flow rate of 55 L/min, similar Fluid-granular interaction behaviour is captured to that of Case-2 and Case-3. The position of counter-rotating vortex pairs at the outer-wall and above the fluid-granular interface as with previous cases is shown to track the eroded bed. Furthermore, at a flow rate of 55 L/min, the effects of the diffused interface are still present, with vortex structures seen to be displaced away from the granular bed interface by the dispersed granular phase.

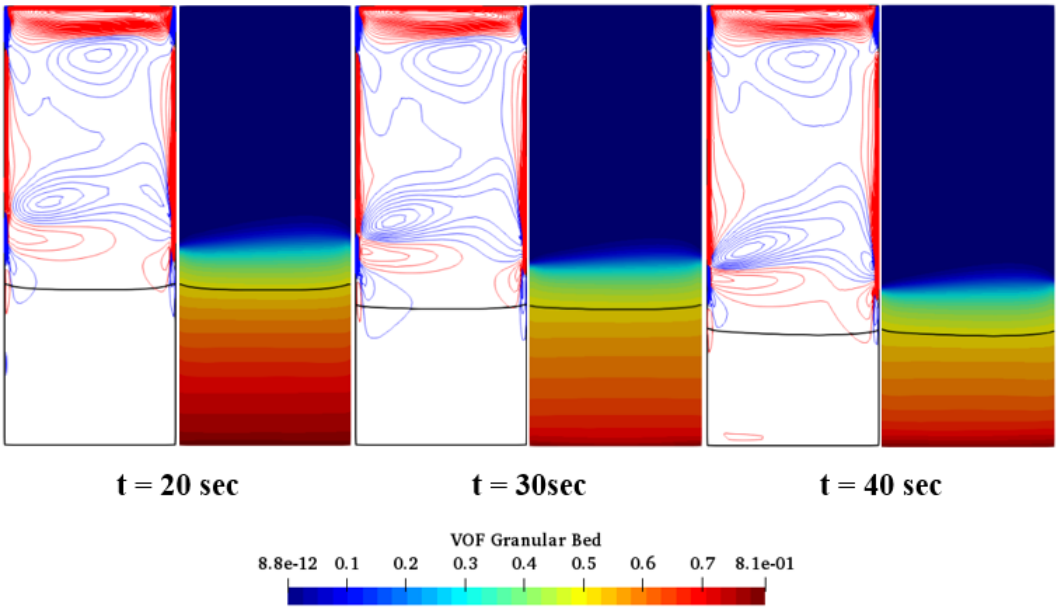

Figure 7.14: *Spatial overview of 135° position, showing H* and granular phase VOF respectively for Case-3 over t = 20 – 40 sec.*

The granular interface, seen in Figure 7.14, lacks the complex granular bed profiles captured in experimental results. Additionally, stabilisation of the flow field is captured for time steps t = 50 sec and t = 60 sec, with vortex structures above the granular bed occupying a similar position over this period.

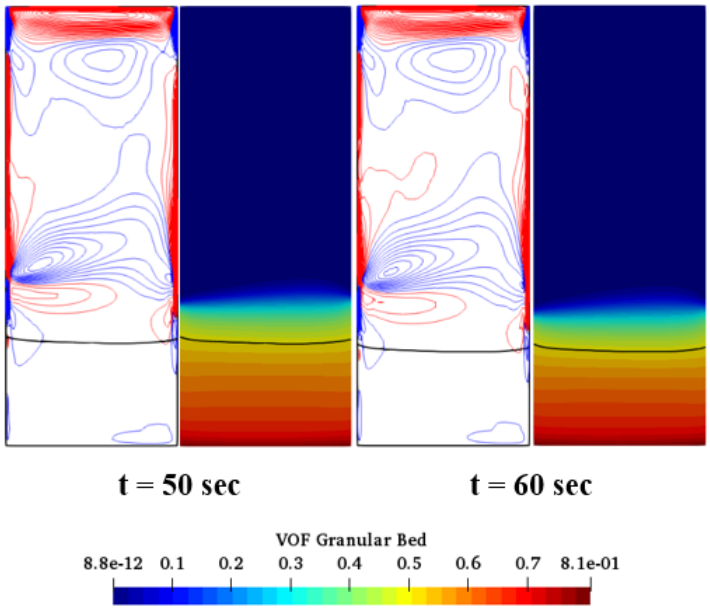

Figure 7.15: *Spatial overview of 135° position, showing H* and granular phase VOF respectively for case Case-3 over t = 50 – 60 sec.*

Similar temporal behaviour to Case-2 and Case-3 is observed at an increased flow rate of 50 L/min. An increased flow rate is seen to produce more pronounced granular bed height fluctuations. The most prominent occurring at t ≈ 22 sec with a less pronounced increase occurring at t ≈ 45 sec. As with Case-2, Case-3 and case-4 lacks clearly defined stages of interaction captured by experimental results but shows a similar trend towards a quasi-stable stage of fluid-granular interaction.

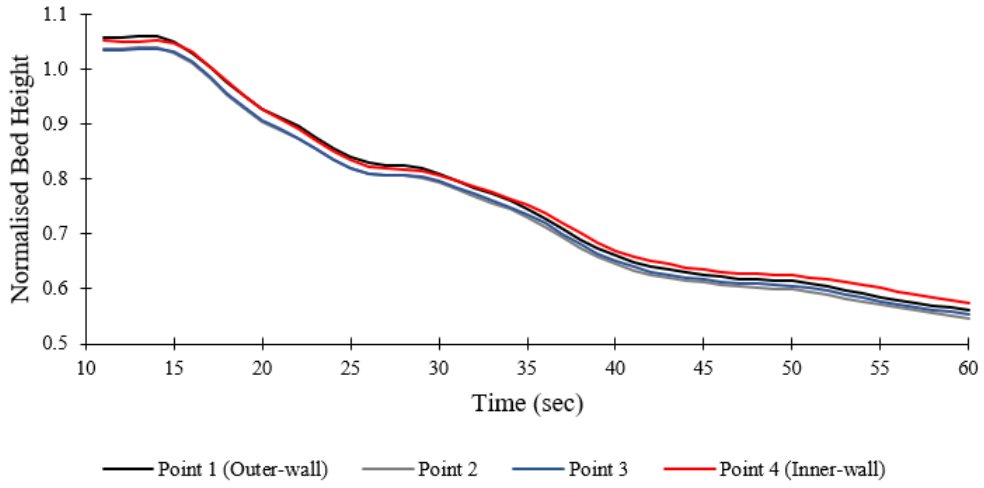

Figure 7.16: *Temporal overview of 135° position for numerical case Case-3, showing the normalised granular bed height with respect to time.*

7.2.5 Case-5: D=475 – 1180 μm, Q=55L/min

Numerical results for the coarsest granular bed comprising of 425 – 1140 μm grains, are shown for a flow rate of 55 L/min in Figure 7.17 and 7.18. Numerical results show less dispersed granular phase and a more pronounced granular bed profile relative to all the previous cases. A less diffuse granular phase is seen resulting in the formation of counter-rotating vortex structures closer to granular bed interface demarcated. The resulting proximately of counter-rotating vortices to the granular bed interface is seen as an uneven granular bed profile.

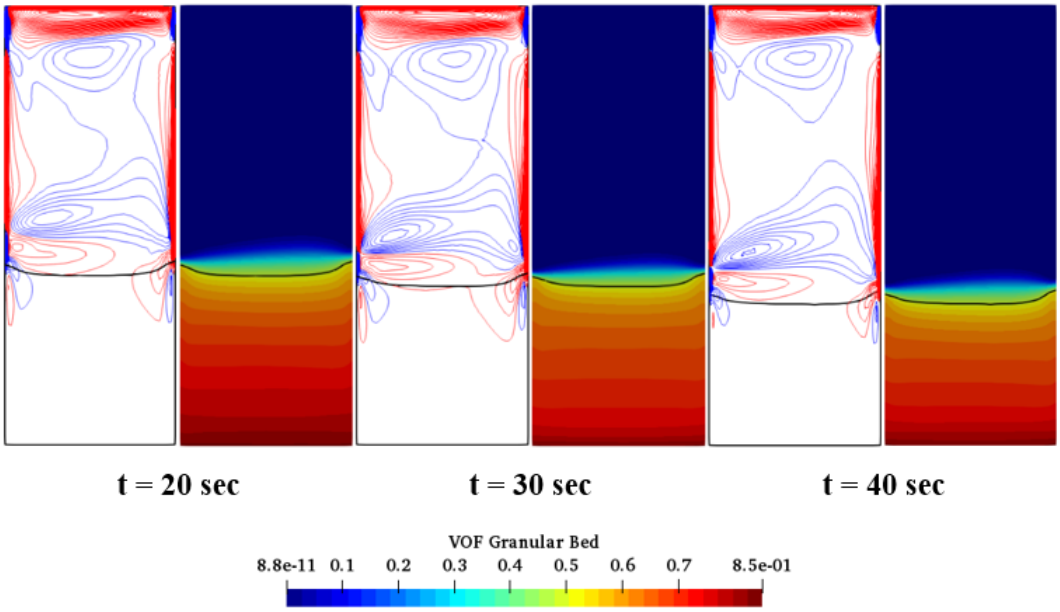

Figure 7.17: *Spatial overview of 135° position, showing H* and granular phase VOF respectively for Case-5 over t = 20 – 40 sec.*

Comparison to the experimental results for the same granular bed size range and flow condition show a lack of similarity in granular bed profile. Numerical results for Case-5 show the result of fluid-granular interaction to be erosion dominant, in contrast to experimental observation. Experimental results under the same parameters showed sustained sedimentation across the duct.

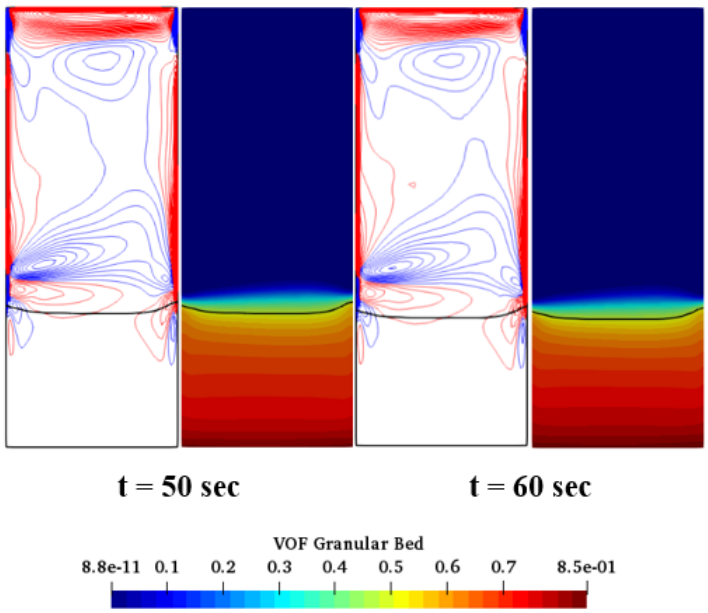

Figure 7.18: *Spatial overview of 135° position, showing H* and granular phase VOF respectively for case Case-3 over t = 50 – 60 sec.*

Temporal results are shown in Figure 7.19 for case Case-5. A stable initial granular bed profile is captured, showing qualitative similarity to the initially captured in experimental behaviour, noting that a granular bed profile has already taken form during this process unlike that seen in experimental results. After the initial stages of interaction, numerical and experiment results diverge. Experimental temporal results show initial stable stage to be followed by a rapid transition into sedimentation dominated interaction, as can be seen in Figure 7.19 below, the general trend of interaction is seen to be one of gradual erosion.

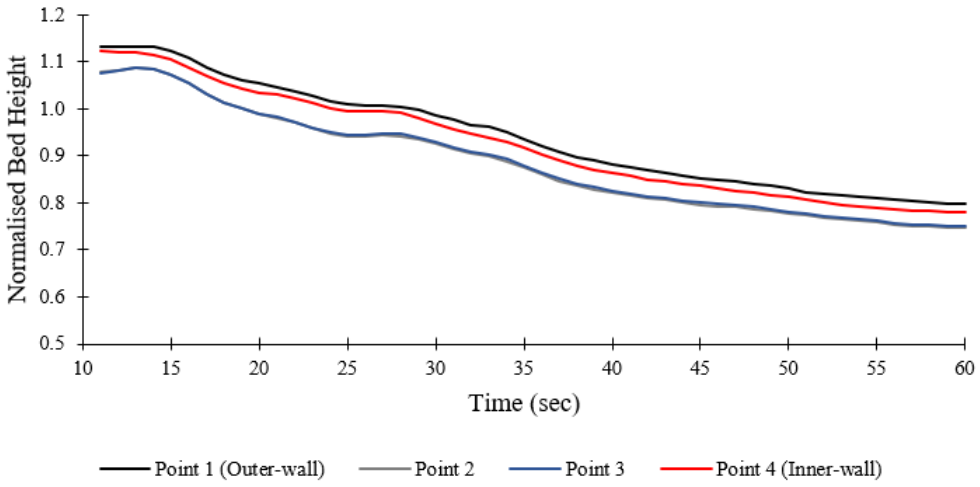

Figure 7.19: *Temporal overview of 135° position for numerical case Case-5, showing the normalised granular bed height with respect to time.*

7.3 Modified Gibilaro Drag model

Selection of the standard Gibilaro Drag model is based on the sensitivity analysis undertaken in Section 6.3. Numerical results show erosion of the granular bed at a rate higher than that of experimental results. To examine the discrepancy between experimental and numerical results, a modified Gibilaro Drag model is used by manual selection of a drag coefficient. Time steps selected for spatial investigation accounted for the extended nature of the numerical results presented. Complete temporal overviews are provided for each case for increased temporal resolution. The case of D=300 – 400 μm, is examined when drag correction coefficient is scaled by factor of 0.5 for two flow rates of 50 L/min and 55 L/min. This test is critical to understand the numerical contribution of drag coefficient in the erosion rate and weight it against other numerical parameters such as mesh refinement, adjustment of Courant number and closures which are likely to improve qualitative accuracy of the model.

7.3.1 Case-6; Q=50 L/min, Correction factor=0.5

Numerical results associated with the lowest correction factor for a granular bed of size 300 – 400 μm, at a flow rate of 50 L/min is shown in Figure 7.20 and 7.21 and 7.22. When a comparison is made to Case-3 which uses no drag correction, VOF interface diffusion is seen to be reduced. Additionally, the effect of drag coefficient modification is seen by a decrease in erosion rate and a varied granular bed profile, demarcated by the solid black line.

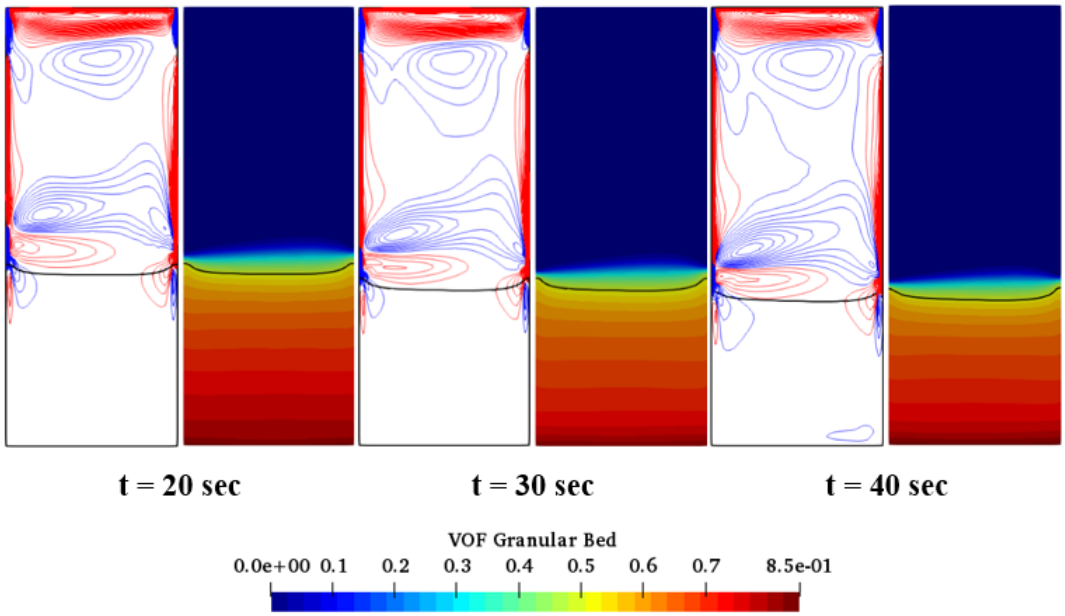

Figure 7.20: *Spatial overview of 135° position, showing H* and granular phase VOF respectively correction factor = 0.5 over t = 20 – 40 sec.*

A less diffuse interface is seen, resulting in the formation of counter-rotating vortex structures closer to the granular bed interface. The product of counter-rotating vortices proximately to the granular bed interface is an uneven granular bed profile. A distinctive difference between the granular bed profile shape is captured as a result of incorporating the correction factor.

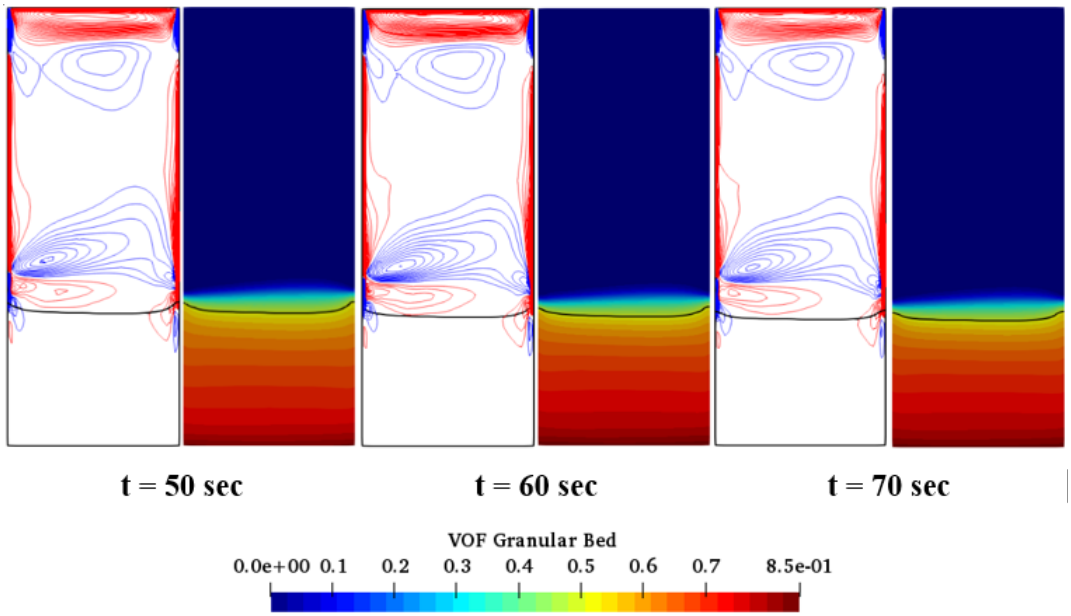

Figure 7.21: *Spatial overview of 135° position, showing H* and granular phase VOF respectively correction factor = 0.5 over t = 50 – 70 sec.*

Granular bed height over t = 20 – 40 sec (Figure 7.20) compared to that of the granular bed height of t = 50 – 70 sec (Figure 7.21), shows a reduction in the rate of granular bed erosion. The onset of the quasi-stable phase from t = 70 – 200 sec is captured, with the stabilisation of fluid-granular interactions typifying the quasi-stable phase is seen in Figure 7.22.

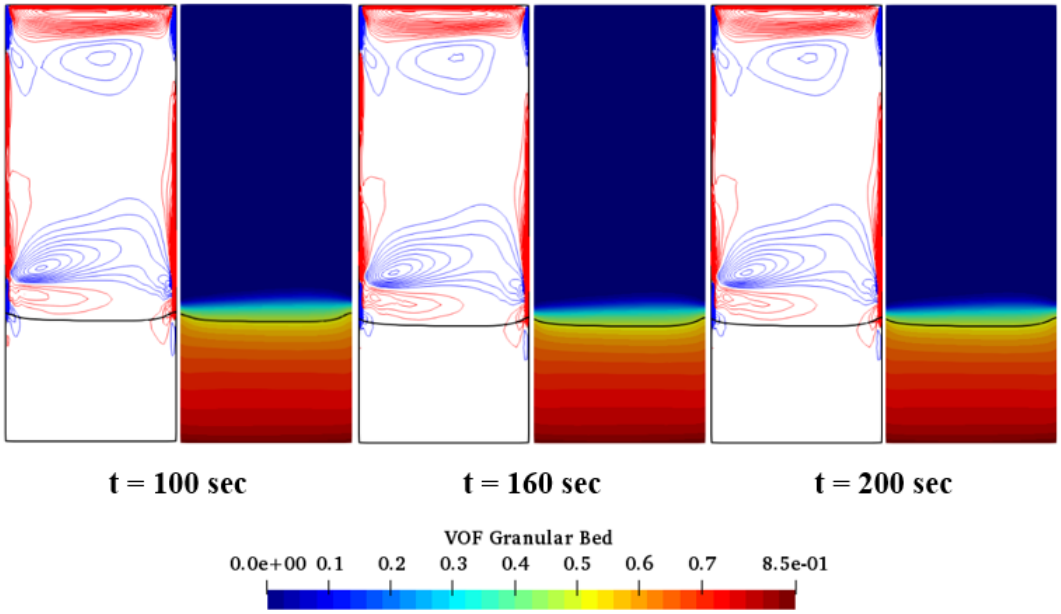

Figure 7.22: *Spatial overview of 135° position, showing H* and granular phase VOF respectively over t = 100 – 200 sec.*

Temporal analysis for the modified case is shown in Figure 7.23, the increased temporal scale captured shows qualitative similarity to experimental results under the same parameters (300 – 400 μm, flow rate 50 L/min). Specifically, the quasi-stable phase of fluid-granular interactions is captured with interactions stabilising at t = 140 sec. Temporal scales for the transition into the quasi-stable phase between numerical and experimental results differ, with fluid-granular interactions stabilising earlier for numerical results. Additionally, a reduced transitional phase is seen to occur to t = 10 – 60 sec.

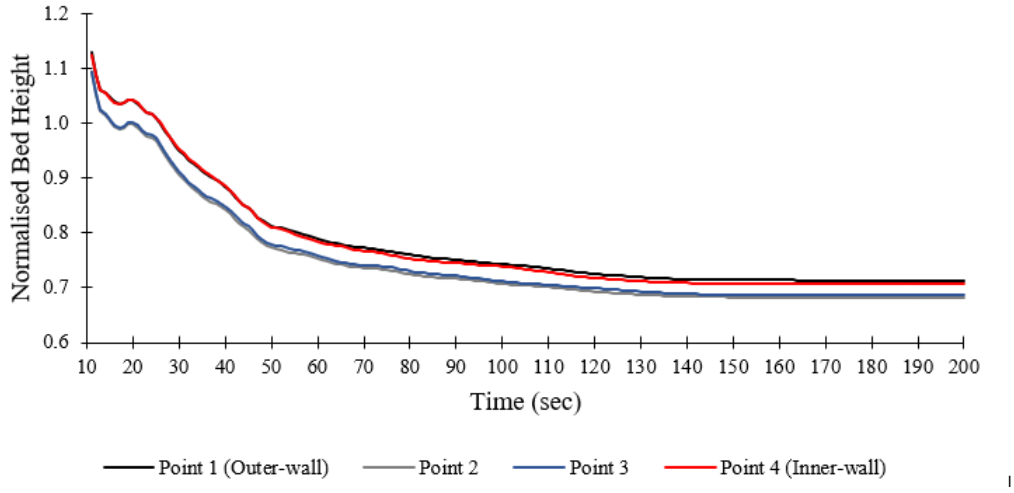

Figure 7.23: *Temporal overview of 135° position, showing the normalised granular bed height with respect to time.*

7.3.2 Case-7; Q=55 L/min, Correction factor=0.5

Numerical results for the drag correction factor of 0.5 at an increased flow rate of 55 L/min are shown in Figures 7.24 and 7.25. Comparison of results obtained for case Case-4 using the standard Gibilaro Drag model to those of the modified case shows a less diffuse granular phase, and a corresponding decrease erosion rate.

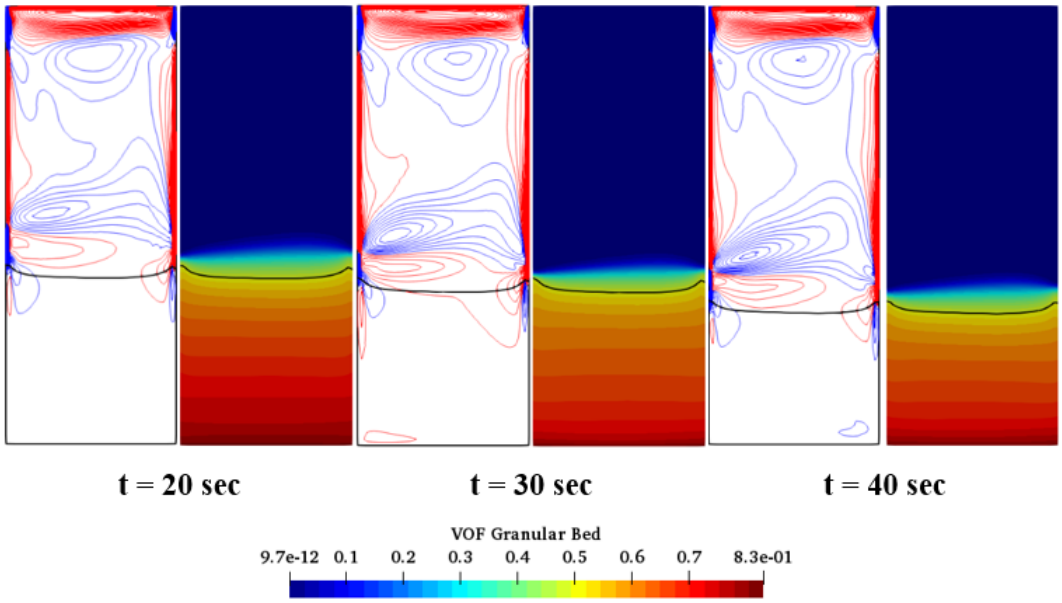

Figure 7.24: *Spatial overview of 135° position, showing H* and granular phase VOF respectively correction factor = 0.5 over t = 20 – 40 sec.*

Counter-rotating vortices are seen to be positioned closer to the granular bed interface relative to that of Case-4. Consequentially, the granular bed profile shows more distinctive features over t = 20 sec and t = 30 sec (Figure 7.24), seen by the ridge-like structure formed at the inner-wall over this period. The ridge-like structure is gradually smoothed out over the remainder of the time steps. Granular bed height over t = 20 – 40 sec (Figure 7.24) compared to that of the granular bed height of t = 80 sec (Figure 7.25), shows a reduction in the rate of granular bed erosion. The onset of the quasi-stable phase from t = 80 – 160 sec is captured, with stabilisation of fluid-granular interactions during the quasi-stable phase corresponding to a stabilisation in flow field behaviour.

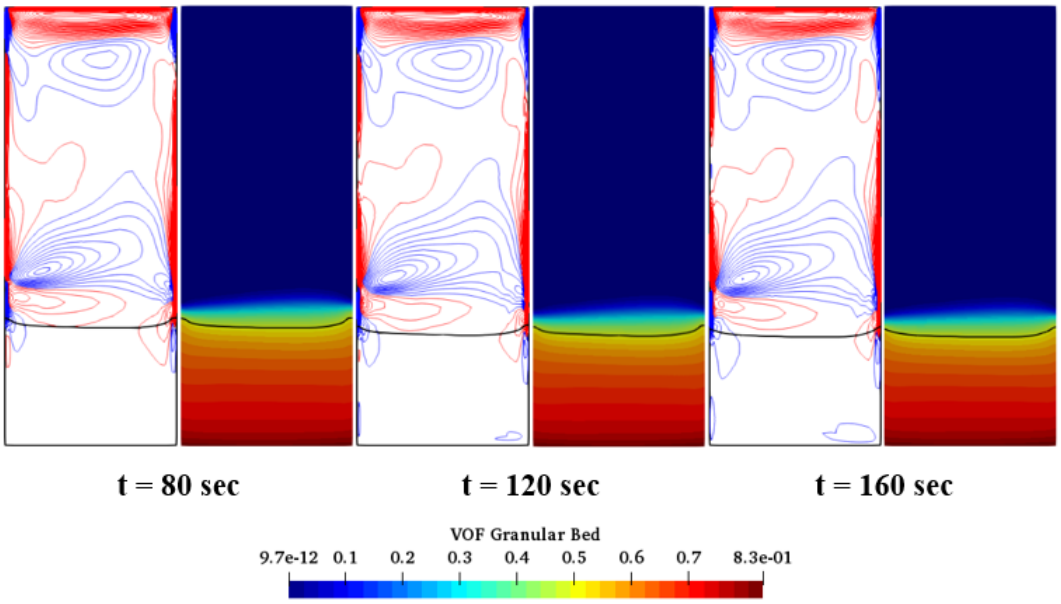

Figure 7.25: *Spatial overview of 135° position, showing H* and granular phase VOF respectively correction factor = 0.5 over t = 80 – 160 sec.*

Temporal analysis of the modified drag for Q= 55 L/min in Figure 7.26, shows qualitative similarity to experimental results under similar flow parameters (300 – 400 μm, flow rate 55 L/min). Initial observations show an increase in granular bed height within 20 sec, with fluctuations in granular bed height continuing to t = 60 sec. The initiation of quasi-stable fluid-granular interactions is captured at t = 110 sec. Temporal analysis of numerical results still shows a difference in temporal scales between numerical and experimental results.

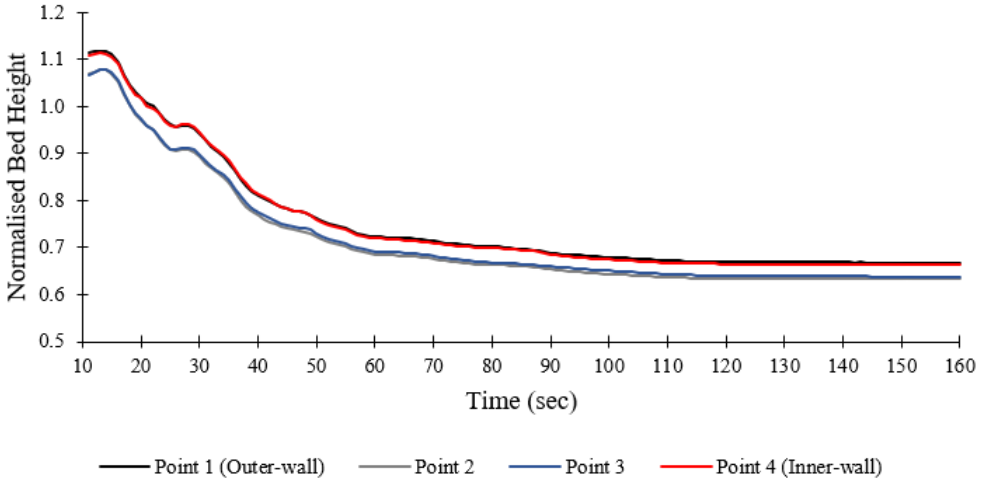

Figure 7.26: *Temporal overview of 135° position, showing the normalised granular bed height with respect to time.*

7.3.3 Effect of Modified Drag Coefficient

A comparison of numerical results using the standard and modified Gibilaro Drag model are presented for a granular bed of 300 – 400 μm at a flow rate 50 and 55 L/min. The temporal range of the modified Gibilaro Drag model cases is shortened to provide temporal alignment with non-modified counterpart cases. A comparison for each point from the outer-wall (Point 1) to the inner-wall (Point 4) of the duct cross-section is provided. The standard Gibilaro Drag model is indicated by the solid black line, with the modified Gibilaro Drag model, using a drag coefficient of 0.5, is indicated by a solid red line. Additionally, a brief discussion on the effect of increased drag coefficient on the outcomes of the modified Gibilaro Drag model is provided.

At a flow rate of 50 L/min, it can be seen in Figure 7.27 for all points, that the rate of erosion of the granular bed is higher for the numerical result across all points using Gibilaro Drag model. Fluctuation in granular bed height is captured by both models, noting that the occurrence of these fluctuations differ, with the modified Gibilaro Drag model showing fluctuations initiating earlier. When comparison between granular bed height at each investigation point is made, the most significant difference between the two models is found at Point 1 (outer-wall) and Point 4 (inner-wall).

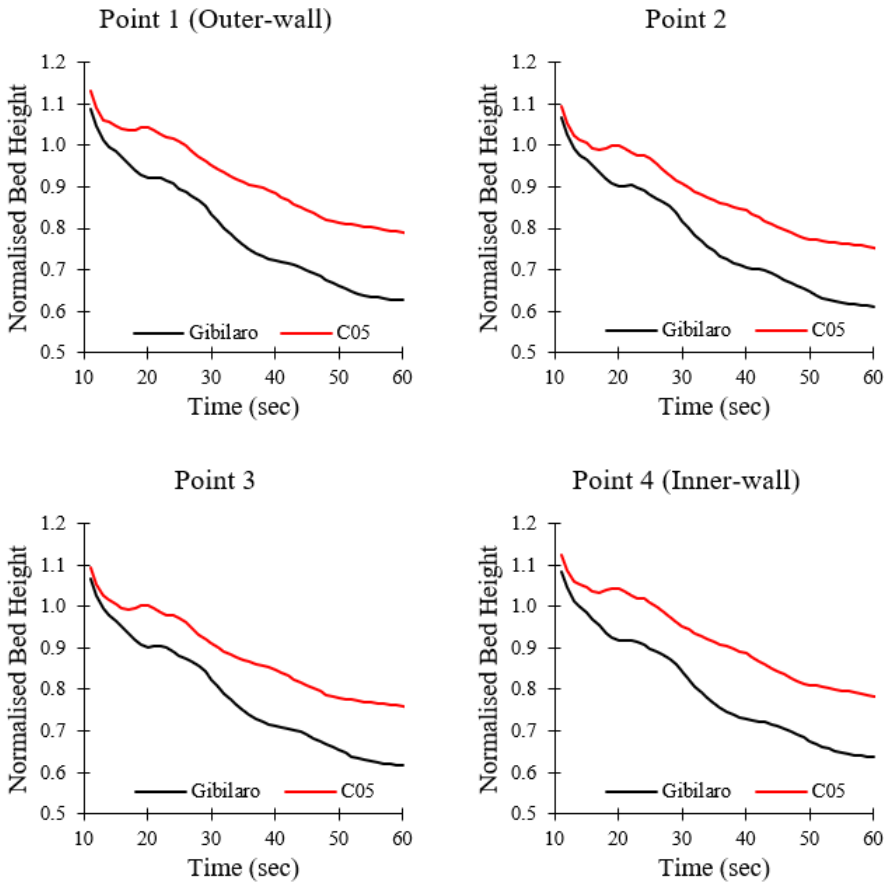

Figure 7.27: *Temporal comparison between the standard and modified Gibilaro drag model for granular bed 300 – 400 μm at 50 L/min.*

At an increased flow rate of 55 L/min, comparison between the standard and modified Gibilaro Drag model is shown in Figure 7.28. As with the comparison made in for 50 L/min (Figure 7.27), at a flow rate of 55 L/min, the standard Gibilaro Drag model shows more significant erosion. Additionally, fluctuation in granular bed height is captured by both models; the occurrence of these granular bed height fluctuation is seen to be in closer temporal alignment. The difference in granular bed height between drag coefficient model is seen to be consistent across each investigation point.

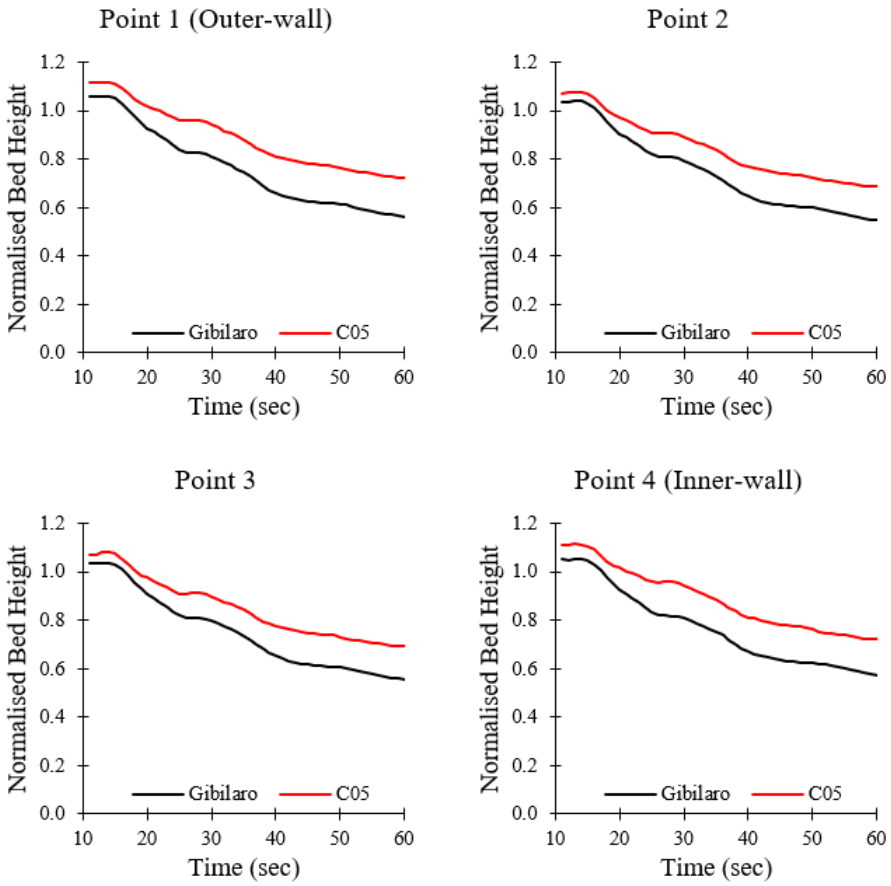

Figure 7.28: *Temporal comparison between the standard and modified Gibilaro drag model for granular bed 300 – 400 µm at 50 L/min.*

The modified Gibilaro drag model used a drag coefficient of 0.5; results were obtained for a drag coefficient of 0.6, 0.7, 0.8 and 0.9. Results obtained were found to be temporally and spatially identical to those obtained using a drag coefficient of 0.5 and therefore were excluded.

7.4 Quantitative Comparison of Results

A comparison between experimental and numerical results is provided, temporal and spatial results are compared to assess agreement between experimental observation and numerical predictions

7.4.1 Temporal Scale Comparison

Temporal comparison is made using the onset of the quasi-stable stage, and the duration of the transient stage, shown in Figure 7.29. Duration of the transient stage is determined by taking the difference between the quasi-stable stage and the initial stage. The black dashed line denotes perfect agreement between numerical and experimental results. Regarding the temporal comparison between results, it can be seen that the numerical predictions do not provide temporal agreement with experimental observation. Increased agreement is seen with respect to the duration of the transient stage, but numerical results underpredict the temporal scale. Regarding the initiation of the quasi-stable stage, the numerical prediction do not align with experimental results and show less agreement. This observation could be associated with initial stage and parameters which need to be measured more accurately. For instance, a fully homogeneous structure of granular material and a bed interface with no spatial imperfection (assumed in numerical model) are not physically accurate assumptions, and may be considered as a source of error.

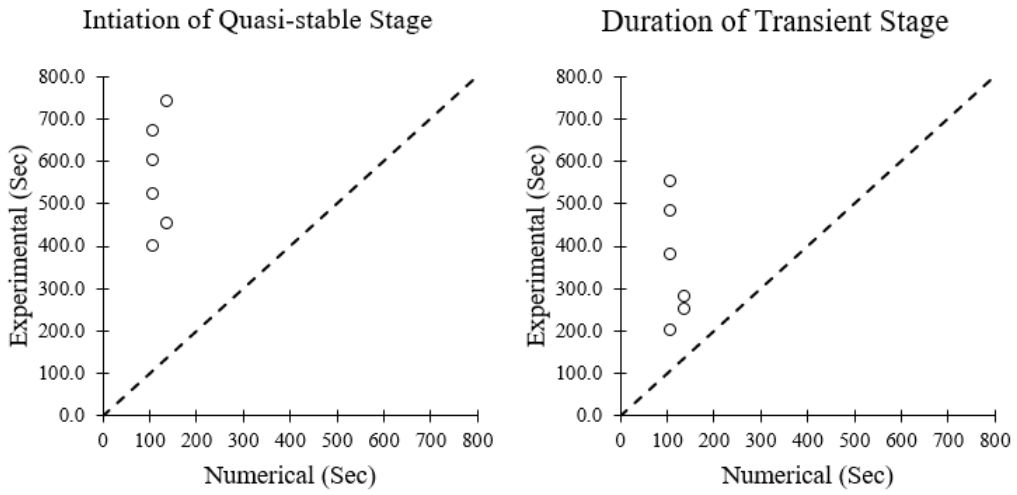

Figure 7.29: *Temporal scale comparison between experimental and numerical results, with perfect correlation denoted by the black dashed line.*

7.4.2 Spatial Comparison

Spatial comparison is made using the final normalised granular bed height for both experimental and numerical results, across investigations points during experimentation. Numerical results used in Figure 7.30 and 7.31 are taken from the modified Gibilaro Drag model cases, Case-6 denoted using black markers and Case-7 denoted using red markers. Results are presented, moving incrementally towards the inner-wall of the curved duct cross-section.

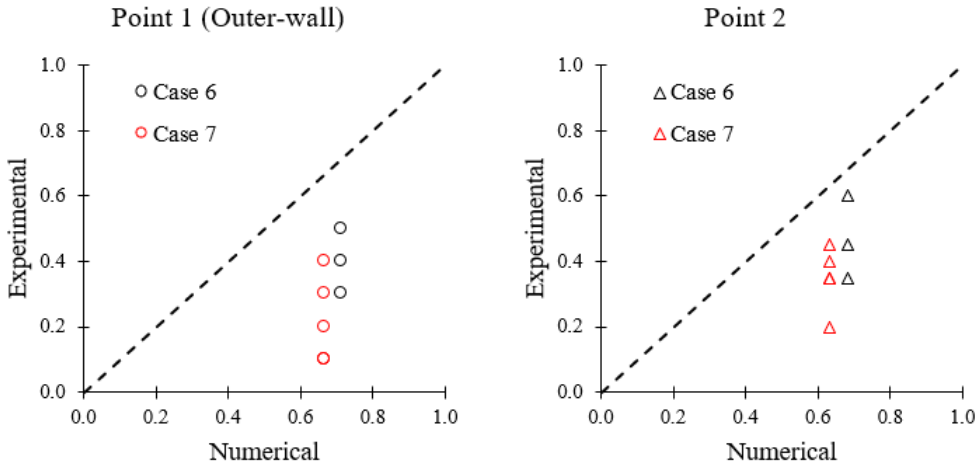

Figure 7.30: *Spatial comparison between experimental and numerical results for Point 1 and 2; perfect correlation is denoted by the black dashed line*

Concerning Point 1 (outer-wall), lack of agreement between experimental and numerical results are seen, improved agreement is captured for cases at a flow rate of 50 L/min (Case-6). Point 2, shows improved agreement between experimental and numerical results, with results captured for flow rate 50 L/min (Case-6) showing better agreement when compared to flow rate 55 L/min (Case-7).

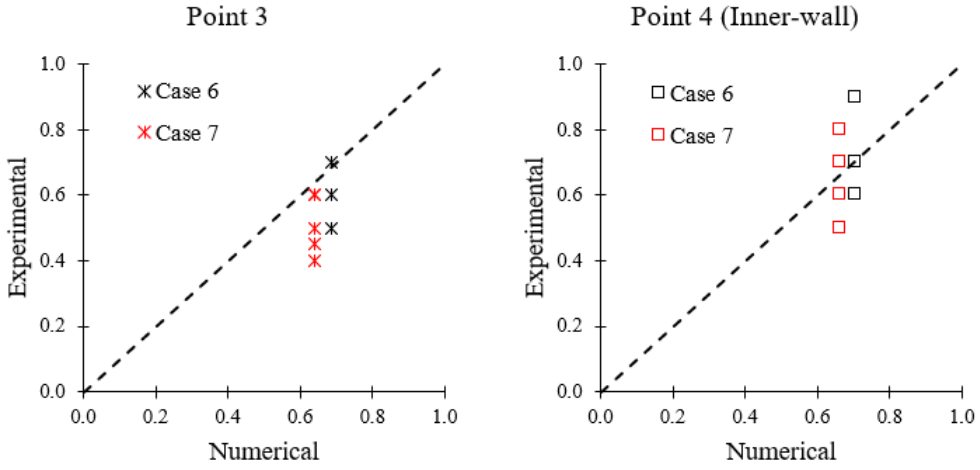

Figure 7.31: *Spatial comparison between experimental and numerical results for Point 3 and 4; perfect correlation is denoted by the black dashed line*

At point 3 along the cross-section, good agreement between the numerical predictions and experimental observations is captured for both flow rate 50 L/min (Case-6) and 55 L/min (Case-7), with the former showing the best agreement. At the inner-wall (Point 4), the best agreement between numerical predictions and experimental observations is captured, with both the 50 L/min and 55 L/min flow rates showing agreement with experimental results.

7.5 Summary of Numerical Outcomes

General observations of numerical results show granular bed features such as inner-wall dunes, described in section 4.1 of experimental results, is captured by numerical results (Figure 7.2 and 7.3). Granular bed topography shows qualitative similarity to the initial stages of experimental observations, with granular bed features being less pronounced than those captured in experimental results.

Results for numerical cases using the standard Gibilaro coefficient model, Cases-1 to Case-5, show greater granular phase diffusion, with Case-1 (150 – 300 μm bed at 55 L/min) exhibiting the greatest diffusion. Consequences of increased granular phase diffusion result in the displacement of counter-rotating vortex structures away from the granular bed interface. The displacement of vortex structure away from the granular bed interface give rise to axial flow dominated erosion, seen as a uniform granular bed profile. The diffuse nature of the granular phase and the subsequent effect on flow structures may be a determining factor in the reduction

of momentum transfer between the fluid and granular phases. Moreover, for cases with increased granular phase diffusion, reduced dynamic bed behaviour coupled with an increase in erosion rate, is captured. Modification of the Gibilaro drag model, by selecting a drag coefficient of 0.5, significantly reduced granular phase diffusion. The effect is seen with counter-rotating vortex formations being located at the granular bed interface, producing uneven granular bed profiles due to the proximity of these vortices (Figure 7.22 and Figure 7.24).

When assessing the temporal similarity of numerical and experimental results, reference is made to the modified Gibilaro Drag model cases for flow rates 50 L/min and 55 L/min (Figures 7.23 and 7.26). Distinct stages of interaction captured in experimental results, namely the initial, transient and quasi-stable stage are not in temporal alignment with numerical results. Reduced transient stage behaviour is captured for both flow rates, but lack the dynamic interactions captured during experimentation. The distinctive quasi-stable stage of fluid-granular interactions is captured, but the onset of this stage occurs earlier than that of experimental results under similar flow conditions. During the onset of the quasi-stable stage of interactions, the coupled nature between helical flow structures and granular bed profile is seen during the gradual stabilisation process occurring with the formation of a stable bedform.

Spatial comparison assessing the final quasi-stable granular bed height show agreement between experimental and numerical results to increase towards the inner-wall for the investigation cross-section located at 135°, shown in Figures 7.30 and 7.31. The difference between experimental and numerical results captured for Points closest to the outer-wall Point 1 and Point 2 coincides with the position of counter-rotating vortices closest to the granular bed interface. Additionally, granular bed profiles produced from numerical results are seen to be more uniform when compared to those captured for experimental results, suggesting that increased mesh resolution in the range of granular phase grain size is required to capture the complex fluid-granular interactions.

Chapter 8

Conclusions

The study presented in this thesis undertook an extensive review of published literature encompassing the nature of granular material, the threshold of grain movement, the role of turbulence on fluid-granular interaction, and secondary flow behaviour in curved ducts. A broad knowledge base was reported on fluid-granular interaction mechanisms, threshold of grain movement and secondary flow behaviour in curved ducts comprising numerous analytical, experimental and numerical modelling studies, and a wide range of applicable methodologies. However, studies reporting on the erosion-sedimentation process in curved ducts were virtually unexplored.

The study undertaken has addressed this shortfall using a closed ducted configuration with fluid passage geometry selected to enhance secondary flow instability. Characterisation of erosion and sedimentation in curved fluid passages was achieved by a combination of experimental and numerical investigations. Captured interactions provided a qualitative and quantitative overview with spatial and temporal comparison made for varied granular phase particle size ranges over a multiple flow rates.

8.1 Qualitative description of interactions and granular bed structures

A qualitative description of fluid-granular interactions was provided, with an overview and identification of discrete stages of interactions, namely the initial stage, transient stage and quasi-stable stage. The commencement of fluid-granular interactions (Initial stage – Stage.1), was characterised by the initiation and evolution of bedforms, such as inner-wall dunes and inner-wall ridges. Continue growth and propagation of inner-wall dunes was accompanied by the transition to the transient stage (Stage.2). The transient stage was seen to be a direct result of the outward widening of scour around the parameter of inner-wall dunes and eventual contact with the outer-wall, defined by prominent Fluid-granular interactions. The prominence of these interactions dynamic and

complex granular bed profiles, formed the scour paths of helix-like structures. The dynamic and oscillatory reshaping of the granular bed characteristic of the transient stage subsided, giving way to the final stage of interactions, the quasi-stable stage (Stage.3). The defining characteristic of this stage was the stable granular bed profile captured. Moreover, the granular bed profile during the quasi-stable stage was seen to be dominated by outer-wall erosion. Outer-wall dominated erosion can be attributed to the local intensity of secondary vortices, known to be higher at the outer-wall. Quasi-stable fluid-granular interactions identified are attributed to the coupled nature of granular bed profile and secondary flow structures.

Qualitative observations regarding the sensitivity of Fluid-granular interactions to surface perturbations were shown to result in the unpredictable initiation of erosion/sedimentation along the curved fluid passage. Sources of perturbations such as small surface defects at the curved fluid passage inlet, propagated the premature formation of inner-wall dunes, initiating the three stages of interaction mentioned above at locations that remained relatively unchanged for the majority of experiments undertaken, underscoring the stochastic nature of fluid-granular interaction along the curved fluid passage

A valuable contribution provided by qualitative observations was the identification of the radial position of 135°, which provided reliable and repeatable fluid-granular interactions used for temporal investigation across all flow rates investigated.

8.2 Spatial Interactions

Observations made during the qualitative assessment of Fluid-granular interaction correspond to those seen during spatial investigation. Quantitative spatial investigation captured the dominance of fluid-granular interactions along the outlet half (90°-180°) of the curved passage. The inlet half showed no measurable interaction occurring within the first 15° and the consistent formation of an inner-wall ridge located along the 60° radial position.

Radial positions 135° and 165° showed uneven fluid-granular interactions with sudden and dynamic changes to granular bed profiles. Captured granular bed profile related to the growth of inner-wall ridge structures suggests the influence of secondary flow structures, hinting at a mutually coupled relationship between the two. Moreover, the effects of this mutually coupled relationship are seen to increase towards the outlet (180°) of the curved fluid passage.

8.3 Temporal Behaviour

Temporal analysis carried out at the fixed cross-section of 135° for combinations of various flow rates and mean particle diameter, identified critical parameters, namely, flow rate and particle mean diameter as pivotal to fluid-granular interactions.

Temporal analysis undertaken for a granular bed of size ranges, 150 – 300 μm and 300 – 400 μm over flow rates 47 L/min to 63 L/min, identified the three previously described stages of interaction, the initial stage (Stage.1), transient stage (Stage.2) and the Quasi-stable stage (Stage.3). Transient stage interactions show an increase in dynamic granular bed behaviour with increased flow. Temporal analysis captured during the transient stage show strong evidence of the effects of secondary flow instability and the subsequent effect on granular bed reshaping, the most significant occurring at the outer-wall. The oscillatory and transient nature of these profiles suggest an intricate mutually coupled relationship between secondary flow structure present in the curved passage and the granular bed.

Reduced transient stage, due to increased flow rate, corresponded to earlier establishment quasi-stable fluid-granular interactions. Quasi-stable temporal behaviour of this stage was seen by the general asymptotic nature of the temporal profiles across the investigation area. Stabilisation of fluid-granular interactions was demonstrated temporal profiles captured and are a result of the presence of localised helical flow structures, coupled with the granular bed morphology acting to stabilise the granular bed.

8.4 Effects of particle size

Parametric assessment of the effects of granular bed particle size on fluid-granular interactions show both an enhancing and suppressing effects during the three stages of interaction identified. At lower flow rates transient stage onset is delayed in comparison to higher flow rates, seen as an extended initial stage for size ranges 150 – 300 μm and 300 – 400 μm. Increased flow rate is shown to correspond to a reduced transient stage onset time, and was seen to decay with flow rates 53 L/min to 61 L/min. Granular beds comprised of larger particles (475 – 1180 μm), showed no difference in transient stage onset over the flow rates investigated (57 – 65 L/min). quasi-stable interactions for granular bed size range 150 – 300 μm and 300 – 400 μm show initial delayed onset of the quasi-stable stage at lower flow rates, with increased flow rates corresponding to a reduced quasi-stable stage onset time. Granular beds consisting of 475-1180 μm grains, show relatively stable quasi-stable onset times.

Parametric assessment of transient stage duration for granular beds of 150 – 300 μm and 300 – 400 μm showed that increased flow rate did not correspond to a shortening in the transient stage. Increased flow rate was associated with increased variability in transient stage duration. The variability in transient stage duration suggests that axial flow is not the primary mechanism for the dynamic reshaping of the granular bed during the transient stage. Secondary flow instability, coupled with the stochastic nature of granular materials is the prime agents responsible for the scattered nature transient stage duration. In contrast, a marked difference in temporal behaviour was seen for courser granular beds (475 – 1180 μm), denoted by the sudden transition to quasi-stable interactions and the unique temporal profile produced, occurring at flow rates from 58 -65 L/min. The presence of larger grains is associated with increased drag force, suggesting that fluid-granular interactions for beds of size range 475 – 1180 μm are influenced by axial flow to a greater extent relative to secondary flow.

8.5 Numerical Evaluation

Sensitivity analysis carried out to determine an appropriate drag model to be used with the Euler-Euler Granular phase model utilised, consisted of a comparison of three commonly employed models namely, Gibilaro, Huilin-Gidaspow and Syamlal-Obrien models. Assessment of drag model selection on the granular bed profile located at the fixed cross-section of 135°, showed both the Huilin-Gidaspow and Syamlal-Obrien models to overpredict granular bed erosion. The granular bed profile produced using the Gibilaro drag model showed relatively lower rates granular bed erosion, therefore further numerical characterisation of fluid-granular interactions was undertaken using the Gibilaro drag model.

Spatial representation of fluid-granular interactions using the standard Gibilaro drag model, produced a diffused granular phase, with the most significant diffusion occurring for a granular bed of 150 – 300 μm, reducing with each increase in granular bed coarseness. Consequences of increased granular phase diffusion were seen by the displacement of counter-rotating vortex structures away from the granular bed interface. The diffuse nature of the granular phase and the subsequent effect on flow field structures may be a determining factor in the reduction of momentum transfer between the fluid and granular phases. Addressing this, a correction factor was applied to the Gibilaro drag model using a drag coefficient of 0.5, resulting in significantly reduced granular phase diffusion. Reduced granular phase diffusion, corresponded increased proximity of counter-rotating helical structures to the granular bed interface, producing uneven granular bed profiles.

Further adjustments to the Gibilaro drag model using increased drag coefficients of 0.6, 0.7, 0.8 and 0.9 show a lack of model sensitivity to drag coefficient modification. The lack of model sensitivity to drag coefficient modification can be attributed to the physical flow conditions and numerical grid resolution causes. Interactions at the fluid-granular interface and the subsequent boundary layer produced result in reduced flow velocities within this boundary layer. Increases drag coefficient to the Gibilaro drag model yield negligible increases in drag force applied to the granular phase due to the reduced flow velocities present within the boundary layer. Additionally, lack of model sensitivity to drag coefficient modification may be a result of mesh resolution. Higher mesh resolution would produce a less diffuse fluid-granular interface, potentially

allowing for greater refinement in the momentum transfer between phases and as such, increased model sensitivity.

The presence of granular bed features identified in qualitative experimental observations, namely migrating inner-wall dunes and the formation of an inner-wall ridge, are captured with reduced bed height profiles relative to experimental results.

Spatial and temporal numerical results captured the quasi-stable stage of fluid-granular interactions observed in experimental results. Granular bed profiles produced during the quasi-stable stage, at the investigation cross-section located of 135°, show increasing quantitative agreement in the direction of the inner-wall. Qualitative comparison of temporal behaviour between experimental and numerical results show similarities in overall transition towards a stable granular bedform. Additionally, reduced transient stage behaviour is captured, but lacks the dynamic oscillatory behaviour observed in during experimental investigation. Regarding quantitative comparison of temporal results, the establishment of quasi-stable interactions does not show temporal alignment with experimental results. Additionally, granular bed profiles produced from numerical results are seen to be more uniform in comparison to experimental results. The discrepancy between numerical and experimental observation is attributed to the drag selection models commonly used for Eulerian multiphase modelling (Gibilaro, Huilin-Gidaspow and Syamlal-Obrien) which are intrinsically linked to momentum transfer in Eulerian treatments. These drag models are a product of validation against pressure drop experiments using fluidised or randomly packed beds. The need for drag models capable of capturing spatial and temporally accurate interactions between the fluid and granular phases in curved passages is needed.

Numerical investigation provided insight into the mutually coupled relationship between helical flow field structures and the granular bed. The presence of counterrotating vortices is identified at the outer-wall along the fluid-granular interface. These counterrotating vortices are shown track the displacement of the granular bed interface. Moreover, the influence of secondary flow effects on the establishment of quasi-stable fluid-granular interactions is captured with the stabilisation of the flow field corresponding to an equivalent stabilisation of granular interface profile.

8.6 Key Contributions

An original contribution towards the characterisation of erosion and sedimentation in curved fluid passages has been made. Verified measurements original to the field provide a valuable resource for further physical investigation and can be considered as a reliable benchmark for the validation of numerical models and specifically CFD closures.

Key findings are be summarised as follows:

- Initiation stage is indicated as the regime over which, the macroscopic variation of the bed is insignificant while smaller eddies cause micro changes;
- Following the initiation process, transition stage is indicated by the regimes of formation and movement of dunes resulting in periodic bed profiles at a given flow rate;
- The bed essentially reaches a quasi-stable regime where secondary flow vortices are the dominant erosive flow structure, and the bed interface maintains an outward leaning slope;
- The temporal behaviour of all the associated stages accelerate with an increase of flow rate;
- The particle size is seen to influence in both enhancing and suppressing the initiation process. Larger particle size imparts a higher drag force decelerating the initiation, while advanced turbulent boundary layer and higher porosity tend to accelerate initiation;
- The transition process is shortened for beds with larger particle sizes since they are less sensitive to smaller eddies and perturbations; and
- Current drag models derived from fluidised/packed bed experiments do not capture spatially and temporally accurate interactions between the fluid and granular phases in curved passages.

8.7 Possible future research directions

The field of multi-phase fluid flow coupled with that of secondary flow instability provides extensive opportunities for further investigation. Contributions to fields such as mass and heat transfer, mineral processing, reactor design and the modelling of natural systems such as rivers show the importance and applicability continued investigation.

8.7.1 Future experimental work

A potential extension of the current work would consist of an experimental investigation of both the flow field and granular bed profile. Techniques such as such as PIV (Particle Image Velocimetry) and LIF (Laser Induced Fluorescence) are proven methods for flow field investigation, but care would need to be employed under periods of rapid erosion, due to the presence of entrained grains removed from the granular bed and their impact on measurement accuracy. A promising, solution is the use of ultrasonic measurement techniques, recent advances have allowed for both the flow field and granular bed profile to be captured within relatively small passageways, providing high-resolution 3-dimensional investigation[65]. Spatially and temporally aligned flow field and granular bed interface data would provide a valuable benchmark for future numerical model validations studies.

8.7.2 Future numerical modelling

The current Euler-Euler Granular Phase model used has seen contemporary use in multiphase problems. The treatment of the granular phase as a pseudo-fluid presents challenges when accounting for the discrete nature of entrained grains removed from the granular phase. Lagrangian methods, though capable of capturing these discrete entrained grains suffer from being computationally demanding when modelling system at a 1:1 scale. A recent solution is that of a hybrid Euler-Lagrangian approach[66], this method shows promise when applied to the current experimental/numerical configuration, and allows for both treatment of the granular phase as a pseudo-fluid, capturing and accounting for the discrete nature entrained grains, with the promise of reduced computational resources.

Appendix A

Experiment Measurement Accuracy

Table A.1: *Experimental accuracy for granular bed 150 – 300 μm.*

Experiment	**L1** (±%)	**L2** (±%)	**L3** (±%)	**L4** (±%)
EXP-135-150-47-02	2	2	2	2
EXP-135-150-50-01	3	2	3	3
EXP-135-150-53-01	3	2	3	3
EXP-135-150-57-04	1	1	1	2

Table A.2: *Experimental accuracy for granular bed 300 – 400 μm.*

Experiment	**L1** (±%)	**L2** (±%)	**L3** (±%)	**L4** (±%)
EXP-135-300-47-03	4	3	3	4
EXP-135-300-50-02	1	1	1	2
EXP-135-300-50-10	2	2	3	3
EXP-135-300-53-02	3	2	3	3
EXP-135-300-53-04	3	2	3	3
EXP-135-300-53-05	3	2	4	3
EXP-135-300-57-01	3	2	3	3
EXP-135-300-57-02	3	3	4	3
EXP-135-300-57-04	2	2	4	3
EXP-135-300-57-07	3	3	4	3
EXP-135-300-60-02	3	3	3	4
EXP-135-300-60-03	3	3	3	3
EXP-135-300-60-04	3	2	3	3
EXP-135-300-60-05	3	2	4	3
EXP-135-300-63-01	3	2	3	2

Table A.3: *Experimental accuracy for granular bed 475 – 1180 μm.*

Experiment	**L1** (±%)	**L2** (±%)	**L3** (±%)	**L4** (±%)
EXP-135-475-57-01	2	3	3	3
EXP-135-475-57-02	3	2	3	2
EXP-135-475-60-01	3	2	3	3
EXP-135-475-63-02	2	2	3	3

Table A.4: *Calibration uncertainty at 135 Deg radial position*

Calibration Set	**L1** (±%)	**L2** (±%)	**L3** (±%)	**L4** (±%)
Cam 1	0.5	0.3	0.3	0.4
Cam 2	0.4	0.3	0.3	0.2
Cam 3	0.4	0.3	0.6	0.3
Cam 4	0.8	0.8	0.8	0.8

Table A.5: *Full bed scan calibration uncertainty*

Calibration Set	**L1** (±%)	**L2** (±%)	**L3** (±%)	**L4** (±%)
Cam 1	1.0	0.8	0.7	0.8
Cam 2	0.8	0.9	0.8	0.9
Cam 3	0.7	0.4	0.6	0.5
Cam 4	0.5	0.4	0.4	0.4

Bibliography

[1] Claudio Faria Duarte, Nima Nadim, and Tilak T Chandratilleke. "Experimental study of granular bed erosion and sedimentation subjugated to the secondary flow structures in curved ducts". In: *Advances in Mechanical Engineering* 11.11 (2019), p. 1687814019885255.

[2] GDR MiDi. "On dense granular flows". In: *The European Physical Journal E* 14.4 (2004), pp. 341–365.

[3] Heinrich M Jaeger, Sidney R Nagel, and Robert P Behringer. "Granular solids, liquids, and gases". In: *Reviews of modern physics* 68.4 (1996), p. 1259.

[4] Heinrich M Jaeger, Sidney R Nagel, and Robert P Behringer. "The physics of granular materials". In: *Physics today* 49 (1996), pp. 32–39.

[5] Charles S Campbell. "Rapid granular flows". In: *Annual Review of Fluid Mechanics* 22.1 (1990), pp. 57–90.

[6] Yoël Forterre and Olivier Pouliquen. "Flows of dense granular media". In: *Annu. Rev. Fluid Mech.* 40 (2008), pp. 1–24.

[7] Philippe Frey and Michael Church. "Bedload: a granular phenomenon". In: *Earth Surface Processes and Landforms* 36.1 (2011), pp. 58–69.

[8] Stuart B Savage and K Hutter. "The motion of a finite mass of granular material down a rough incline". In: *Journal of fluid mechanics* 199 (1989), pp. 177–215.

[9] Tamás Börzsönyi, Robert E Ecke, and Jim N McElwaine. "Patterns in flowing sand: understanding the physics of granular flow". In: *Physical review letters* 103.17 (2009), p. 178302.

[10] James T Jenkins and Stuart B Savage. "A theory for the rapid flow of identical, smooth, nearly elastic, spherical particles". In: *Journal of fluid mechanics* 130 (1983), pp. 187–202.

[11] Isaac Goldhirsch. "Rapid granular flows". In: *Annual review of fluid mechanics* 35.1 (2003), pp. 267–293.

[12] Ralph Alger Bagnold. "Experiments on a gravity-free dispersion of large solid spheres in a Newtonian fluid under shear". In: *Proc. R. Soc. Lond. A* 225.1160 (1954), pp. 49–63.

[13] Ralph Alger Bagnold. "The flow of cohesionless grains in fluids". In: *Phil. Trans. R. Soc. Lond. A* 249.964 (1956), pp. 235–297.

[14] Grove Karl Gilbert and Edward Charles Murphy. *The transportation of debris by running water*. 86. US Government Printing Office, 1914.

[15] John M Buffington and David R Montgomery. "A systematic analysis of eight decades of incipient motion studies, with special reference to gravel-bedded rivers". In: *Water Resources Research* 33.8 (1997), pp. 1993–2029.

[16] MC Miller, IN McCave, and P_D Komar. "Threshold of sediment motion under unidirectional currents". In: *Sedimentology* 24.4 (1977), pp. 507–527.

[17] SJ White. "Plane bed thresholds of fine grained sediments". In: *Nature* 228.5267 (1970), pp. 152–153.

[18] JD Fenton and JE Abbott. "Initial movement of grains on a stream bed: The effect of relative protrusion". In: *Proc. R. Soc. Lond. A* 352.1671 (1977), pp. 523–537.

[19] François Charru, Hélene Mouilleron, and Olivier Eiff. "Erosion and deposition of particles on a bed sheared by a viscous flow". In: *Journal of Fluid Mechanics* 519 (2004), pp. 55–80.

[20] Morgane Houssais et al. "Onset of sediment transport is a continuous transition driven by fluid shear and granular creep". In: *Nature communications* 6 (2015), p. 6527.

[21] AJ Raudkivi. "Study of sediment ripple formation". In: *Journal of the Hydraulics Division* 89.6 (1963), pp. 15–34.

[22] AJ Raudkivi. "Bed forms in alluvial channels". In: *Journal of Fluid Mechanics* 26.3 (1966), pp. 507–514.

[23] Jonathan M Nelson et al. "Role of near-bed turbulence structure in bed load transport and bed form mechanics". In: *Water resources research* 31.8 (1995), pp. 2071–2086.

[24] SR McLean, JM Nelson, and SR Wolfe. "Turbulence structure over two-dimensional bed forms: Implications for sediment transport". In: *Journal of Geophysical Research: Oceans* 99.C6 (1994), pp. 12729–12747.

[25] Stephen J Kline et al. "The structure of turbulent boundary layers". In: *Journal of Fluid Mechanics* 30.4 (1967), pp. 741–773.

[26] Edward Robert Corino and Robert S Brodkey. "A visual investigation of the wall region in turbulent flow". In: *Journal of Fluid Mechanics* 37.1 (1969), pp. 1–30.

[27] Anthony J Grass. "Structural features of turbulent flow over smooth and rough boundaries". In: *Journal of Fluid Mechanics* 50.2 (1971), pp. 233–255.

[28] Mr Rashidi, G Hetsroni, and Sanjoy Banerjee. "Particle-turbulence interaction in a boundary layer". In: *International Journal of Multiphase Flow* 16.6 (1990), pp. 935–949.

[29] JIM Best. "On the entrainment of sediment and initiation of bed defects: insights from recent developments within turbulent boundary layer research". In: *Sedimentology* 39.5 (1992), pp. 797–811.

[30] Jim Best. "The fluid dynamics of river dunes: A review and some future research directions". In: *Journal of Geophysical Research: Earth Surface* 110.F4 (2005).

[31] Alex J Sutherland. "Proposed mechanism for sediment entrainment by turbulent flows". In: *Journal of Geophysical Research* 72.24 (1967), pp. 6183–6194.

[32] Philip B Williams and Patrick H Kemp. "Initiation of ripples on flat sediment beds". In: *Journal of the Hydraulics Division* 97.4 (1971), pp. 502–522.

[33] Panayiotis Diplas et al. "The role of impulse on the initiation of particle movement under turbulent flow conditions". In: *Science* 322.5902 (2008), pp. 717–720.

[34] Ahmet O Celik et al. "Impulse and particle dislodgement under turbulent flow conditions". In: *Physics of Fluids* 22.4 (2010), p. 046601.

[35] John Eustice. "Flow of water in curved pipes". In: *Proceedings of the Royal Society of London. Series A, Containing Papers of a Mathematical and Physical Character* 84.568 (1910), pp. 107–118.

[36] John Eustice. "Experiments on stream-line motion in curved pipes". In: *Proceedings of the Royal Society of London. Series A, Containing Papers of a Mathematical and Physical Character* 85.576 (1911), pp. 119–131.

[37] Wo R Dean. "XVI. Note on the motion of fluid in a curved pipe". In: *The London, Edinburgh, and Dublin Philosophical Magazine and Journal of Science* 4.20 (1927), pp. 208–223.

[38] CM White. "Streamline flow through curved pipes". In: *Proceedings of the Royal Society of London. Series A, Containing Papers of a Mathematical and Physical Character* 123.792 (1929), pp. 645–663.

[39] JA Baylis. "Experiments on laminar flow in curved channels of square section". In: *Journal of Fluid Mechanics* 48.3 (1971), pp. 417–422.

[40] JAC Humphrey, AMK Taylor, and JH Whitelaw. "Laminar flow in a square duct of strong curvature". In: *Journal of Fluid Mechanics* 83.3 (1977), pp. 509–527.

[41] JAC Humphrey, JH Whitelaw, and G Yee. "Turbulent flow in a square duct with strong curvature". In: *Journal of Fluid Mechanics* 103 (1981), pp. 443–463.

[42] P Hille, R Vehrenkamp, and EO Schulz-Dubois. "The development and structure of primary and secondary flow in a curved square duct". In: *Journal of Fluid Mechanics* 151 (1985), pp. 219–241.

[43] H Iacovides et al. "Turbulent boundary-layer development around a square-sectioned U-bend: measurements and computation". In: (1990).

[44] KC Cheng and Mltsunobu Akiyama. "Laminar forced convection heat transfer in curved rectangular channels". In: *International Journal of Heat and Mass Transfer* 13.3 (1970), pp. 471–490.

[45] KC Cheng, Ran-Chau Lin, and Jenn-Wuu Ou. "Fully developed laminar flow in curved rectangular channels". In: *journal of Fluids Engineering* 98.1 (1976), pp. 41–48.

[46] Shiro SUGIYAMA, Taro HAYASHI, and Koji YAMAZAKI. "Flow Characteristics in the Curved Rectangular Channels: Visualization of Secondary Flow". In: *Bulletin of JSME* 26.216 (1983), pp. 964–969.

[47] Tilak T Chandratilleke et al. "Numerical prediction of secondary flow and convective heat transfer in externally heated curved rectangular ducts". In: *International Journal of Thermal Sciences* 42.2 (2003), pp. 187–198.

[48] Tilak T Chandratilleke, Nima Nadim, and Ramesh Narayanaswamy. "Vortex structure-based analysis of laminar flow behaviour and thermal characteristics in curved ducts". In: *International Journal of Thermal Sciences* 59 (2012), pp. 75–86.

[49] TT Chandratilleke and Nima Nadim. "An Investigation of Particulate Flow Behaviour and Sedimentation in Curved Channel using Euler-Euler Approach". In: *The Proceedings of the 19th Australasian Fluid Mechanics Conference*. 2014.

[50] RC Joshi et al. "Effect of aging on the penetration resistance of sands". In: *Canadian Geotechnical Journal* 32.5 (1995), pp. 767–782.

[51] Debashis Basu et al. "Comparison of Eulerian-Granular and discrete element models for simulation of proppant flows in fractured reservoirs". In: *ASME 2015 International Mechanical Engineering Congress and Exposition*. American Society of Mechanical Engineers Digital Collection. 2015.

[52] Lu Huilin, He Yurong, and Dimitri Gidaspow. "Hydrodynamic modelling of binary mixture in a gas bubbling fluidized bed using the kinetic theory

of granular flow". In: *Chemical Engineering Science* 58.7 (2003), pp. 1197–1205.

[53] ANSYS Fluent. "ANSYS fluent theory guide 15.0". In: *ANSYS, Canonsburg, PA* (2013).

[54] Shitanshu Gohel et al. "CFD modeling of solid suspension in a stirred tank: Effect of drag models and turbulent dispersion on cloud height". In: *International Journal of Chemical Engineering* 2012 (2012).

[55] Giuseppina Montante, Davide Pinelli, and Franco Magelli. "Scale-up criteria for the solids distribution in slurry reactors stirred with multiple impellers". In: *Chemical Engineering Science* 58.23-24 (2003), pp. 5363–5372.

[56] Dongfang Liang, Liang Cheng, and Fangjun Li. "Numerical modeling of flow and scour below a pipeline in currents: Part II. Scour simulation". In: *Coastal engineering* 52.1 (2005), pp. 43–62.

[57] LG Gibilaro et al. "Generalized friction factor and drag coefficient correlations for fluid-particle interactions". In: *Chemical engineering science* 40.10 (1985), pp. 1817–1823.

[58] FJ Moraga, FJ Bonetto, and RT Lahey. "Lateral forces on spheres in turbulent uniform shear flow". In: *International Journal of Multiphase Flow* 25.6-7 (1999), pp. 1321–1372.

[59] Dimitri Gidaspow. *Multiphase flow and fluidization: continuum and kinetic theory descriptions*. Academic press, 1994.

[60] Sebastian Zimmermann and Fariborz Taghipour. "CFD modeling of the hydrodynamics and reaction kinetics of FCC fluidized-bed reactors". In: *Industrial & engineering chemistry research* 44.26 (2005), pp. 9818–9827.

[61] Dimitri Gidaspow, Rukmini Bezburuah, and J Ding. *Hydrodynamics of circulating fluidized beds: kinetic theory approach*. Tech. rep. Illinois Inst. of Tech., Chicago, IL (United States). Dept. of Chemical . . ., 1991.

[62] CKK Lun et al. "Kinetic theories for granular flow: inelastic particles in Couette flow and slightly inelastic particles in a general flowfield". In: *Journal of fluid mechanics* 140 (1984), pp. 223–256.

[63] David G Schaeffer. "Instability in the evolution equations describing incompressible granular flow". In: *Journal of differential equations* 66.1 (1987), pp. 19–50.

[64] Madhava Syamlal and Thomas J O'Brien. "Computer simulation of bubbles in a fluidized bed". In: *AIChE Symp. Ser.* Vol. 85. 1. Publ by AIChE. 1989, pp. 22–31.

[65] Anthony Auzerais et al. “Formation of localized sand patterns downstream from a vertical cylinder under steady flows: Experimental and theoretical study”. In: *Physical Review E* 94.5 (2016), p. 052903.

[66] Wojciech P Adamczyk et al. “Modeling of particle transport and combustion phenomena in a large-scale circulating fluidized bed boiler using a hybrid Euler–Lagrange approach”. In: *Particuology* 16 (2014), pp. 29–40.